Fermi National Accelerator Laboratory

FERMILAB-Pub-90/258-E
[E687]

Description and Performance of the Fermilab E687 Spectrometer*

The E687 Collaboration
Fermi National Accelerator Laboratory
P. O. Box 500
Batavia, Illinois 60510

December 31, 1990

* To be submitted to Nucl. Instrum. Methods

Operated by Universities Research Association Inc. under contract with the United States Department of Energy

Description and Performance of the Fermilab E687 Spectrometer

P. L. Frabetti, V. Giordano, G. Molinari
Dip. di Fisica dell'Universita' and INFN - Bologna, I-40126 Bologna, Italy

C. W. Bogart[1], P. Coteus[2], J. P. Cumalat, S. Culy, H. W. K. Cheung, C. Dallapiccola, E. Erdos, J. Ginkel, W. Johns, G. Schultz
University of Colorado, Boulder, CO 80309, USA

J. N. Butler, S. Cihangir, A. Cotta-Ramusino, R. Currier, F. Davenport[3], I. Gaines, P. H. Garbincius, S. A. Gourlay, D. J. Harding, S. Hansen, R. Justice, K. Kephart, P. Kasper, A. Kreymer, P. Lebrun, S. Shukla
Fermilab, Batavia, IL 60510, USA

S. Bianco, F. L. Fabbri, M. Giardoni, L. Passamonti, V. Russo, A. Spallone, A. Zallo
Laboratori Nazionali di Frascati dell'INFN, I-00044 Frascati, Italy

R. Culbertson, M. Diesburg[4], G. Jaross[5], K. Lingel[6], P. D. Sheldon, J. Wiss
University of Illinois at Urbana-Champaign, Urbana,IL 61801

G. Alimonti, G. Bellini, W. R. Cavaletti, P. D'Angelo, M. Di Corato, M. G. Giammarchi, P. Inzani, F. Leveraro, S. Malvezzi, P. F. Manfredi[7], D. Menasce, E. Meroni, L. Moroni, D. Pedrini, L. Perasso, F. Ragusa, A. Sala, S. Sala, D. Torretta, M. Vittone
Dip. di Fisica dell'Universita' and INFN - Milano, I-20133 Milan, Italy

D. Buchholz, C. Castoldi, D. Claes, B. Gobbi, B. O'Reilly, S. Park[8], R. Yoshida[9], R. Tilden
Northwestern University, Evanston, IL 60208, USA

B. W. Baumbaugh, J. M. Bishop, J. K. Busenitz[10], N. M. Cason, J. D. Cunningham[11], R. W. Gardner, C. J. Kennedy, G. N. Kim, T. F. Lin, E. J. Mannel, R. J. Mountain, D. L. Puseljic, R. C. Ruchti, W. D. Shephard, J. A. Swiatek, Z. Y. Wu, M. E. Zanabria
University of Notre Dame, Notre Dame, IN 46556, USA

V. Arena, G. Boca, R. Diaferia, S. P. Ratti, P. Vitulo
Dip. di Fisica dell'Universita' and INFN - Pavia, I-27100 Pavia, Italy

A. Lopez, University of Puerto Rico at Mayaguez, Puerto Rico

H. Mendez[12], Cinvestav-IPN, A.P. 14-740,07000 Mexico DF, Mexico and Fermilab

V. Paolone, P. M. Yager, University of California-Davis, Davis, CA 95616

J. R. Wilson, University of South Carolina, Columbia, SC 29208

J. F. Filasetta, Northern Kentucky University, Highland Heights, KY 41076

1. Present address: Vector Research Company, 6903 Rockledge Drive, Bethesda,MD 20817, USA

2. Present address: IBM T.J. Watson Laboratories, Yorktown Heights,NY 10598 USA

3. Present address: University of North Carolina-Asheville, Asheville, NC 28804 USA

4. Present address: Fermilab, Batavia, IL 60510, USA

5. Present address: STX Inc., 4400 Forbes Blvd., Lanham, MD 20706 USA

6. Present address: University of Colorado, Boulder, CO 80309, USA

7. Present address: Dipartmento di Elettronica, Universita' di Pavia, Pavia, Italy

8. Present address: Fermilab, Batavia, IL 60510, USA

9. Present address: NIKHEF-H, 1009 DB, Amsterdam, The Netherlands

10. Present address: University of Alabama, Tuscaloosa, AL 35487, USA

11. Present address: Brandeis University, Waltham, MA 02254 USA

12. Present address: University of Illinois, Chicago Circle Campus, Chicago, IL 60637 USA

Abstract

The beam and spectrometer used in Fermilab Experiment 687 to study the photoproduction and decay of charm particles are described in detail. The photons are produced by a wideband electron beam which can operate at energies up to 600 GeV/c. The spectrometer consists of a high resolution silicon microstrip detector, a large aperture dipole magnet, proportional chambers, a second large aperture dipole, and more proportional chambers. Three multicelled threshold Čerenkov counters provide charged particle identification. Electromagnetic calorimeters outside the aperture of the second analysis magnet and at the downstream end of the spectrometer provide electron identification and photon reconstruction capability. A hadron calorimeter which follows the downstream electromagnetic calorimeter is used to trigger on events with hadrons in the final state and to reject purely electromagnetic events. Detectors for muon identification are located after the hadrometer and also outside the yoke of the second analysis magnet. The tracking system is capable of resolving the secondary decay vertices of charm and beauty mesons and baryons from the primary interaction vertex. It also determines the invariant mass of the multibody final states of particles containing heavy quarks with excellent resolution. The particle identification system, muon detection system, and electromagnetic calorimetry allow one to identify clearly the leptons, kaons, and protons present in these final states. This collection of detectors produces very clean signals for charm particles and permits one to make many cross checks of the apparatus. The performance is illustrated for a variety of charm signals. Of particular interest is a description of the tracking through the silicon microstrip detector and its use in isolating downstream decay vertices. Two complementary approaches to the reconstruction of secondary decay vertices are presented and insight is gained by comparing their strengths and weaknesses.

1 Introduction

The purpose of Fermilab experiment 687 is to study the production and decay of charm and beauty particles using a high intensity, high energy photon beam. Since charm production by photons occurs in roughly 10^{-3} of the hadronic events and beauty production at perhaps the 10^{-5} level, it is necessary to have a highly efficient, large acceptance multiparticle spectrometer, capable of operating at high rates.

The Fermilab Wideband Photon Spectrometer presented in Fig. 1 is a two-magnet spectrometer with large acceptance for charged and neutral hadrons and for muons, electrons, and photons. Charged particle tracking is accomplished by a silicon microstrip detector with 8,400 strips and a proportional chamber system with 13,400 wires. Three multi-celled Cerenkov counters provide charged particle identification. Neutral vees can be reconstructed over a decay path of about 10 meters. Photons and electrons are detected by two lead-scintillator arrays, one at the center of the aperture and one at large angles. Muons are detected over the full aperture by scintillation hodoscopes and proportional tubes inserted behind steel hadron filters. A gas hadron calorimeter is used in the trigger to reject purely electromagnetic events. This complement of detectors permits the observation of a wide variety of charmed baryon and meson decay modes. In particular, the microstrip system is designed to separate tracks coming from the downstream decays of charmed or beauty particles from those emerging from the primary production vertex [1]. The experiment has already presented results on charmed decays of the D^0, D^+, D_s^+, and the Λ_c^+ [2]. Examples of charm signals are shown in Fig. 2. In section II the photon beam and its instrumentation are described. In section III the spectrometer is presented in detail. Also included in this section is a description of the data acquisition system and the triggering criteria. Section IV presents techniques of data reconstruction and analysis including tracking, neutral vee reconstruction, particle identification, vertexing, calorimetry, and Monte Carlo simulation techniques. Section V is devoted to tracking in the target region with a special emphasis on the use of the silicon microstrip system to separate decay vertices from the primary interaction vertex and to perform lifetime measurements. Section VI presents various performance checks on the tracking and particle identification which demonstrate conclusively the capability of the detector.

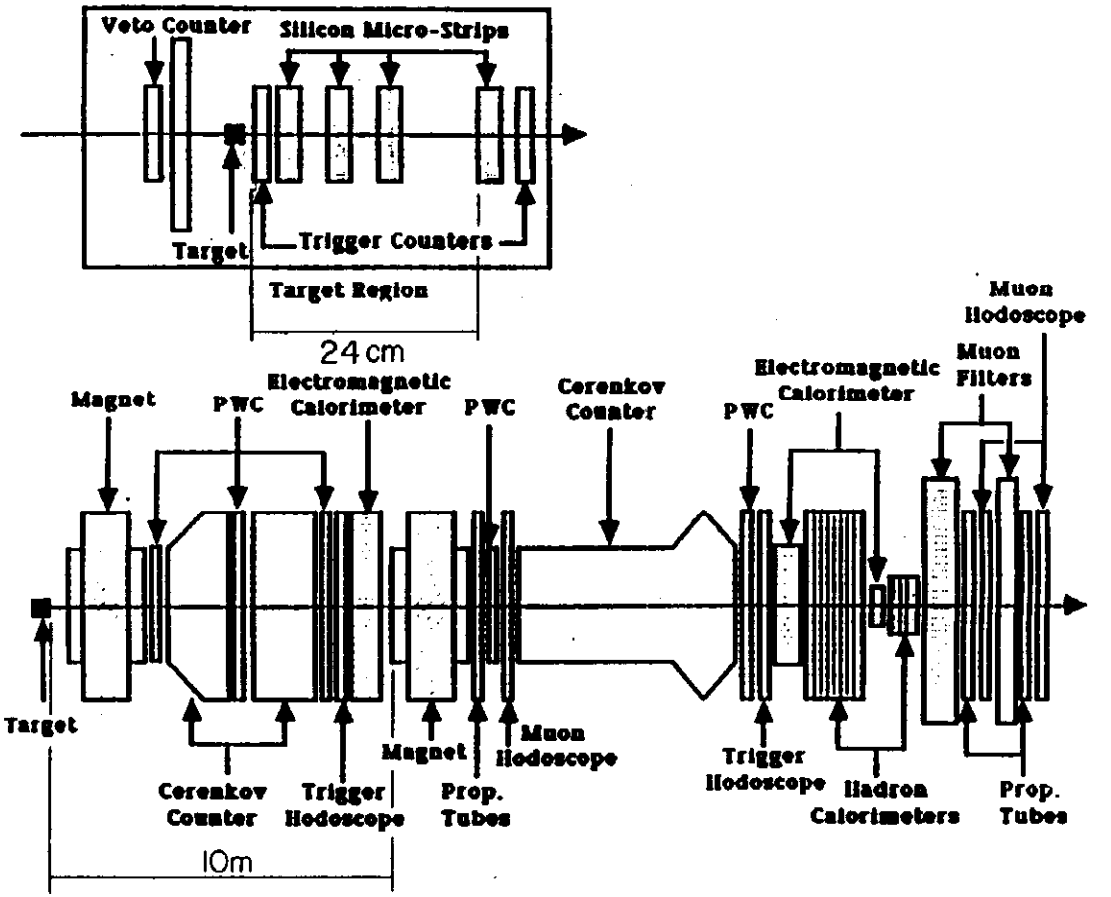

Figure 1

Schematic representaiton of E687 spectrometer. The inset at the top shows the target region and the silicon microstrip detector.

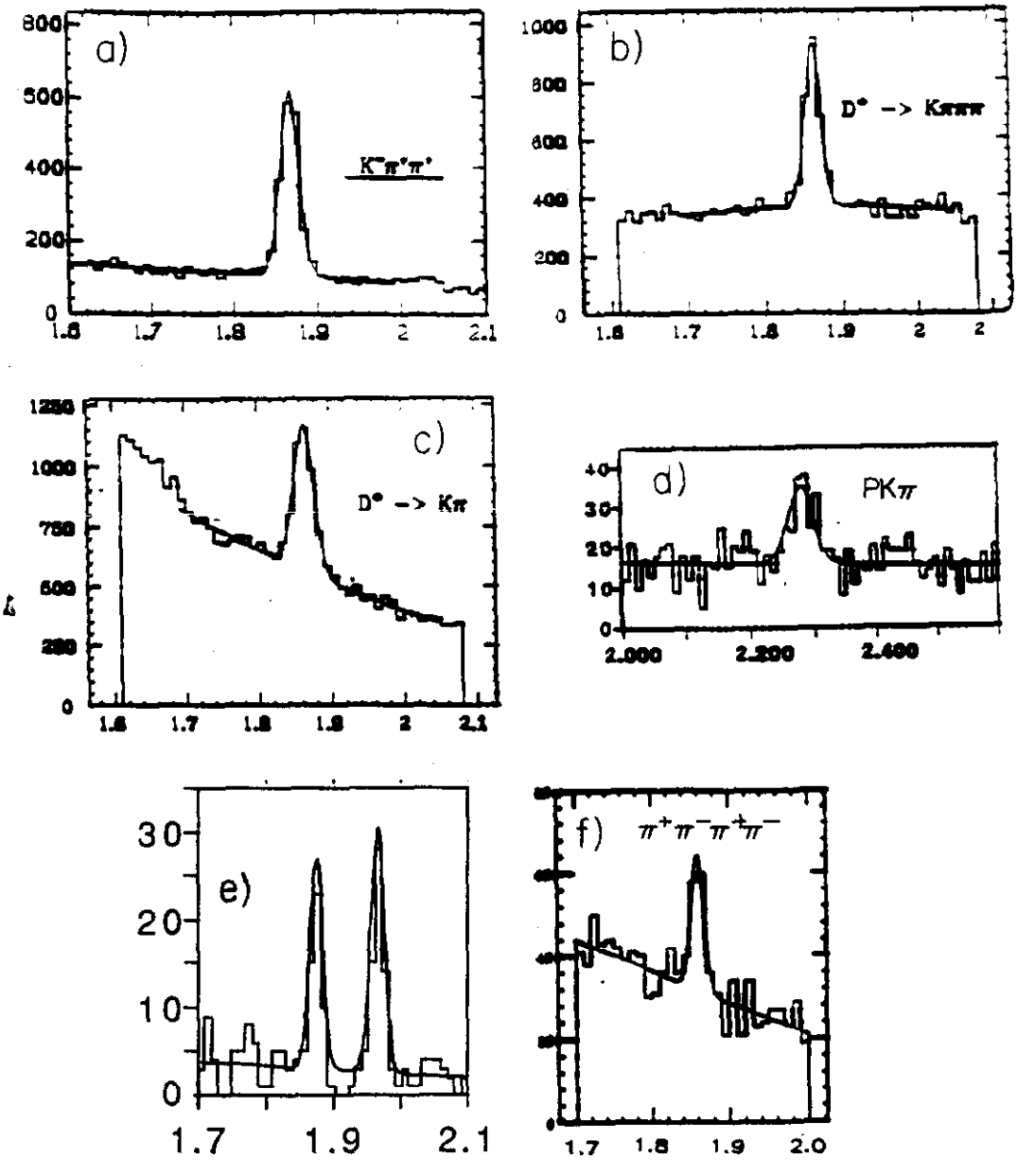

Figure 2: Examples of charm signals observed in E687 including: a) $D^{\pm} \to K2\pi$ b) $D^0 \to K3\pi$, c) $D^0 \to K\pi$, d) $\Lambda_c^+ \to pK\pi$, e) D^+ and $D_s^+ \to \phi^0\pi^+$, and f) $D^0 \to 4\pi$.

2 Photon Beam

2.1 Description, Yields, and Backgrounds

For many years, high energy photon beams have been recognized as a good place to conduct investigations of charmed particles[3]. The cross section is a relatively large fraction – approximately 1% – of the total hadronic cross section at high energies. The challenge was to develop a high energy and high intensity beam that produces enough charmed particles to obtain very high statistics so that one can answer really detailed questions about charm production and decays. The Fermilab Wideband Photon Beam is an attempt to meet that challenge.

At a proton accelerator, photons are derived indirectly from the strong interactions. One must solve two problems in order to make a clean photon beam: first, one must collect particles produced over a wide range of momenta and angles to form the beam; second, one must remove all the unwanted particles which are produced together with the photons. The unwanted particles include charged hadrons, π^+,π^-,K^+,K^-,p,and $\bar{p}$, as well as neutral particles such as neutrons and K_L^0's.

The photon beam is produced by the conventional "bremsstrahlung method" [4, 5]. This is accomplished as follows:

1. 800 GeV/c protons interact in a target, the "primary production target". Neutral pions are created and immediately decay into two photons. Immediately downstream of the target are sweeping magnets which remove all the charged particles. The photons emerge from the target box at zero degrees.

2. They then interact with a lead foil, the "converter",where they produce electron-positron pairs.

3. The electrons (more on this point later) are then captured by a conventional beam transport consisting of dipole magnets and quadrupoles. The electrons are bent away from zero degrees. Neutral hadrons, neutrons and K_L^0's, along with unconverted photons, travel straight ahead at zero degrees and are absorbed in a "neutral dump".

4. The electron beam is transported around the dump and is eventually passed through a thin lead foil, the "radiator", to produce photons by bremsstrahlung.The electrons are then deflected off to the side by dipole magnets,"electron sweepers", and into a dump, the "electron dump", while the photons pass straight ahead to the experimental target.

Figure 3 shows schematically the various steps required to produce a photon beam by this method. Figure 4 shows a schematic of the charged particle transport employed in the Wideband Photon Beam.

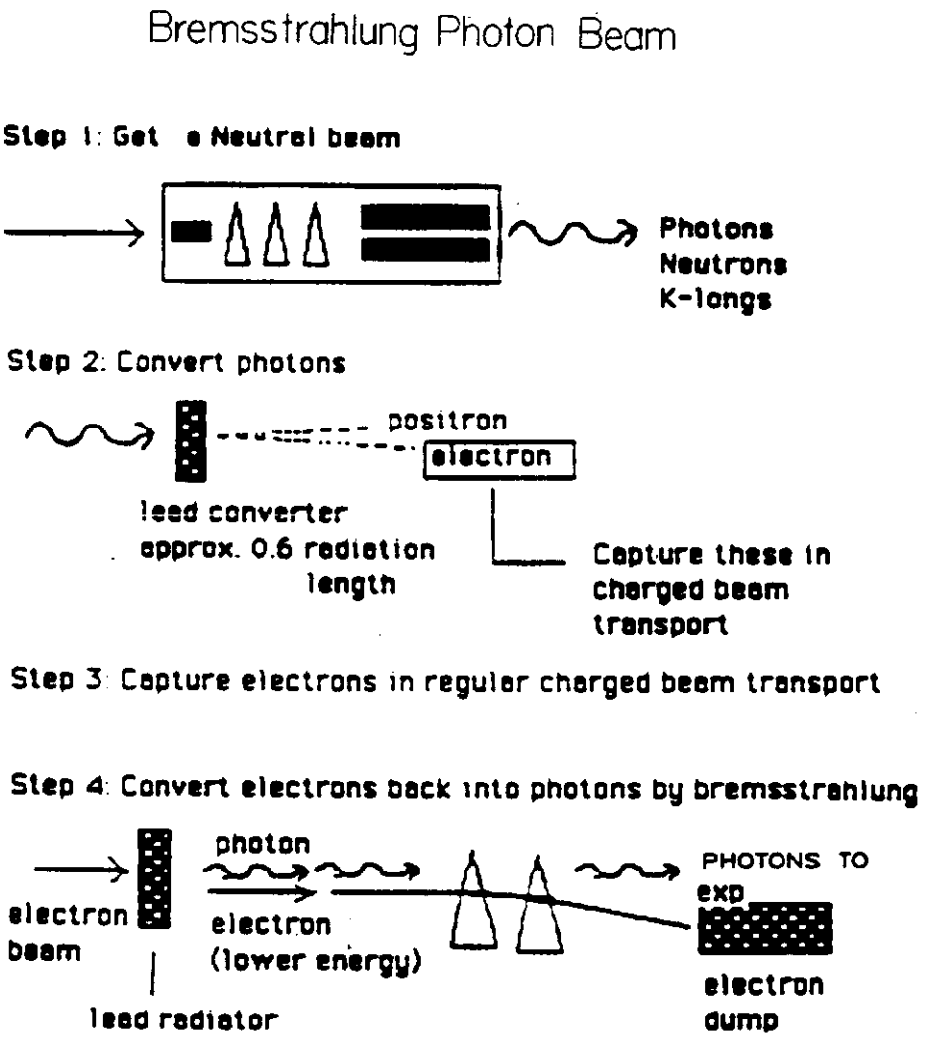

Figure 3: Steps required to produce a bremsstrahlung photon beam

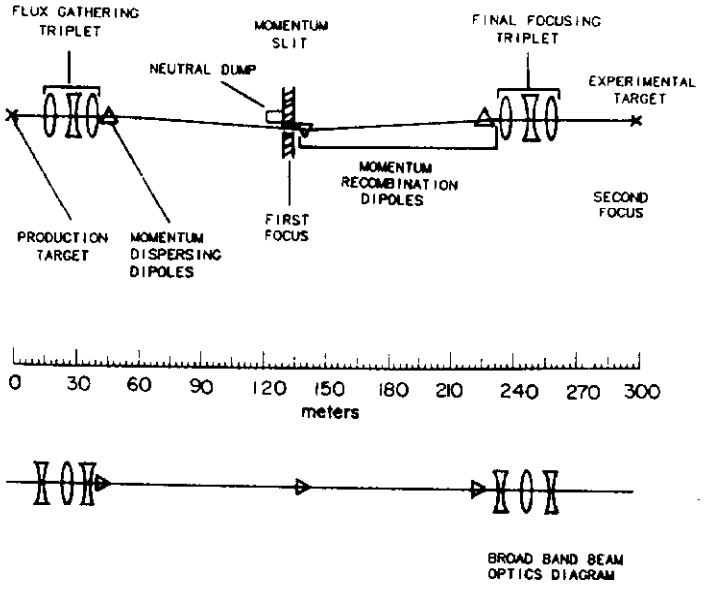

Figure 4: Charged particle transport for the Fermilab Wideband Photon Beam

The photons produced by this method have emerged from a chain of three interactions and one decay process: the primary interaction which produced a π^0 which then decayed to two photons; a conversion of one of the photons to an electron-positron pair; and the bremsstrahlung of the electron to a photon and an electron. The π^0 decay, the pair conversion and the bremsstrahlung interaction all degrade the final energy of the photon which emerges from the end of the chain. The photon beam is thus a 'tertiary' beam and it is difficult, using this method, to achieve high intensity, especially at high photon energies. The advantage of this technique is that it is relatively free from hadronic background compared to other methods. This is discussed in more detail below.

In order to achieve intense beams of high energy photons, it is crucial to collect electrons emerging from the converter over a very large range of angles and momenta. Since the electrons are charged, they may be collected by quadrupoles and it is possible to achieve large angular acceptance in this kind of beam while achieving a reasonably small beam spot on the experimental target. The optics of the Wideband Beam is arranged to collect electrons with a range of $\pm 15\%$ around a 'central' momentum setting.

The dipole arrangement in the secondary beam is a 'double dogleg'. It has two important features: first, there are no dipoles before the first set of quadrupoles and the bend angles in the dipole string in the center of the beam cancel each other so that there is no net first order momentum dispersion in the downstream quadrupole section of the beam; second, all the bends are very

Table 1: Wide Band Beam Properties

Horizontal spot size at production target	$\delta x = \pm 1 mm$
Vertical spot size at production target	$\delta y = \pm 1 mm$
Geometric horizontal angle accepted	$\delta\theta_x = \pm 1.0 milliradian$
Geometric vertical angle accepted	$\delta\theta_y = \pm 0.75 milliradian$
Geometric solid angle accepted	$\Delta\Omega = 6.0 \mu steradians$
Maximum momentum bite	$\frac{\Delta p}{p} \approx \pm 15\%$
Effective acceptance	$\Delta\Omega \times \frac{\Delta p}{p} \approx 96 \mu ster - \%$
Horizontal spot at experimental target	$\delta x = \pm 1.25\, cm$
Vertical spot at experimental target	$\delta y = \pm 0.75\, cm$
Horizontal divergence at experimental target	$\delta\theta_x = \pm 0.6\, milliradian$
Vertical divergence at experimental target	$\delta\theta_y = \pm 0.5\, milliradian$

small. The first feature keeps the beam relatively small as it passes through the quadrupoles. The second preserves the momentum acceptance in the double dogleg itself. The dipoles are all of the Fermilab '6-3-120' [6] type and have apertures which are 6 in. × 3 in.

In the upstream part of the beam, there is a flux-gathering symmetric quadrupole triplet, consisting of standard Fermilab '4Q120' magnets[7], which have 4 in. apertures. The field gradients are chosen to focus the low momentum components at the momentum slit in the middle of the double dogleg both vertically and horizontally. The high momentum components are not well focussed and are essentially parallel near the center of the dogleg. At the downstream end of the beam, another symmetric quadrupole triplet of 4Q120 magnets images both the highest and lowest momentum components of the beam onto the experimental target. Thus, in conventional terms, the beam is a 'two-stage' beam or 'point-to-point-to-point' for the low momentum components but is a 'one stage beam' with 'point-to-parallel-to-point' optics for the higher momentum components. The intermediate momentum components are not well-focussed. It is obvious that, while this arrangement produces high acceptance, it will not produce a small beam spot at the experimental target because most of the momentum components of the beam are not truly imaged at the target.

The parameters of the Wide Band Beam are shown in Table 1. The beam spot has a half width of over a centimeter at the base. This can be a disadvantage in some situations and an advantage in others.

The method by which the optics is arranged to achieve a large momentum and angle acceptance has been explained. Several other choices of parameters influence the final flux that can be achieved. These parameters are the material and thickness of the production target, the converter, and the radiator. Each has an 'optimum' value. One cannot make the production target too long because photons can convert as they travel from the production point to the end of the target. The converter cannot be made too thick because the elec-

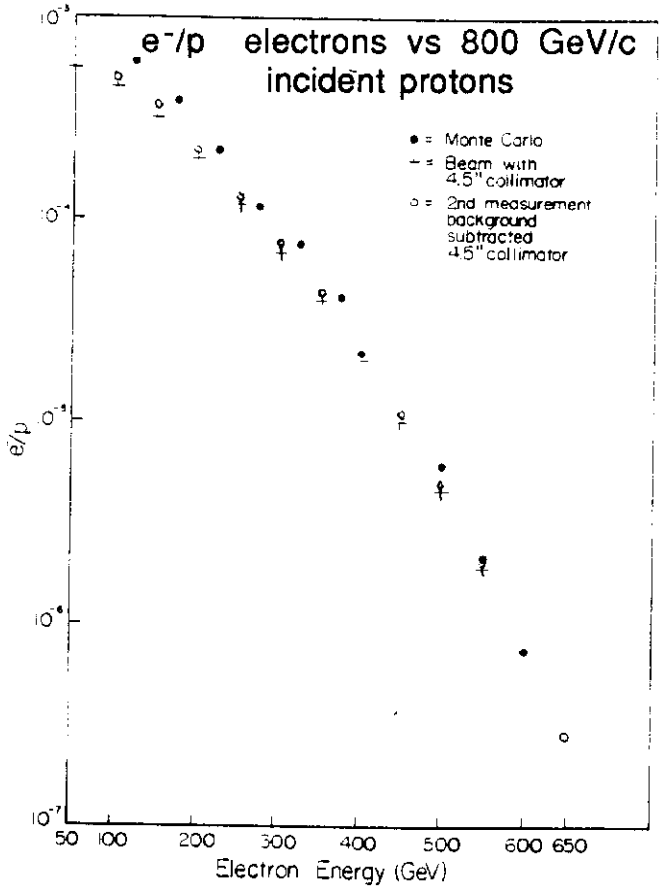

Figure 5: Electron yield per incident 800 GeV proton as a function of electron energy

trons radiate energy via bremsstrahlung as they travel through the radiator from the production point. Increasing the converter beyond a certain thickness will produce more electrons but will 'soften' the energy spectrum. The result is a reduction in the number of 'high energy' photons. Finally, if the radiator is made too thick many of the electrons give rise to more than one photon and this can make the interpretation of the events more difficult and can create rate problems in the detectors of the experiment.

A full calculation of the flux must include all these effects and is carried out by Monte Carlo techniques. Based on the Monte Carlo calculation, the production target was chosen to be 18 in. of beryllium and the converter was chosen to be 50% of a radiation length of lead. The radiator was chosen to be 20% of a radiation length of lead based on studies of the effect of multiple bremsstrahlung on the performance of the experimental apparatus, especially of the microstrip detector.

Figure 5 shows the measured electron yields per incident 800 GeV/c proton and compares them to the Monte Carlo calculation. For energies above 250 GeV, measured values are within 15% of the calculated values, consistent with the systematic uncertainties of the measurements and extrapolations used in the calculation. The photon spectrum obtained with the central e^- beam momentum set to 350 GeV/c is shown in the next section.

One major reason for using the bremsstrahlung style beam was to reduce the

hadronic background in the beam. The sources of this background are neutrons and K_L^0's in the beam. These neutral hadrons escape the target box along with the photons. When they strike the converter, a small fraction of them interact and may produce high energy charged hadrons which are captured by the secondary (electron) beam transport. If the secondary beam is set up to transport negatively charged particles, the background in the secondary beam is mostly π^-. If the secondary beam is set to transport positive particles, then the background is a mixture of π^+ and protons and is typically higher than for the negative setting. The relative number of protons also rises as the secondary beam energy approaches the primary beam energy. For these reasons, one always chooses to operate the secondary beam so as to capture and transport negative particles. The charged hadrons will eventually arrive at the 'radiator' where they may undergo hadronic interactions. These hadronic interactions are only a problem if they produce *neutral* particles that are at such small angles that they will eventually strike the experimental target. This means that they must be produced within a milliradian of the incident charged hadron. Any *charged* particles produced in these collisions will be removed by the 'electron sweepers' just downstream of the radiator.

Hadronic background comes from a sequence of events each of which has relatively low probability. The resultant background of neutral hadrons at the experimental target is, both from Monte Carlo calculation and from measurement, 10^{-5} neutrons per photon. The production of events by these neutrons is therefore under 1% of the photoproduction of events with hadrons in the final state.

The beam can be operated in a variety of modes to help calibrate experimental equipment. By turning the electron sweepers off and removing the radiator, one can bring the electron beam directly into the experiment and use it to calibrate the electromagnetic calorimeters. By inserting a lead absorber into this 'electron beam', one can remove the electrons and obtain a beam of π^- which can be used to calibrate the calorimeters. If a 10 ft long steel absorber is moved into the beam near the upstream end, all the electrons and pions are absorbed. The dominant flux through the detector consists of muons which have escaped from the primary target box. This so-called 'muon beam' is composed of high energy muons travelling at small angles to the central axis of the beam and spread out over the whole detector. It can be used for detector alignment, chamber efficiency studies, muon detector calibration, and many other purposes.

2.2 Beam Tagging System and Beam Gamma Monitor

The Wideband Beam has a simple photon energy tagging system. It is shown schematically in Fig. 6. Its purpose is to determine the energy of the interacting photon on an event-by-event basis. It also serves the function of requiring a selectable minimum electron energy loss in the radiator in the Level II trigger to effectively "harden" the bremsstrahlung spectrum.

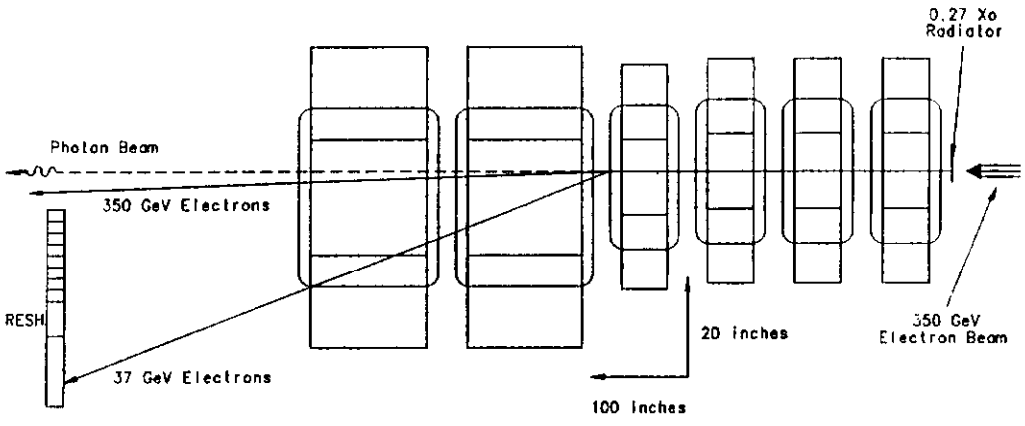

Figure 6: Schematic of Recoil Electron Tagging System

The incident electron, momentum selected by the Wideband Beam, strikes a lead radiator, producing photons by bremsstrahlung. The electron, after this energy loss, is momentum analysed in a magnetic spectrometer with the Radiated Electron Shower Hodoscope (RESH) as detector. Electrons are identified by a large energy deposition divided by momentum (E/p) in this RESH hodoscope. Multiple bremsstralung may occur in the radiator. Typically, only one photon interacts in the experimental target. The energy of any non-interacting photons is measured in a sero-degree shower counter, the Beam Gamma Monitor (BGM), located towards the end of the spectrometer. The physical properties of these detectors are given in Table 2.

The photon energy is calculated, on an event-by-event basis, from the following formula:

$$E_0 = E' + k_{interacting} + \sum k_{additional} \quad (1)$$

where:

Counter Name	Nominal Photon Tag (GeV)	Centerline Magnetic Deflection (in.)	Nominal Width (in.)	# Layers, Material, and Thickness
non-Radiating Electrons	0	4.03		
RESH 1	138	7.37	2.5	23 Pb,Lucite,1/4 in. each
RESH 2	205	9.98	2.5	"
RESH 3	235	12.56	2.5	"
RESH 4	254	15.14	2.5	"
RESH 5	268	17.72	2.5	"
RESH 6	278	20.30	2.5	"
RESH 7	286	22.88	2.5	"
RESH 8	293	25.46	2.5	"
RESH 9	302	29.79	6.0	20 Pb,Acrylic Scint,1/4 in.
RESH 10	310	37.54	11.5	20 Pb,Acrylic Scint,1/4in.
BGM	0		9 x 9	45, Pb,Lucite,1/8in. each

Table 2: Tagging Counter Specifications. The lead is stiffened with 6 % Sb by weight. The vertical (non-bend) size of the RESH counters is 6 in. The RESH 10 aperture is limited by the tagging magnet vacuum chamber wall.

E_0 is the incident electron energy, 350 GeV $\pm$50 GeV (σ). For this analysis, the incident electron is assumed to be the nominal 350 GeV beam energy.

E' is the energy of the electron after radiation as measured in the magnetic spectrometer and RESH hodoscope.

$k_{interacting}$ is the energy of the photon interacting in the experimental target producing the hadronic event detected in the E-687 spectrometer.

$\sum k_{additional}$ is the sum of the energies of any additional multiple bremsstrahlung photons produced by the electron in the radiator (and either not interacting in experimental target or interacting and striking the BGM counter).

Then, $k_{interacting} = E_0 - E' - \sum k_{additional}$.

The uncertainty in each of these terms limits the resolution in the estimate of the energy of the interacting photon. The major limitation is due to the $\pm$50 GeV energy spread of the incident electron beam. The photons cannot be tagged to a greater precision than this $\pm$50 GeV σ. For future runs, an incident beam magnetic spectrometer has been installed to measure the incident electron momentum to $\pm$2%. This system is described in Appendix B.

A second major concern is the multiple bremsstrahlung in the thick radiator. For most of the run, a 0.20 X_0 Pb radiator was used. There was an additional 0.07 X_0 effective radiator due to nearby beam monitoring scintillation counters and titanium vacuum windows. Therefore, the total effective radiator was 0.27 X_0.

2.2.1 Hardware

The magnetic field which bends the radiated electron was generated by six dipole magnets which were prototypes for the Fermilab Anti-proton Accumulator Ring[8]. They produced a $\int B \times dl$ of 89.5 kilogauss-meters at an operating current of 1190 Amperes. The distance from the effective bend point to the RESH plane (shower maximum) was 13.335 m. The non-radiating nominal 350 GeV electrons were deflected 10.24 cm from the photon beamline and struck a lead and steel dump. The dipole sweeping magnets were offset to the west to increase the horizontal aperture and good field region for the radiated electrons.

The RESH hodoscope counters were either lead-lucite or lead-acrylic scintillator shower counters of about 24 X_0 depth. The RESH counters were outfitted with RCA 8575 photomultiplier tubes and transistorized bases [9].

Table 3: RESH patterns considered valid by trigger logic

	RESH(i)	a single hit
or	RESH(i)×RESH(i+1)	two adjacent hits
or	RESH(i-1)× RESH(i)×RESH(i+1)	three adjacent hits

The BGM is a lead-lucite shower counter (45 layers of 1/8 in. Pb (+ 6% Sb) and 1/8 in. lucite) of 24 X_0 depth with bent lucite light pipes leading to a Amperex 58AVP photomultiplier tube with a 9 stage resistor base [10].

The RESH counters and BGM had CAMAC-controlled pulsed LED's for performance and gain monitoring.

Since this tagging system was intended to operate at high rates, it was important to minimize the time resolution, and to have pulse pair resolutions of one RF bucket (18.8 ns) if possible. The coincidence resolving time for the coincidence registers was approximately 4 ns. Due to problems with the ECL gate driving circuit feeding the LRS 1885 ADC's, the minimum gate widths for RESH and BGM were 38 nsec, corresponding to two RF buckets.

2.2.2 Use of RESH in Triggering

The typical energy deposition in an individual RESH(i) counter is shown in Fig. 7. There is a prominent peak due to the momentum analysed radiated electron striking near the center of the individual RESH(i). There is a tail on the low energy deposition side due to transverse shower leakage for electrons striking that RESH near either of its side edges. There is also a tail extending upward from pedestal due to radiated electrons striking an adjacent RESH(i-1) or RESH(i+1) hodoscope cell with some energy deposited in RESH(i) due to transverse shower spread. Such shower sharing between adjacent RESH counters can be used to localize the electron impact point to considerably better resolution than the RESH counter width. Due to the resolution limitations inherent in the untagged incident wide band electron beam, a simpler tagging algorithm was used.

A discriminator threshold was set at approximately 20% of the nominal radiated electron peak for each RESH counter. This logic signal was latched in a coincidence register gated by the MASTER GATE (MG). The output of this latch was then sent to a LeCroy LRS 4516 Programmable Logic Unit (PLU). This PLU then passed the RESH hit patterns to the Level II trigger logic, consistent with a single electron striking RESH. The valid patterns are shown in Table 3. Since the triple adjacent hit pattern occurred less than 1% of the time, this triple pattern was cut in the offline analysis.

There were three levels of RESH signals passed from the RESH PLU to the Level II trigger corresponding to:

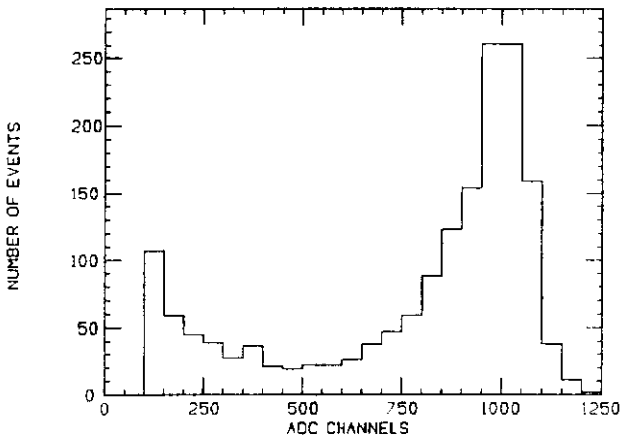

Figure 7: Typical RESH counter pulse height spectrum

1- RESH-LOW nominal electron energy loss greater than 116 GeV
2- RESH-MED nominal electron energy loss greater than 193 GeV
3- RESH-HIGH nominal electron energy loss greater than 212 GeV

It is again noted that the electron energy loss represents the sum of the energies of the radiated photons. Most of the data was taken using the RESH-LOW threshold.

The use of the patterns for the 10 single RESH hits and the 9 adjacent RESH hits provided 19 photon energy tagging bins. This is more than adequate since the difference between adjacent bins was typically smaller than the incident electron beam momentum uncertainty.

2.2.3 Performance

Photon Tagging System performance data were taken during dedicated runs where either an electron beam was taken directly to the BGM counter or a photon beam was used, but with a simple charged particle trigger with the spectrometer analysing magnets OFF to allow converted pairs to strike the BGM. This allowed cross calibration and monitoring of the RESH and BGM systems. Figure 8 shows the electron beam energy Distribution measured calorimetrically in the BGM shower counter. The photon beam energy distribution is shown in Fig. 9, for a 0.27 X_0 effective radiator. There is no requirement of a RESH tag in this spectrum. The spectrum shape is fitted with the form

$$\frac{dn}{dq} = \frac{1}{q^{\alpha}} \times \frac{1}{1 + exp[\frac{q - q_{end}}{\lambda}]} \qquad (2)$$

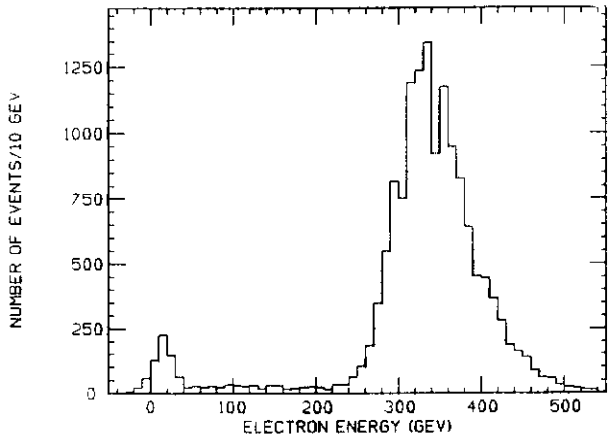

Figure 8: Electron beam energy distribution for 350 GeV central beam setting

Table 4: Fit parameters for description of photon spectrum

α	=	0.73 ± 0.02
e_{end}	=	398 GeV $\pm$ 3 GeV, the endpoint of the photon spectrum, related to the incident electron beam energy
λ	=	28 GeV $\pm$ 1 GeV, the incident electron energy spread.

where q is the total energy of all the photons radiated. Fitted values are given in Table 4.

A 'thick target' bremsstrahlung Monte Carlo calculation predicts $\alpha = 0.73$ for the distribution of q, the sum of the photon energies or the electron's energy loss for a 0.27 X_0 radiator, in good agreement with the experimental distribution.

Figure 10 shows the tagged (electron energy loss) photon spectrum, integrated over all accepted RESH tagging hit pattern configurations. Figure 11 shows the Photon Tagging Efficiency obtained by dividing the Tagged Photon Spectrum without RESH trigger requirement into the same distribution requiring the RESH-LOW trigger to be set. Typical tagged photon spectra (measured in BGM) for selected tagging RESH hit patterns are shown in Fig. 12.

Figure 13 shows how the RESH and BGM work together in determining the event energy on an event by event basis. Plotted first is the electron energy loss from RESH minus the J/ψ energy for quasi-elastic events determined from the magnetic spectrometer. The assumed incident electron energy is 350 GeV. The energy does not balance due to extra multiple photons that are coincident with the photon producing the J/ψ but are not accounted for. By subtracting also the summed energies of these non-interacting photons hitting the BGM counter, the energy balance is improved, as shown in the second plot where the energy

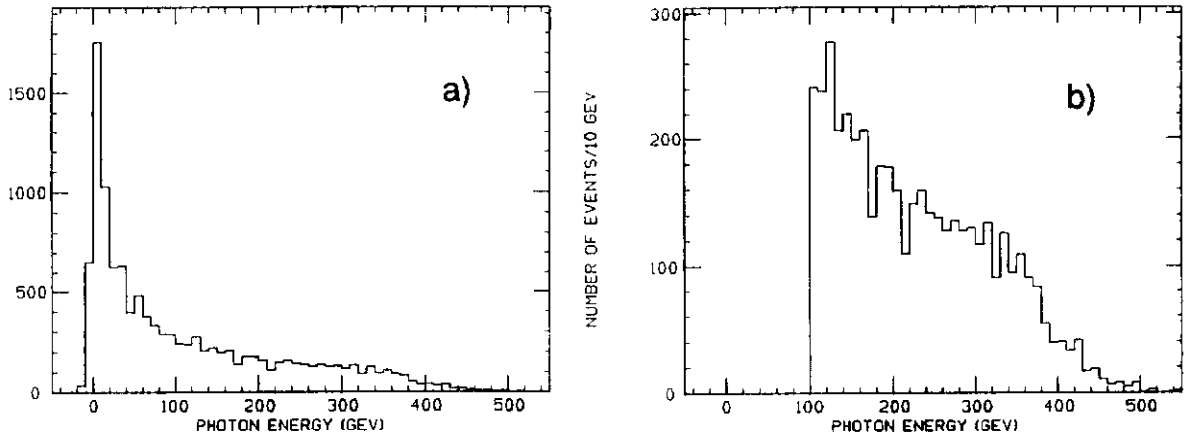

Figure 9: Photon spectrum obtained from 350 GeV electrons a) all energies; b) energies greater than 100 GeV.

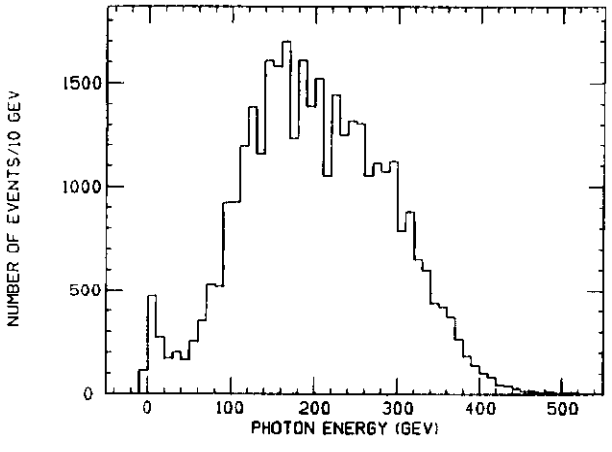

Figure 10: Tagged photon spectrum

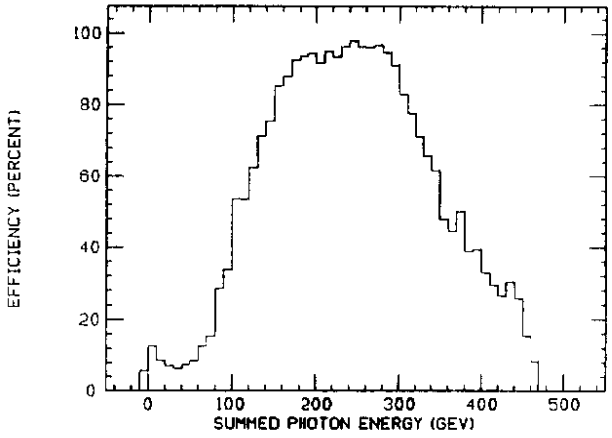

Figure 11: RESH Photon tagging efficiency vs energy

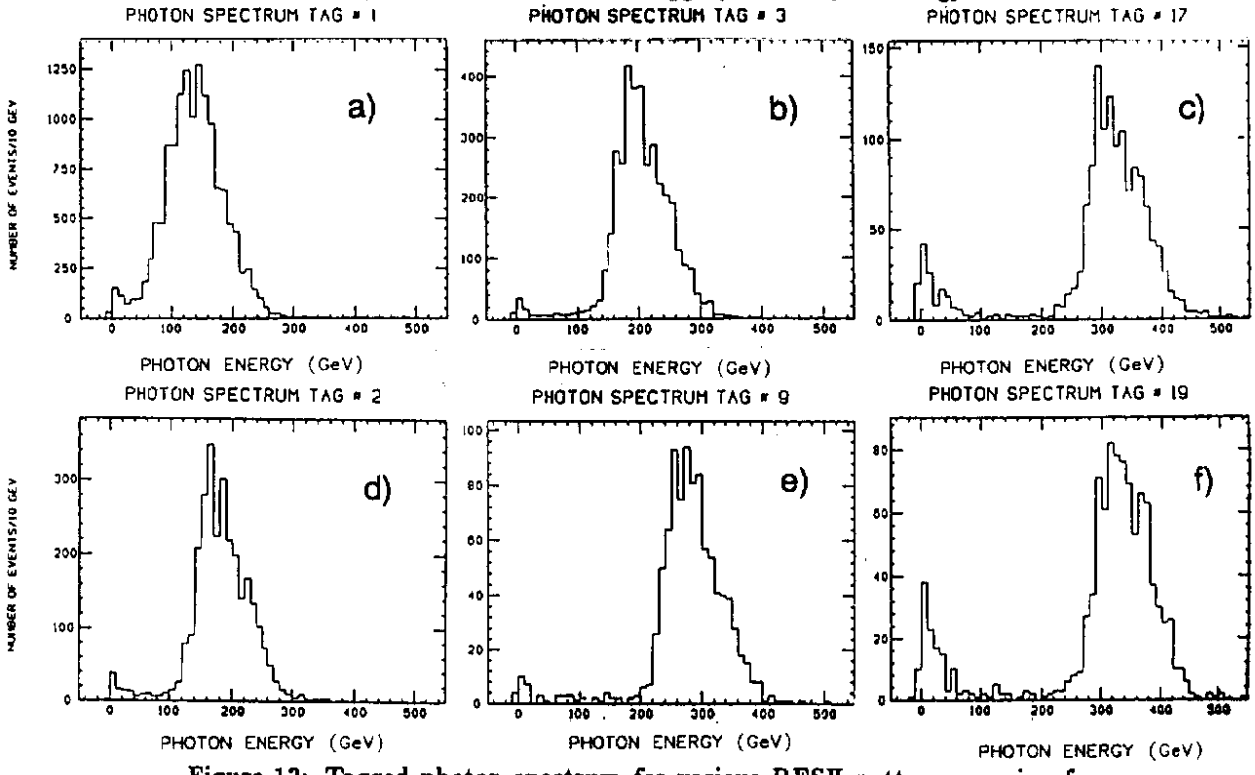

Figure 12: Tagged photon spectrum for various RESH patterns ranging from the lowest energy a) to the highest f)

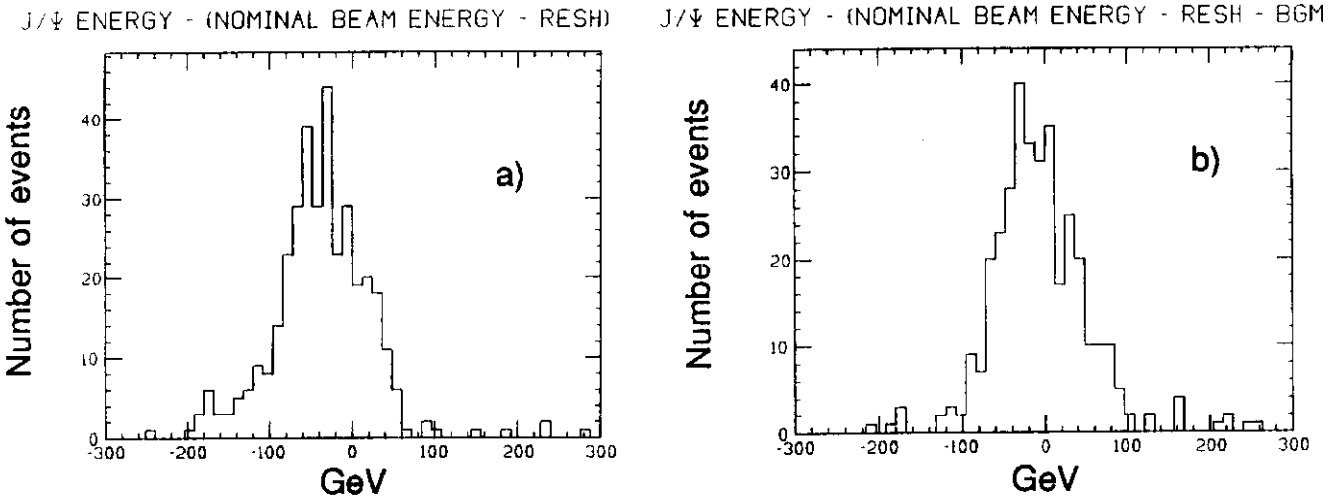

Figure 13: Energy balance between elastic J/ψ and calorimetric photon energy a) without Beam Gamma correction; b) with Beam Gamma correction

spread (σ) is consistent with the uncorrected beam momentum spread and the tail on the low side has disappeared.

2.2.4 Problems and Future Solutions

The problem of the incident beam momentum spread and its solution using a beam spectrometer were mentioned above.

A second serious problem occurs due to second order processes in the thick radiator. Some of the photons produced can be re-converted into e^+e^- pairs within the radiator. This will either lose photons destined to strike the experimental target, leading to a mis-measured flux, or produce "false tags". These false tags can be generated when an incident electron suffers only a small energy loss within the radiator. It is not deflected sufficiently to register in the RESH hodoscope, but strikes the electron dump. A photon radiated by this electron can pair-convert in the radiator, possibly having the electron from the pair fall within the RESH acceptance. This is a more serious background as the apparent tagging energy increases. The bremsstrahlung tail near zero energy in the BGM can be seen to increase as the tagging energy increases in Fig. 12 a through Fig. 12 f. These backgrounds will be identified in future runs by adding dump counters at the electron dump and shower counters on the positron side of the sweeping magnet.

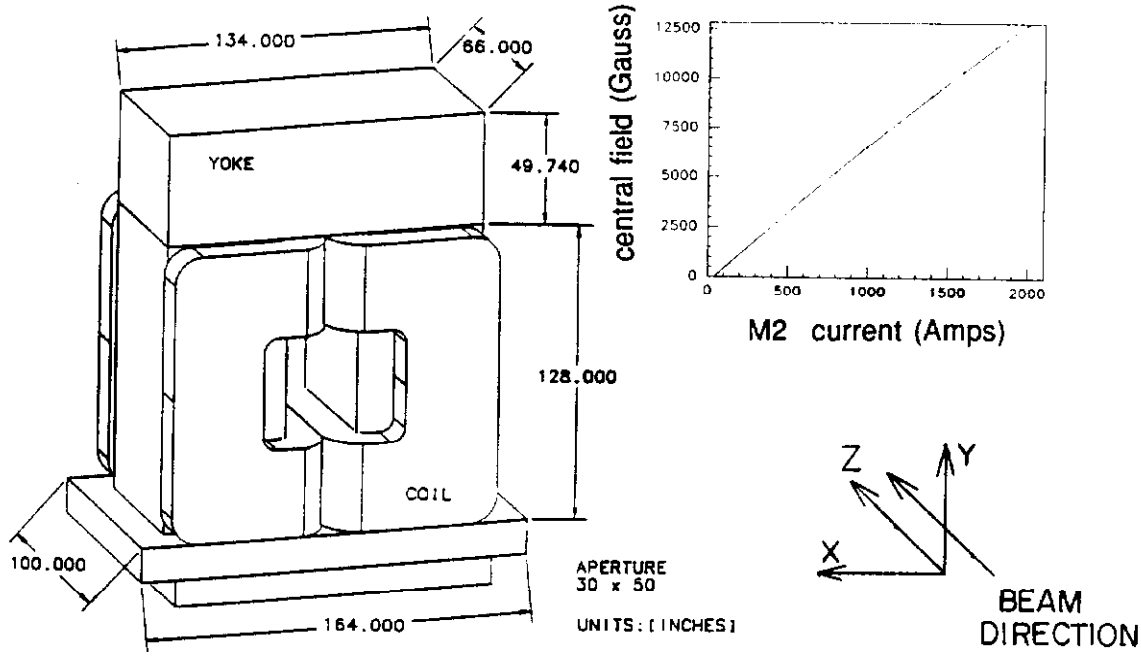

Figure 14: Picture of spectrometer analysis magnet

3 Spectrometer

3.1 Analysis magnets

Momentum analysis of charged tracks is achieved by measuring their deflection in two large aperture dipoles, designed especially for use in multiparticle spectrometers in the Fermilab Tevatron II program[11]. The two dipoles are identical except for the details of the magnetic shield plates on their ends. Figure 14 is a drawing of one of these magnets. The magnet is oriented to deflect charged particles vertically. The inset is the magnet's excitation curve, taken with a Hall probe near the center of the magnet. Also shown, is the coordinate system used to describe the spectrometer: the z axis is along the beam direction with downstream being more positive; the y axis is vertical with up the positive direction; and x is horisontal with the positive direction chosen to form a right-handed system with the y and z axes. The magnets have a maximum p_t kick of 1 GeV/c. The first magnet, M1, is operated at a kick of 0.400 GeV/c and the second magnet, M2, has a p_t kick of 0.850 GeV/c. M1 and M2 bend in *opposite* directions. The ratio of the kicks is arranged so that charged tracks return to their original undeflected position toward the downstream end of the spectrometer, nominally near the inner electromagnetic calorimeter (IE). The properties of the magnets are listed in Table 5.

This particular arrangement of magnet orientation and currents has the following effect on event topology. There is a very large rate of e^+e^- pairs coming

Table 5: Analysis Magnet Specifications

Central field	14.0 kilogauss
Maximum p_t kick	0.97 Gev/c
Field uniformity	$\pm 2.5\%$
Steel yoke length	66 in.
Effective length	101 in.
Effective length/pole length	1.55
Total length	104 in.
Maximum current	2500 amps
Voltage at max current	160 Volts
Total power at max current	400 kW
Total flow (50% glycol)	118 gpm
Pressure drop across coils	150 psi
Conductor diameter	1.855 in. x 1.375in.
Water passage diameter	0.61in.
Total weight	272 Tons

from the experimental target. These events must be suppressed with high efficiency by the experiment's trigger. They are produced with little transverse momentum so they populate a region which is approximately the size of the beam. After they pass through the first analysis magnet, they are dispersed into a vertical swath whose horizontal width is again just the horizontal beam size. They are bent back towards the beam axis by M2. The lowest energy particles strike either the pole tips of M1 or the upstream face or pole tips of M2. The surviving particles come together to reconstitute the beam profile at the end of the spectrometer. The momentum recombination is somewhat smeared by the loss of energy of the electrons and positrons via bremsstrahlung in the material of the spectrometer. Hadronic final states are much more spread out in angle. The geometric distribution of electromagnetic events, shown schematically in Fig. 15, is exploited by the trigger. Most hadronic events, and nearly all events containing charm or beauty, will have at least two particles outside the pair region at the downstream end of the spectrometer and will produce counts in the HxV hodoscope. Electromagnetic pairs will only rarely produce counts in this hodoscope.

The data analysis requires a very precise knowledge of the shape of the magnetic field. This is particularly important for the reconstruction of neutral vees decaying into charged tracks inside M1. The fields of the analysis magnets were measured using the Fermilab Ziptrack device[12]. The Ziptrack consists of a set of 3 orthonormal coils mounted in a small cart. This cart moves along a rigid aluminum rail which extends through the aperture of the magnet and is supported at both ends by a motorized positioning device. The rail lies along

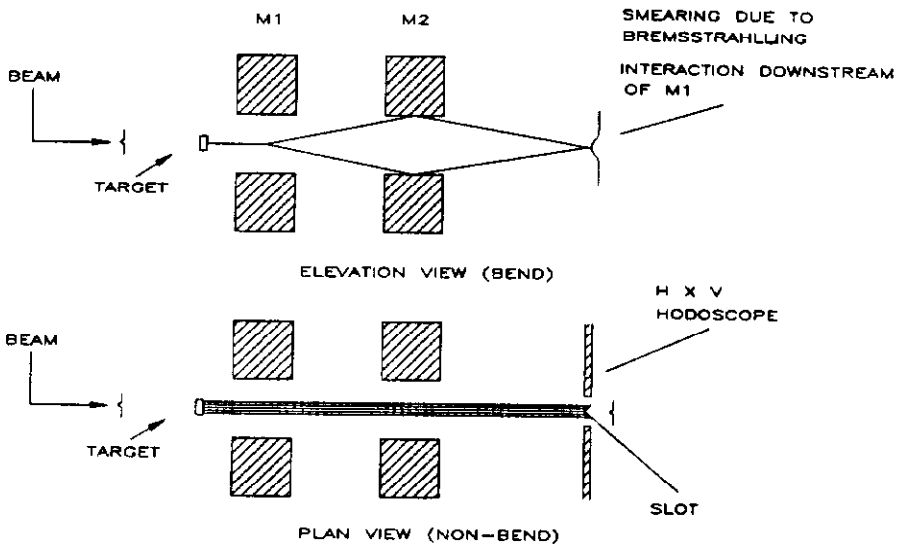

Figure 15: Schematic plot of the geometric distribution of electromagnetic events

the s axis (photon beam direction). The procedure is to position the rail at some (x,y) position and then the cart is pulled at an approximately constant rate of speed along the rail. The charge created by the induced EMF in each coil is measured by a precision ADC at a selectable interval; in this case the interval was about 2.5 cm. The entire operation of the Ziptrack including positioning of the rail and recording the ADC data was controlled by a PDP11 series computer through a simple command interface.

The data from this procedure consisted of 9x9x400 (x,y,z) points with 2 measurements of (B_x,B_y,B_z) at each point (down and back on the cart trip). Surveys of the cart in its 'start location' approximately positioned these field measurements with respect to the spectrometer coordinate system.

A field map is obtained from this data by fitting the x-y behavior of the 3 components of the field every 2.5 cm in s. The fit chosen was a polynomial in x and y with s-dependent coefficients of the form:

$$B_i = \sum_{m,n} C_{mn}^{(i)}(z)\, x^m\, y^n, \qquad (i = x, y, z) \tag{3}$$

It was possible to orient a magnetic coordinate system where B_x , the dominant field component, has reflection symmetry in both x and y. This meant that terms in the B_x polynomial containing odd powers of x and y up to and including terms with $m+n=4$ were set to zero. This gave 6 non-zero coefficients

$C_{00}^{(s)}$, $C_{20}^{(s)}$, $C_{02}^{(s)}$, $C_{22}^{(s)}$, $C_{04}^{(s)}$. and $C_{40}^{(s)}$. The Maxwell relation $\vec{\nabla} \times \vec{B} = 0$ allows one to express all $C_{ij}^{(y)}$ and $C_{ij}^{(x)}$ coefficients in terms of the six allowed $C_{ij}^{(s)}$ coefficients. Up to $m + n = 4$ there are 3 nonzero $C^{(y)}$ and 3 $C^{(x)}$ terms. It turned out that the B_s field of E687 analysis magnets had rather weak y^2 dependences and higher quality information on $C_{02}^{(s)}$ and $C_{04}^{(s)}$ could be obtained from fits to the B_y field.

Several effects had to be corrected in the data before this fit produced useful results:

- The integrators accumulated excess charge at a rate linear in time and calculable from the difference in starting and ending values of the field for each "zip" in z.
- The field data had to be scaled to match NMR measurements of the central field and Hall probe readings of the fringe field at the start and end points on each side of the magnet.
- The coordinate system of the positioning device was not orthonormal or precisely aligned with the magnet symmetry axes. These errors, typically a few milliradians, affected the actual (x,y,z) position of the cart at each of the measurement points.
- The coil axes (inside the Ziptrack cart) were also not orthonormal or precisely aligned. These misalignments caused apparent violations of Maxwell's equations in the measured field.

The coordinate system and coil rotation angles were corrected empirically by looking for reflections of the 'symmetry allowed' components into other 'symmetry forbidden' coefficients. For example a $C_{00}^{(y)}$ coefficient that had the same shape as the main component $C_{00}^{(s)}$ would indicate that the B_y coil was not oriented perpendicular to the x-axis. The size of the $C_{00}^{(y)}$ coefficient would indicate the rotation angle. Similarly a nonorthogonal orientation of the 3 probes will create an apparent violation of Maxwell's equation:

$$\vec{\nabla} \cdot \vec{B} = C_{10}^{(s)} + C_{01}^{(y)} + \frac{\partial}{\partial z} C_{00}^{(z)} = 0 \qquad (4)$$

The z-dependence of the apparent divergence can be used to find the nature of the probe nonorthogonality. Rotations of this type were applied to the data and the fits redone. When the 6 rotation angles associated with the coils, 6 angles for the positioning apparatus and 3 offsets for the positioner were adjusted, the resulting fits satisfied Maxwell's equations and all 'symmetry forbidden' field components disappeared. At this point the fit was redone and only the Maxwell allowed symmetry terms were allowed to contribute. Figure 16 shows the results of these fits by comparing the Maxwell related terms $(\partial B_s/\partial z, \partial B_z/\partial x)$ and $(\partial B_s/\partial y, \partial B_y/\partial x)$ as functions of z. The agreement with Maxwell's equations is seen to be excellent.

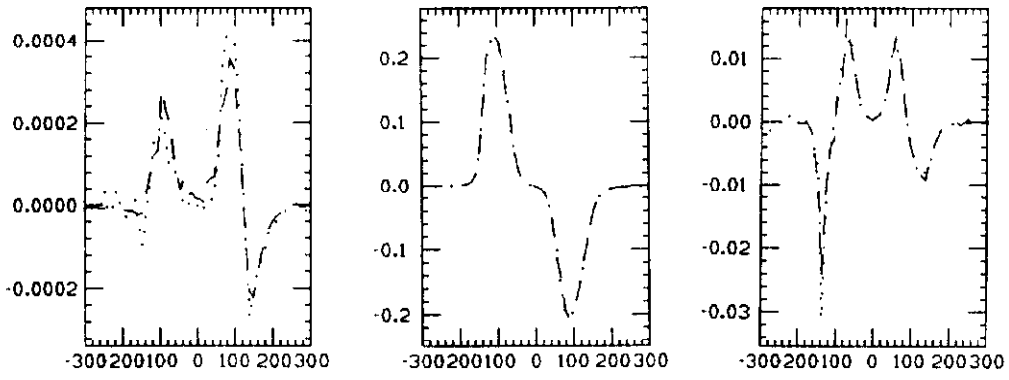

Figure 16: Comparison of Ziptrack fit to Maxwell's equations:
a) $\partial^2 B_x/\partial y^2$ (dots) and $\partial^2 B_y/\partial x \partial y$ (dashes) from curl B,
b) $\partial B_x/\partial z$ (dots) and $\partial B_z/x$ (dashes) from curl B, and
c) $\partial^2 B_x/\partial x^2$ (dots) and $-\partial^2 B_x/\partial z^2$ (dashes) derived from the divergence of B.

3.2 Target

During the run, two different targets were used in the experiment : a beryllium target and an active silicon target.

The beryllium target, shown in Fig. 17, was composed of 5 blocks, with a thickness of 4 mm each, separated by thin air gaps. The *diamond shape* of the downstream 3 blocks was designed to match the high resolution region of the first station of the microstrip detectors. The total length was $\sim$ 4.5 cm corresponding to a radiation length of $\sim$ 11.5 % and an interaction length of 10%.

The active target consisted of 48 silicon detectors [13] with an active area of 2 cm $\times$ 2 cm, divided in four equal regions, as shown in Fig. 18, and a thickness ranging from 200 μm to 250 μm. The detectors were assembled in an alternate crossed geometry to provide a transverse resolution of 5 mm $\times$ 5 mm. To increase the interaction probability in the first region of the target, twenty nine 300 μm thick beryllium layers were inserted among the first detectors; the resulting length of the target was $\sim$ 2.7 cm , corresponding to $\sim$ 14% of a radiation length and $\sim$ 4.7% of an interaction length.

This configuration permitted the reconstruction of secondary vertices by looking at the multiplicity steps along the active target and the direct detection of the primary vertex by means of the large amount of released ionization charge when the interaction took place in the Silicon detectors.

The beryllium target was employed for the major part of the data taking,

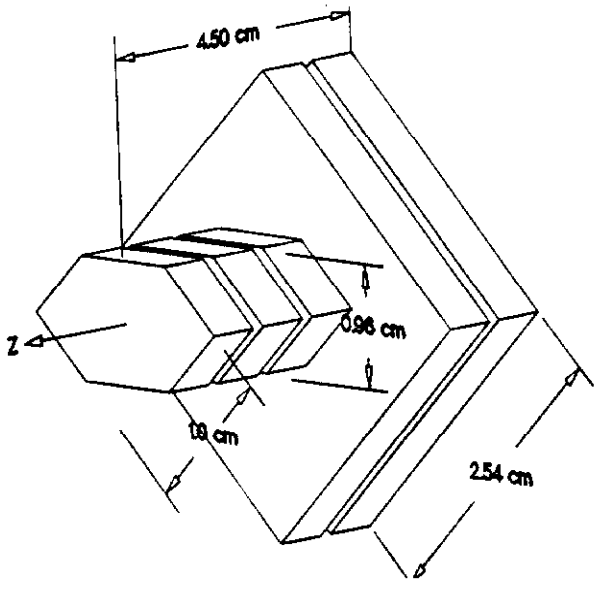

Figure 17: Beryllium experimental target

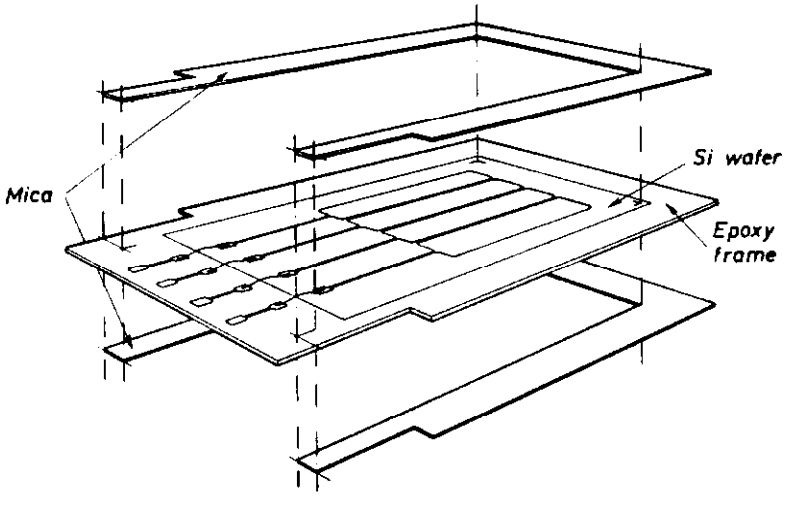

Figure 18: Silicon wafer used in active target

the silicon target only for a small fraction equivalent to about 10 %.

3.3 Trigger counters

A two level trigger is used. The first level trigger rejected a large fraction, approximately 90%, of the electromagnetic interactions of the photons and vetoed possible charged particles coming with the beam; the second level trigger required a certain amount of energy deposited in the hadron calorimeter or at least two muons. In addition, the trigger required at least one hit in the upstream PWC outside the region populated by e^+e^- pairs. The hadron calorimeter and PWC requirement rejected more than 98% of the electromagnetic events surviving the first level trigger.

The first level trigger made use of the scintillator counters A0, AM, TM, TR1, TR2, OH and HxV.

The purpose of the first 3 counters (A0, AM, TM), placed transverse to the beam upstream of the target, was to detect and reject any charged particles (typically muons of the beam halo) travelling inside and close to the photon beam. The AM array was a set of 24 scintillator counters (25.4 cm × 58.4 cm each) of total dimensions 1.5 m × 2.5 m, placed ~ 8 m upstream of the target; TM was composed of 2 scintillator counters of dimensions 45.7 cm × 61 cm placed ~ 2.5 m upstream of the target. Both these sets of detectors surrounded the beam pipe. A0 was a small scintillator (7.6 cm × 4.5 cm) placed inside the beam line about 7 m from the target to veto charged particles coming right down the beam pipe.

The TR counters, TR1 and TR2, were designed to detect the charged particles coming from the target, so the coincidence between TR1 and TR2 indicated that an interaction with at least one charged particle occurred in the target. TR1 was a small scintillator (3.5 cm × 2.5 cm) placed ~ 3 cm downstream of the target and just in front of the microstrip detectors; TR2 was a scintillator counter of dimensions 22 cm × 22 cm placed downstream of the microstrip detectors, at ~ 45 cm from the target. The discriminator thresholds were set so that these counters produced logic signals to the trigger electronics for single minimum ionising particles. Thus, these counters were sensitive to e^+e^- pairs, dimuons, dihadrons, and multihadronic final states.

The purpose of the last two arrays of counters, OH and HxV, was to reject the electromagnetic interactions of photons and to select hadronic events. OH was one plane of 24 scintillators covering the upstream face of the electromagnetic calorimeter (OE). It was designed to detect wide angle charged particles outside the center gap (~ 88 cm × 51 cm) of the plane (Fig. 19). The HxV array was located downstream of the P4 chamber; it consisted of two adjacent planes of scintillators with 24 and 12 counters placed horizontally (H) and vertically (V), respectively (Fig. 20). Each plane was divided in two halves positioned side by side with a horizontal separation of ~ 7.6 cm between them. Signals coming from these two detector arrays, OH and HxV, were organized in a suitable logic

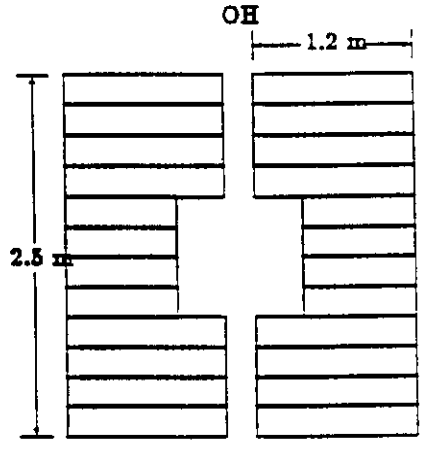

Figure 19: OH counter geometry

to define a pair of particles both of which were out of central gap and therefore much more likely to be from a hadronic interaction than a purely electromagnetic one.

3.4 Tracking

3.4.1 Microstrip Detectors

Tracking in the region between the target and the first magnet is performed by a system of silicon microstrip detectors, shown schematically in Fig. 21. The system [14] was designed to achieve the very high position accuracy needed to separate the decay vertices of particles containing heavy flavors from the interaction vertex, while, at the same time, minimizing the total number of electronics channels (for cost reasons).

It consists of twelve microstrip planes grouped in four stations of three detectors measuring i, j and k coordinates respectively: i at $-135°$, j at $-45°$ and k at $-90°$ with respect to the horizontal z axis of the spectrometer reference frame.

The innermost central region of the system, covering the very forward production cone, has a resolution two times better than the outer one. This region is crossed by the most energetic tracks which are very close to each other and are less affected by Multiple Coulomb Scattering (MCS). The first station, which is the most crucial in determining the extrapolated error to the production point in the target, has twice the position accuracy of the others.

The geometry of the microstrip system is described in Table 6. All the detectors of the system are mounted on a high precision granite support which ensures correct alignment to better than $\pm 3\mu$m over 5 cm. Actually, there are four granite frames, each of them holding the three detectors of a station. The

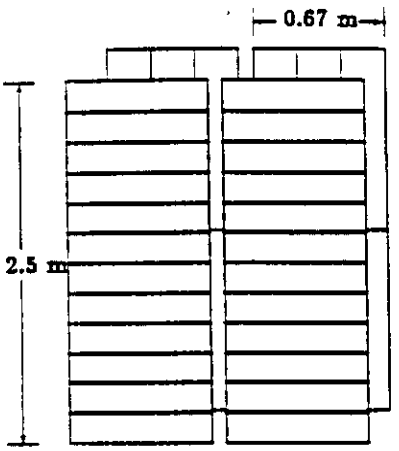

Figure 20: HxV counter geometry

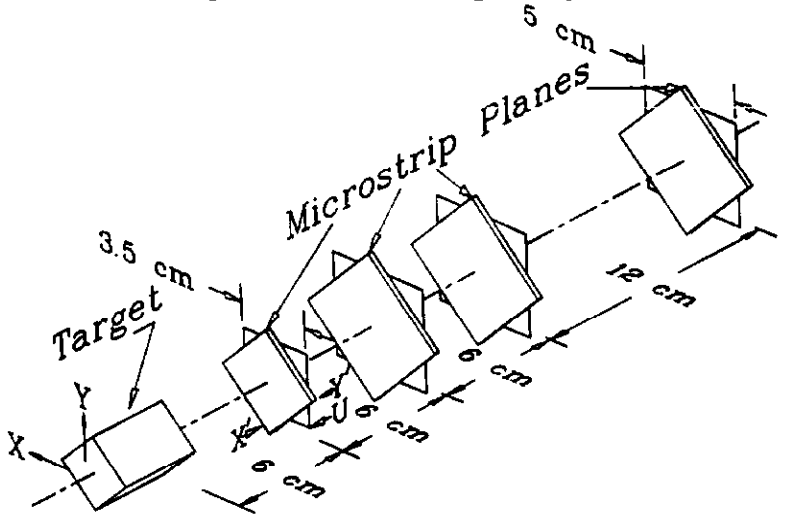

Figure 21: Silicon microstrip detector layout

Table 6: Properties of the Silicon Microstrip Detector

	I station	II station	III station	IV station
z position:				
1st detector	-.5 cm	5.5 cm	11.5 cm	23.5 cm
2nd detector	0.0 cm	6.0 cm	12.0 cm	24.0 cm
3rd detector	0.5 cm	6.5 cm	12.5 cm	24.5 cm
active area	$2.5 \times 3.5\,cm^2$	$5 \times 5\,cm^2$	$5 \times 5cm^2$	$5 \times 5\,cm^2$
high res area	$1 \times 3.5\,cm^2$	$2 \times 5\,cm^2$	$2 \times 5\,cm^2$	$2 \times 5\,cm^2$
strip pitch	25.50 μm	50.10 μm	50.10 μm	50.10 μm
# of channels	688 × 3	688 × 3	688 × 3	688 × 3

four frames are aligned against the two orthogonal reference surfaces of the underlying granite bench.

Each strip is read out by means of a front-end preamplifier, a remote-end amplifier and a charge integrating FLASH ADC [14, 15]; the analog signal at the amplifier output has a semigaussian shape with a base width of $\sim$ 140ns.

The overall signal-to-noise ratio, after 200 ns integration in the ADC, evaluated under real experimental conditions, is $\sim$ 19 for one minimum ionizing particle.

The analog single strip readout has been chosen to maximise the ability of the system in dealing with sequences of adjacent hits; the released charge information gives a simple estimate of the number of tracks involved and, in some cases, its pattern along the cluster permits a better determination of the track impact coordinates.

The overall detection efficiency of every plane was measured to be better than 99% including non-functional strips and/or broken electronics channels. The resolution power of the whole system can be expressed through the extrapolated transverse error to the mean interaction point in the target, which is about 7 cm upstream of the first microstrip plane; it turns out to be $\sim$ 9 μm for infinite momentum tracks crossing the high resolution regions of the twelve detectors.

3.4.2 PWC system

The multiwire proportional chamber (PWC) system for E687 consisted of 20 signal planes grouped into 5 stations with 4 planes per station. These stations were labeled P0, P1, P2, P3, and P4, upstream to downstream. Stations P0, P1 and P2 were located between the two analysis magnets with P0 just downstream of M1. P3 was located just downstream of M2 and P4 was just downstream of the last Cerenkov counter C3.

There were two types of PWC stations, Type I (P0 and P3), and Type II (P1, P2 and P4).

Each station had four views. The X view wires ran vertically and measured horisontal position. The stereo angle for the U and V views was 11.3° from the Y view. The orientation of the wires, which is the same for Type I and Type II, is shown in Fig. 22.

The Type I stations had an aperture of approximately 30 in. $\times$ 50 in. (larger dimension is vertical) with four anode views, YVUX in upstream to downstream order. The Type I anode and cathode planes consisted of copper-clad G-10 circuit boards laminated to solid G-10 frames milled for flatness. Wires were wound onto transfer frames, aligned and glued onto the frames and soldered to the circuit boards. Flexible ribbon cables were plugged into headers soldered onto the circuit boards and carried the anode signal to connectors located outside the gas volume. All cathode and anode planes in a station were stacked within a sealed aluminum gas box with Mylar windows and a removable cover plate for access. The planes were stacked onto precision machined locating pins that pass

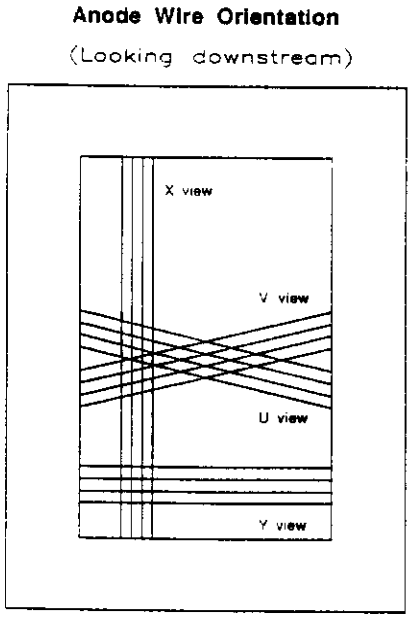

Figure 22: Orientation of PWC wires

through two locating rings at one end of each plane. The locating pins fit into holes machined in the gas box and are visible from the outside so that survey and alignment of the planes may be easily accomplished without opening the gas box.

Type I anode wires were 0.8 mil diameter gold-plated tungsten under 65 gram equivalent tension. The wire spacing was 80 mils and the anode-cathode half-gap was 0.235 in. Cathode wires were 2.5 mil diameter Cu-Be and ran vertically with a pitch approximately 0.4 times that of the anodes. Because of their length, the X plane anode wires were glued to a support wire running horizontally across the middle of the plane in order to achieve electrostatic stability.

The numbers of instrumented wires for Type I stations were 376 for X planes and 640 for Y, U and V planes giving a total of 2296 wires each for P0 and P3.

The Type II stations P1, P2 and P4 had the same basic construction, number of views, stacking order and stereo angle but had a larger aperture of approximately 60 in. × 90 in. To provide extra stiffness, Type II planes had a layer of stainless steel laminated within the frames.

The Type II anode planes used 1.0 mil gold-plated tungsten wire under 90 grams equivalent tension. The wire spacing was 120 mils and the half-gap was 0.240 in. The cathode wires were 3.5 mil Cu-Be and also ran vertically. Again, the X view anode wires had to be supported, but here Mylar garlands running horizontally across the aperture were used to constrain the anode wires in plane between the adjacent cathodes.

The numbers of instrumented wires for the Type II stations were 512 for X, 768 for Y and 832 for U and V planes, giving a total of 2,944 wires per Type II station and thus a total of 13,424 instrumented wires for the entire PWC system.

In October 1987 the original P4 station was damaged and was replaced by a

smaller chamber, $P4'$, with an aperture of approximately 40 in. $\times$ 60 in., having only three views X, V and U (same angles). The X plane had 3mm wire spacing, the U and V planes had 2mm wire spacing and the half-gap was 0.250 in. There were 336 wires instrumented in the X plane and 768 each in the U and V planes.

The gas mixture used was 65/35 Argon-Ethane and was bubbled through ethyl alcohol at 0° C before being distributed to the chamber system. Flow rates were approximately 0.5-1.0 SCFH for Type I stations and 1.0-2.0 SCFH for Type II stations, giving a complete gas exchange every 12-24 hours. A system of PhotoHelic sensors and solenoid valves at the input and output of each station was used to keep a nearly constant overpressure of 0.10-0.25 in. of water. Using this gas mixture, operating voltages of 3.30-3.50 kV for Type I planes and 3.00-3.30 kV for Type II planes produced good efficiency.

Signals from the anode wires were amplified and discriminated by preamplifiers mounted on the chambers. Low voltage power for the preamps was distributed via a system of 1/4 in. $\times$ 1 in. solid copper bus bars attached to the sides and bottom of the gas boxes. Small PC boards with edge connector sockets were mounted across the bus bars and the power connectors for the preamps plugged into these sockets.

Type I stations used 8 channel preamplifier cards with single-ended MECL II outputs, while the Type II stations used 16 channel (Nanometrics N341) preamps with complementary MECL 10K outputs. Both types of preamps were capable of detecting currents of less than 1 μA.

Discriminated signals from the preamps were sent to the counting room via 200ns to 350ns of delay cable, depending on station location, where they were received and reshaped before being sent to the LeCroy 4290 TDC system where time information was recorded for every wire using the Common Stop mode.

The TDCs were located in dedicated CAMAC crates, each containing a LeCroy 4298 TDC controller that had been modified for 7 bit (127 ns full scale) operation. All 4298s for a given station were daisy-chained together using the RS-422 databus, and the last 4298 in each of the five chains (P0-P4) was connected to a Fermilab designed TDC readout controller called a P4299[16].

The P4299s each contained a Z8002 microprocessor and 48K of memory and continuously executed a program stored in ROM that waited for readout requests from the 4298s. A readout request caused execution of a vectored interrupt routine which read all data from the 4298s in the chain and reformatted the data before storing it in RAM. After readin to the P4299s was complete, each P4299 took control of an ECL bus, sent its data to a LeCroy 1892 buffer memory, and passed control of the bus to the next P4299 in line. The last P4299 sent an end of record signal to the 1892 after the last dataword had been sent telling the Lecroy 1892 that the TDC readout was complete. The time required for a complete readout cycle was approximately 300μs to 400μs for a typical hadronic event containing 150-200 sixteen bit words of wire chamber data.

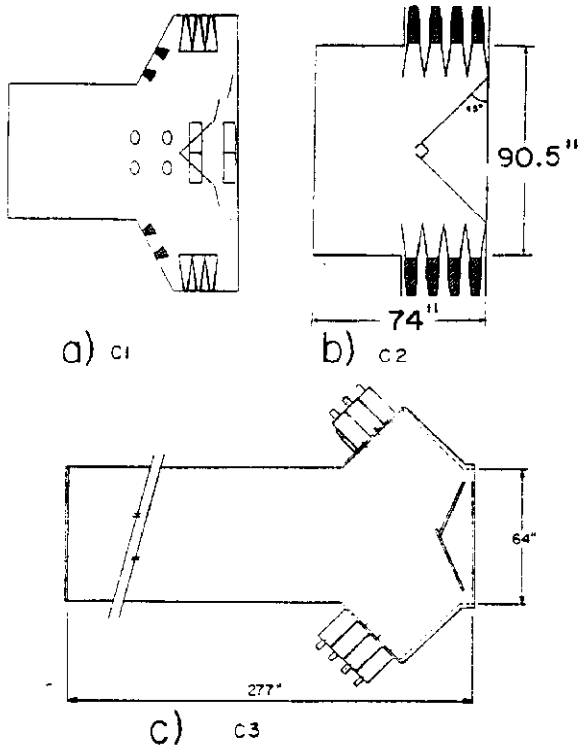

Figure 23: Plan view of the three Cerenkov Counters

Table 7: Characteristics of the Čerenkov Counters

Counter	Gas	Threshold (GeV/c)			No. of Cells
		Pion	Kaon	Proton	
C1	HeN_2	6.7	23.3	44.3	90
C2	N_2O	4.5	16.2	30.9	110
C3	He	17.0	61.0	116.2	100

3.5 Čerenkov System

There are three multicell threshold Čerenkov counters in the detector. The counters, called C1, C2, and C3, are shown in Fig. 23 and some of their characteristics are given in Table 7. The counters are all run at atmospheric pressure in the threshold mode. The gases have been chosen so that there is a wide range of momentum values in which pions, kaons, and protons can be identified. This is critical because identification of kaons and/or protons ("heavies") is crucial for the observation of many of the charm signals present in the data. In the Čerenkov system, pions are separable from heavies from the C2 pion threshold of 4.5 GeV/c to the C3 kaon threshold of 61 GeV/c. Protons can be unambiguously identified between 16 GeV/c and 44 GeV/c and between 61 and 116 GeV/c. In the region between 44 and 61 GeV/c, protons and kaons can be

distinguished from pions but cannot be differentiated from each other.

3.5.1 C1

The Čerenkov counter C1 is the most upstream of the three Čerenkov counters, lying just beyond the first analysis magnet, between the first two PWCs. The counter has a pion threshold of 6.7 GeV, between those of C2 and C3. Counter thresholds for various particles are given in Table 7. The gas used was a helium-nitrogen mixture, and the total length of the counter gas volume along the beam direction is 71 in.

The active area of the counter spans 80 in. in the magnet bend direction and 50 in. in the transverse direction. It is divided into 90 cells by a series of mirrors covering the downstream plane of the gas volume. A schematic of the counter is shown in Fig. 24(a). The mirrors are organized into two readout systems, planar and conventional. The conventional readouts use 2mm thick plastic focussing mirrors designed to focus Čerenkov light onto individual phototubes located upstream of the mirrors, just outside the fiducial volume. Each of the 40 focusing mirrors represents one cell, and all are located in the outer portions of the counter. The corresponding 40 phototubes have diameters of 3 or 5 in. The smaller ones require collection cones to ensure complete light collection. The remaining cells make up the planar mirror section, located at the center of the back plane. Two glass planar mirrors, each 14 × 32 in. , are oriented at 90 degrees with respect to each other and 45 degrees to the beam direction. Light reflecting off these is detected by 2 and 3 in phototubes, 25 on each side of the counter, oriented exactly transverse to the beam direction. Light collection cones are located in front of the phototubes, and are close-packed to ensure that no light reflected from the planar mirrors escapes detection.

The response of the counter can be described in terms of the average number of photoelectrons detected in a particular cell due to a $\beta = 1$ particle, when the Čerenkov cone is completely enclosed in the cell. Under these criteria the typical cell in the C1 planar section sees 3.6 photoelectrons while the conventional cells see about 2.5 photoelectrons.

3.5.2 C2

The cell structure of C2 is shown in Fig. 25. The counter is located downstream of C1 and is between the PWCs P1 and P2. It has an aperture of 64 in. × 94 in. and a length in the beam direction of 74 in. The counter contains 110 cells including 54 inner cells and 56 larger cells on the periphery. The inner cells detect photons with Thorn EMI 9939A 2-in. phototubes while the outer cells use RCA 8854 5-in. phototubes. The faces of the phototubes are coated with the wavelength shifter p-terphenyl. Each cell utilizes a light collection cone made of specular quality Coilzak which was realuminized and overcoated with a thin film of MgF_2.

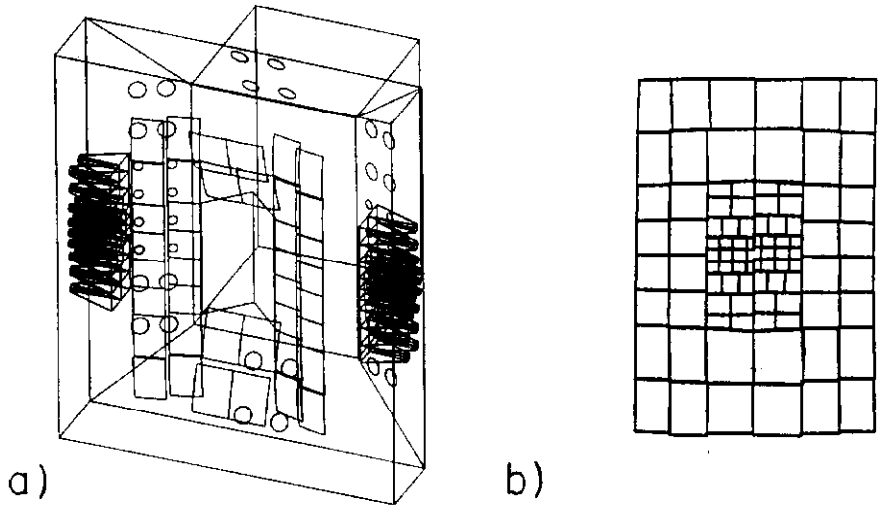

Figure 24: Cell structure of C1: a) shows the positions of the mirrors and light collection cones; b) shows how the aperture is mapped into the photomultipliers.

The counter contains two planar mirror sections. The mirrors reflect the Čerenkov photons toward the light collection cone arrays which are mounted on the side of the structure. (The cell structure shown in Fig. 25 is actually a beam's eye view of the virtual image of the light collection cone arrays.)The mirror sections are each mounted at a 45° angle relative to the beam direction forming a 90° angle between them. The mirror sections are each 44 in. × 92 in. and contain 32 separate mirrors. Each mirror consists of a glass substrate 11.0 in. × 11.5 in. × 0.0394 in. thick which is aluminized and overcoated with MgF_2 on the front surface.The mirrors have 88% reflectivity at a wavelength of 400 nm and maintain a reflectivity of greater than 80% down to 220 nm, below which practically all the light is absorbed by the radiator before reaching the phototubes. A small vertical gap between the two mirror sections in the center of the counter was designed to reduce the material in the region of high incident photon and electron-pair flux.

The gas used is N_2O at atmospheric pressure which gives a pion threshold of 4.5 GeV/c. Since no information on the scintillating properties of N_2O was available during the design of the counter, beam tests were run at Brookhaven with a small test cell. No evidence of scintillation was observed and the gas proved to work well in the experiment.

The photoelectron yield for the 2-inch cells ranged from 8 to 16 with an average value of 11 photoelectrons. For the 5-inch cells, the yield varied from 5 to 13 photoelectrons with an average value of 8 photoelectrons.

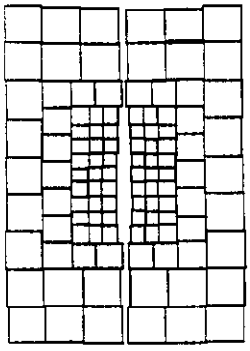

Figure 25: Cell structure of C2

3.5.3 C3

Counter C3, which has the cell structure shown in Fig. 26, was the most downstream of the three Čerenkov counters and was located downstream of the second analysing magnet between the MWPCs P3 and P4. The counter was a helium threshold counter which was 277 in. long with an aperture at the upstream end of 60 in. × 93.25 in. Its pion threshold of 17 GeV was the highest in the system.

The counter had 100 spherical glass focussing mirrors with a total projected area of 1.4 m × 2.0 m. The slumped glass mirrors were 0.060 inches thick with a radius of 260 cm (focal length of 130 cm). The mirrors were cut in three sizes: 22.4 × 30.3 cm, 22.4 × 20.3 cm, and 9.8 × 10.3 cm. (The curved blanks were produced by Glass Fab, Inc., Rochester, N.Y. 14612.) The mirrors were coated with aluminum with an overcoat of MgF_2 to optimize the reflectivity at 140 nm. Light collection cones made from 10 mil mylar coated with aluminum and MgF_2 were used with the smallest mirrors.

The Čerenkov light was detected by phototubes coated with a waveshifter (p-terphenyl) and MgF_2. Thorn-EMI 9939B (2 inch) tubes were used for the smallest mirrors; RCA 8854 (5 inch) tubes were used for the most central large mirrors; and RCA 4522 (5 inch) tubes were used for the outer large mirrors.

The tubes were separated from the helium volume by CaF_2 and quartz windows. CaF_2 was used for all central cells and quartz was used for the outer cells. (Cost considerations were the reasons for these choices.) The UV cutoff for CaF_2 is around 135 nm and the cutoff for quartz is around 180 nm. The gaps between the tube faces and the gas volume windows were flushed with N_2 in order to prevent helium from poisoning the tubes.

The photoelectron yield for all cells ranged from 3 to 17 with an average of 9. For the large mirrors, the photoelectron yield for cells with CaF_2 windows was about 30% higher than for the cells with quartz windows.

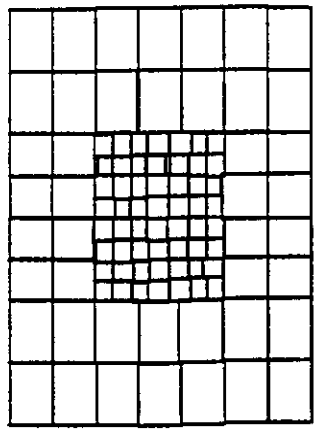

Figure 26: Cell Structure of C3

3.6 Muon System

The muon detector for E687 [17, 18] includes a section for identifying muons produced at less than 40 mr (Inner Muon) and a section for wide angle muons extending to 125 mr (Outer Muon). The small angle muon detector consists of two slabs of iron absorber with three scintillator hodoscope planes, for triggering, and four planes of proportional tubes for localizing the muon trajectory. The iron of the downstream analysis magnet is the absorber for the Outer Muon system, which includes two scintillator hodoscope planes and two proportional tube planes.

The fast muon identification for trigger purposes is provided by the scintillation counters mounted behind M2 (OMV and OMH) and those mounted behind the muon filter steel downstream of the Hadron Calorimeter (IM1V, IM1H, and IM2H).

The location of these counters is shown in Fig. 1. The configurations of these detectors, together with the muon proportional tubes, to be discussed in the next section, are shown in Fig. 27.

3.6.1 Inner Muon Scintillators

The Inner Muon Scintillators (IM) are in two sets. The first set is in two hodoscope planes (IM1H and IM1V) placed downstream of the first muon filter consisting of 121 cm of steel. This steel, and calorimeters immediately upstream, make up approximately 10 interaction lengths of material. The two planes have counters in vertical and horizontal configurations. The arrays cover 2.0 m $\times$ 3.0 m. The second set is downstream of the second muon filter which is an additional 60 cm of steel. There is only one hodoscope plane (IM2H) in the second set, and it is configured horizontally; this plane also covers 2.0 m $\times$ 3.0 m. The IM covers $\pm$ 60 mr in the bend view (y) and $\pm$ 40 mr in the non-bend

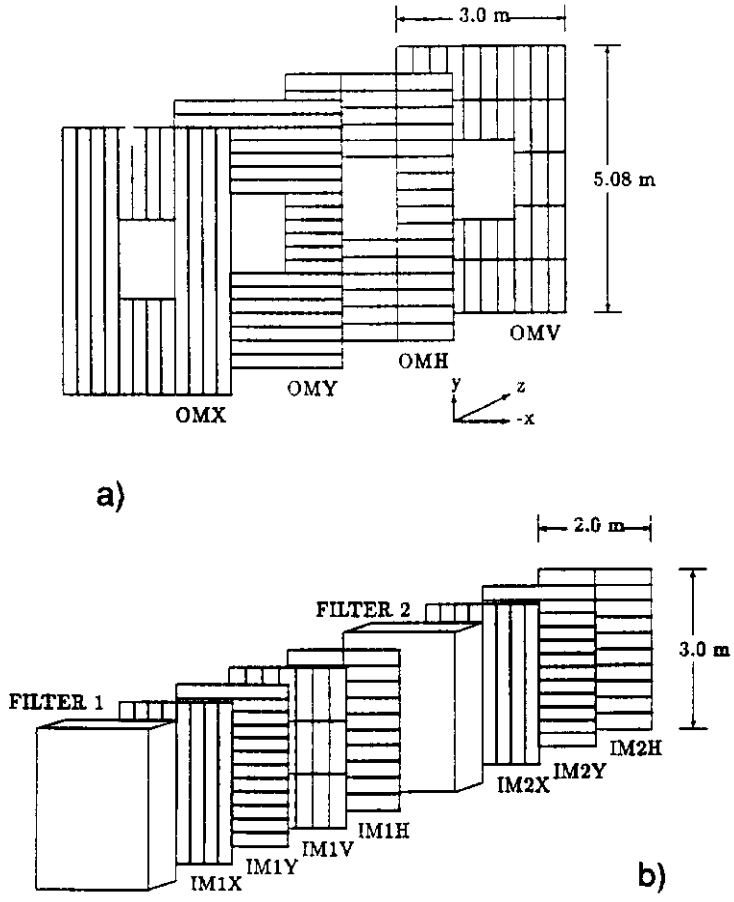

Figure 27: Muon detector configuration: a) Outer Muon Detector; b) Inner Muon Detector. The beam is in the z direction.

view (x). There are a total of 61 counters in IM.

The IM's are conventional scintillation counters utilizing Polipop n.0180, a naphthalene based scintillator, made by Polivar [19]. Each scintillator is 100 cm long 30 cm wide and 1 cm thick. The photomultipliers used were Amperex XP2232B.

The signals from these counters are processed by LeCroy 4413 discriminators and LeCroy 4418 delay units and are stored in ECL latches designed by Fermilab [20]. The latched signals are scaled and also used to form a "Muon Trigger".

3.6.2 Outer Muon Scintillators

The Outer Muon Scintillators (OM) are in vertical and horisontal arrays. The arrays have dimensions of 3.0 m × 5.0 m. The coverage of these planes is from ±50 mr to ±200 mr in the bend view and from ±35 mr to ±125 mr in the non-bend view. There are a total of 89 channels in OM. The iron yoke of the second analysis magnet, M2, provides a 10 interaction length absorber for these detectors. The OM counters are made with the same scintillator material and dimensions as the IM's but have an additional difficulty in that the counters are in a hostile environment– a magnetic field of up to 300 gauss. This problem is solved by using a high-field phototube made by Hamamatsu [21] and a special base[22].

The Hamamatsu R2107 [23] has a photocathode 7.0 cm in diameter with four multiplication dynodes in the form of closely spaced mesh layers. Due to the close spacing of the dynodes, it is relatively immune to magnetic fields. However, the charge gains of the Hamamatsu R2107 tubes, operating at 1000 volts, vary from 100 to 1900 so that the base must contain a high-gain, low-noise amplifier. Since the design of these electronics, high field phototubes with gains of up to 10^6 have become available.

The requirement of the amplifier section of the base is as follows: The minimum input is ~100 μvolts across a few hundred ohms. The amplifier output must be at least a few millivolts above the noise for the discriminator section to operate. The risetime of the signal must be ~10 ns to handle the counting rates expected in the experiment.

The intrinsic noise of the circuit is kept low by incorporating the Plessey SL560 300MHz low noise amplifier [24] in the amplifier circuit (Fig. 28). The amplifier card for the base also includes a discriminator which consists of a threshold setting network providing temperature compensation and four ECL NOR gates(10102) the first three of which are operated in the analog region and the last of which gives complementary ECL signals. The threshold is set by a 1 kΩ potentiometer which is in a remote location from the base.

Oscillation due to self-coupling was prevented through careful grouping of the grounds into a small area of the circuit board to reduce possible ground loops and through use of an internal shield to decouple the sensitive first SL560 from the rest of the circuit. The rf shielding is shown schematically in Fig. 29.

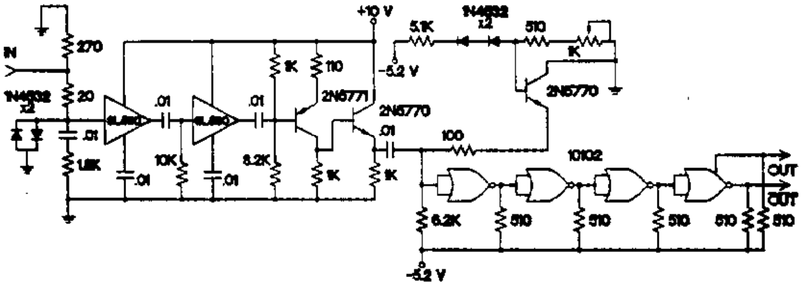

Figure 28: Outer Muon phototube amplifier-discriminator circuit

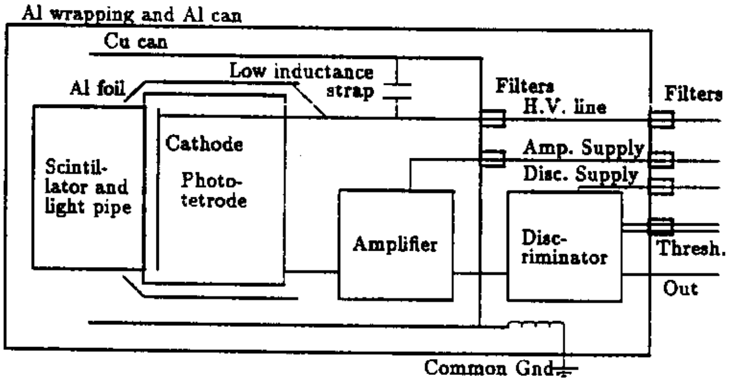

Figure 29: Outer Muon phototube electronics shielding arrangement

The ECL output from the discriminator is directly connected to the input of LeCroy 4418 delay units, and signals are stored in ECL latches built at Fermilab. These signals are also used as part of the "Muon Trigger".

3.6.3 Muon Proportional Tubes

Arrays of muon proportional tubes were placed upstream of each of the muon scintillator walls, as shown in Fig. 27. These tubes, with their finer granularity, are used in identifying muons in events with multiparticle final states. The proportional tubes are made of aluminum extrusions 5.08 cm in diameter and 0.16 cm wall thickness. A unit is made of 8 tubes attached to aluminum faceplates that act also as gas channels (Fig. 30). When the units are assembled into planes, the gas flows serially through all of the tubes in a plane. The wires, 50 μm diameter gold plated tungsten, are strung through nylon plugs with brass

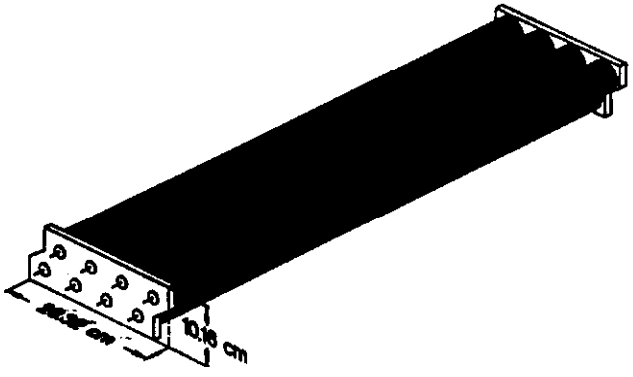

Figure 30: Muon proportional tube unit

feedthrough tubes. The nylon plugs are glued to the faceplates and the wires are soldered to the brass feedthroughs. The overlap of the tubes in a unit gives a resolution of 0.91 cm. The gas used was Ar-CO_2 (80%/20%), and the operating high voltage on the anode was -2.6 kV, 200 volts above the knee on the efficiency plateau. Each unit contains an 8 channel amplifier [25] shown in Fig. 31 , whose ECL outputs are read out by "black bin" latches, made at the University of Illinois. Proportional tube arrays of length up to 200 in. were made up.

The Inner Muon Proportional Counters (IM1X, IM1Y, IM2X and IM2Y) are in two groups to match the IM scintillation counters. Each group has two arrays reading out x and y coordinates. The total number of channels of IM proportional tubes is 320.

The Outer Muon Proportional Counters (OMX and OMY) are in two arrays which read out the x and y coordinate of the hit. There are 336 channels of OM proportional tubes. The individual channel geometry is the same as for the inner proportional tubes.

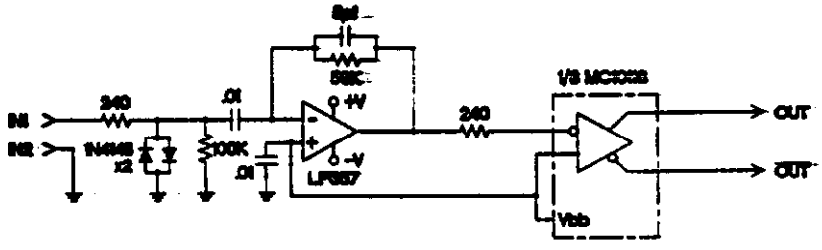

Figure 31: Muon proportional tube amplifier

3.7 Calorimetry

3.7.1 Electromagnetic (e.m.) Calorimeters

Photons and electrons are detected in the experiment by two lead-scintillator calorimeters: the "Inner Electromagnetic" or *IE* calorimeter covering the small angle region; and the "Outer Electromagnetic" or *OE* calorimeter covering the wide angle region up to about 150 mrad. The original design for these detectors provided full containment for e.m. showers and very fine longitudinal segmentation, namely 33 scintillator samplings organized in 9 longitudinal independent views for the OE, and 88 scintillator samplings in a total of 7 views for the IE. However, the original IE was totally destroyed by a fire which struck the experiment in October of 1987. All counters from the two most downstream OE sampling segments were reassembled to provide an emergency IE substitute calorimeter. This degraded the energy resolution by losing full containment for the OE and introduced a geometrical mismatch between the angular acceptance of the two calorimeters, but did provide acceptable γ and π^0 reconstruction and good electron-hadron rejection.

The OE calorimeter is located 900 cm from the target. Its external dimensions are 255 cm × 205 cm, with an internal rectangular aperture 51 cm × 88 cm. This corresponds to an angular acceptance for photons of $28 \leq |\theta_x| \leq 142$ mrad, and $49 \leq |\theta_y| \leq 114$ mrad. The OE calorimeter is mounted on a support which has a motorised drive and can be displaced both horizontally and vertically for calibration and access purposes. Counters are arranged in four independent quadrants in the x-y plane (Fig. 32). The substitute IE calorimeter (Fig. 33), with lateral dimensions 122 cm × 122 cm and an inner 10.2 cm × 10.2 cm hole, is located downstream of the M2 magnet, at 2360 cm from the target. It has an angular acceptance of $2 \leq |\theta_{x,y}| \leq 26$ mrad, both for γ and e due to the focussing optics of the magnetic spectrometer. The calorimeters are made of Pb (stiffened with 6% Sb by weight) plates and scintillator layers (POPOP $C_{24}H_{12}N_2O_2$ doped with 8% naphthalene, and NE-102 were used). Scintillator layers are made of strips, whose light readout is either individual (OE0, OE9, IEPAD segments) or five-fold integrated by a light guide to a single PMT (all other segments), as shown in Table 8. Horizontal and vertical five-fold counters are interlaced as shown in Fig. 34. In Table 8 the detailed segmentation of the OE and IE calorimeters is also shown. Each counter in the calorimeters (778 for the OE and 240 for the IE), was individually wrapped in 0.1 mm Al foils and black plastic, was light-tighted and then assembled without liners in the mechanical structure, thus reducing dead regions. Counters are equipped with ten-stage, EMI-9902KB photomultiplier tubes (PMT) operating at a typical gain of 10^6 at 1000 V, with a quantum efficiency of 20% at 440 nm. Tubes were individually tested in order to select only those with good linearity and small sensitivity to rate [26]. Gain versus high voltage was measured for all selected PMT's. PMT's are powered by LeCroy 1440 and custom-made FRAMM[27] HV

systems via a high-linearity anode-grounded voltage divider supplying 1.5 mA at 1500 V. PMT signals reach the counting room via coaxial cables, 60m long, where they are converted by Lecroy 1885 Fastbus ADCs using a dual linear range technique: this means accepting input charges up to 200 pC in the high resolution scale, and up to 1600 pC in the coarser resolution scale.

Calorimeter stability is controlled by monitoring the ADC pedestals in both ranges during and between spills, and by monitoring the HV supplies for the PMT's. Overall stability for each OE channel is checked with a N_2 laser light source, while for the IE this is done with regularly scheduled muon runs. ADC pedestals are acquired continuously in the interspills during data taking and accumulated in 1-2 hour periods. These pedestal runs are then analysed for changes with respect to the pedestal reference values, and all changes are recorded in a database for later use in data analysis. PMT voltages are periodically read back via computer, and discrepancies between setting and reading values of $\geq 0.3\%$ are stored in databases, while a warning condition is generated. The N_2 laser light is emitted at a wavelength of 330 nm. The light is converted by a 8 mm wavelength shifter bar to a frequency equal to the frequency of the light emitted by the plastic scintillator used in the calorimeter. Quartz optical fibers (OPSICA SCF, Radiall Inc. France), having a 200 μm diameter core, a 400 μm diameter silicon cladding, and a vinyl protection, distribute the light to each PMT. Each fiber is independently regulated to provide a signal corresponding to about 10 times the light emitted by one m.i.p. (minimum ionizing particle) crossing one counter. In the case of a five-fold counter, this corresponds to about 10^4 photons at the photocathode. The N_2 laser is constantly pulsed at a rate of 1 Hz. About 3-4 laser events are acquired during each interspill period. They are organized into 1-hour runs, and their statistical characteristics stored in data bases. The laser light output dependence on both the HV applied to the spark gap and on the gas pressure in the cavity was studied and optimized. An intrinsic stability for the laser output of $\pm 10\%$ was obtained. To improve this limit, two reference PMT's are used. Reference PMT's are kept at constant temperature, shielded from any beam effect and face the same fiber bundle. By using the two reference PMT's to normalize the response of the individual tubes to the laser, the intrinsic stability of the gain monitor system was improved to $\pm 5\%$. Figure 35 shows a typical laser pulse height distribution, with and without the reference PMT normalisation algorithm. Similarly, Fig. 36 shows the effect of such normalization on the average dispersion of laser light pulses as seen by 660 counters in a dedicated run. Finally, Fig. 37a) shows the response of a typical counter to the laser output during a standard 100-hour monitoring period and Fig. 37b) shows the effect of laser and pedestal correction. The monitors installed are sensitive to variations $\geq 1\%$.

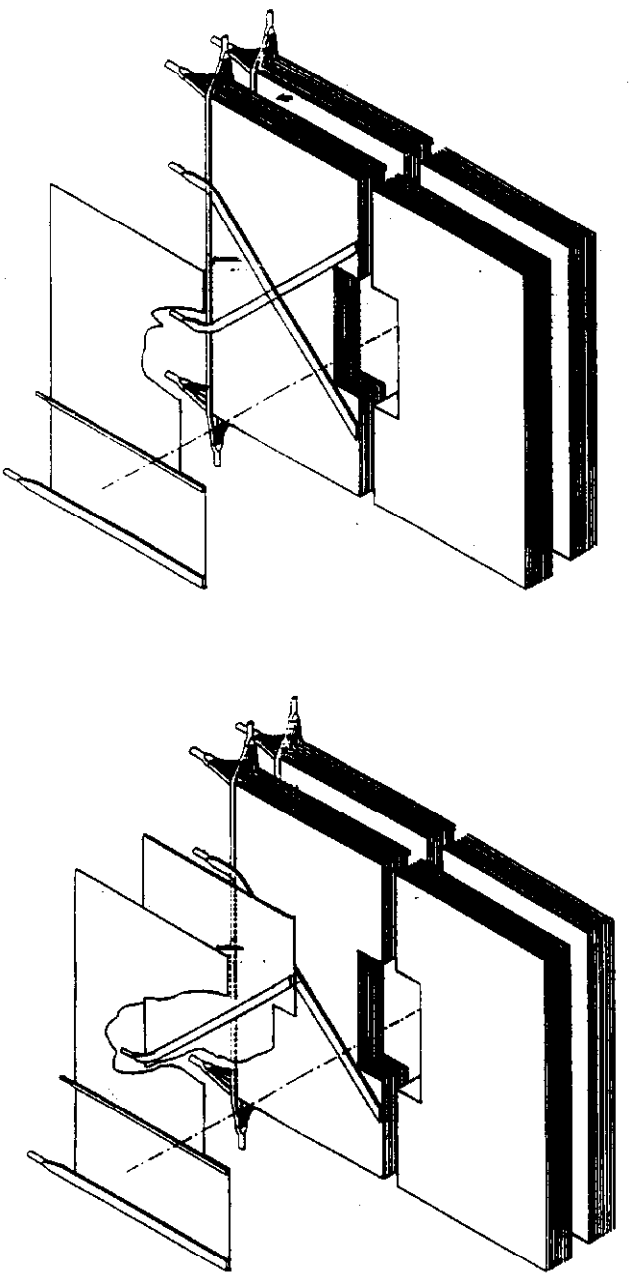

Figure 32: The Outer Electromagnetic (OE) calorimeter. A 9 cm gap along the y-axis is present to avoid e.m. showers from e^+e^- pairs from beam photon conversions.

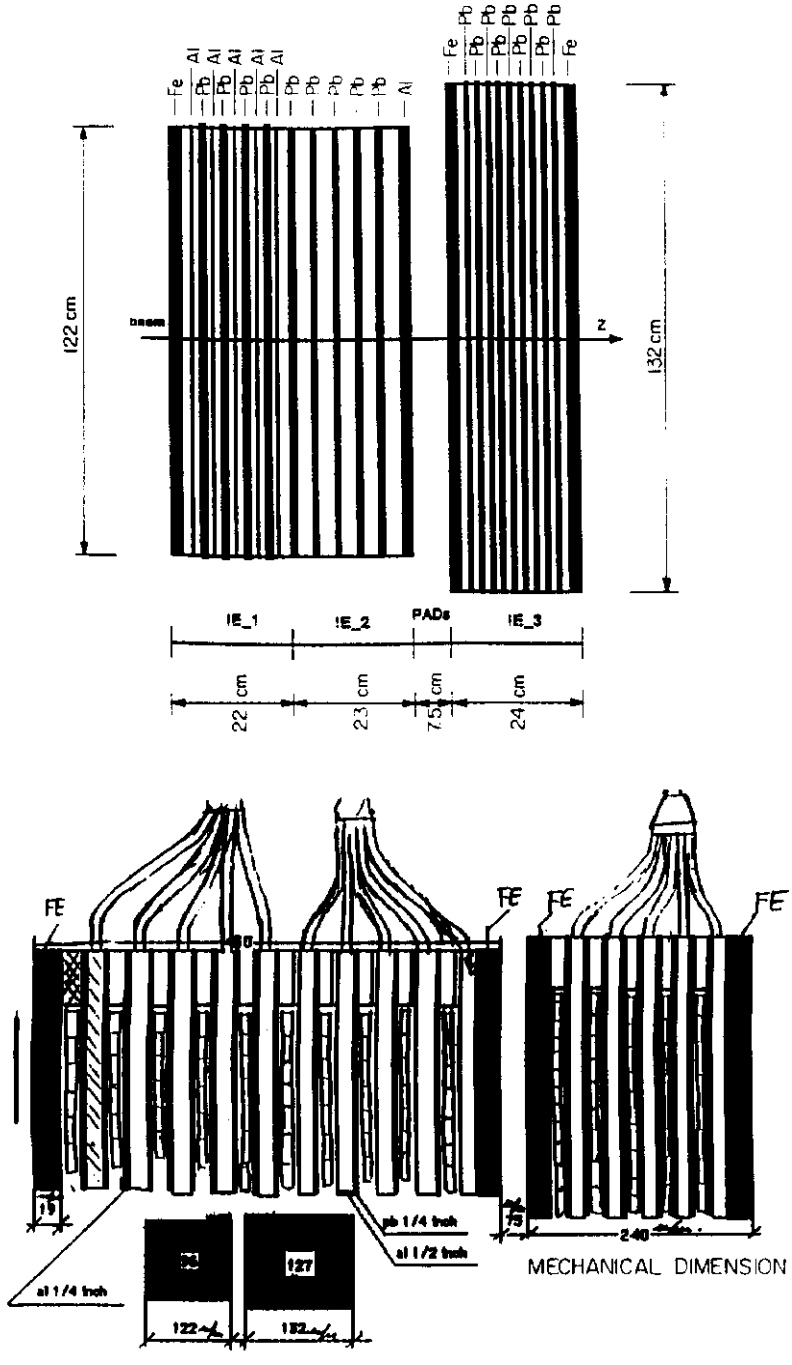

Figure 33: The Inner Electromagnetic (IE) calorimeter

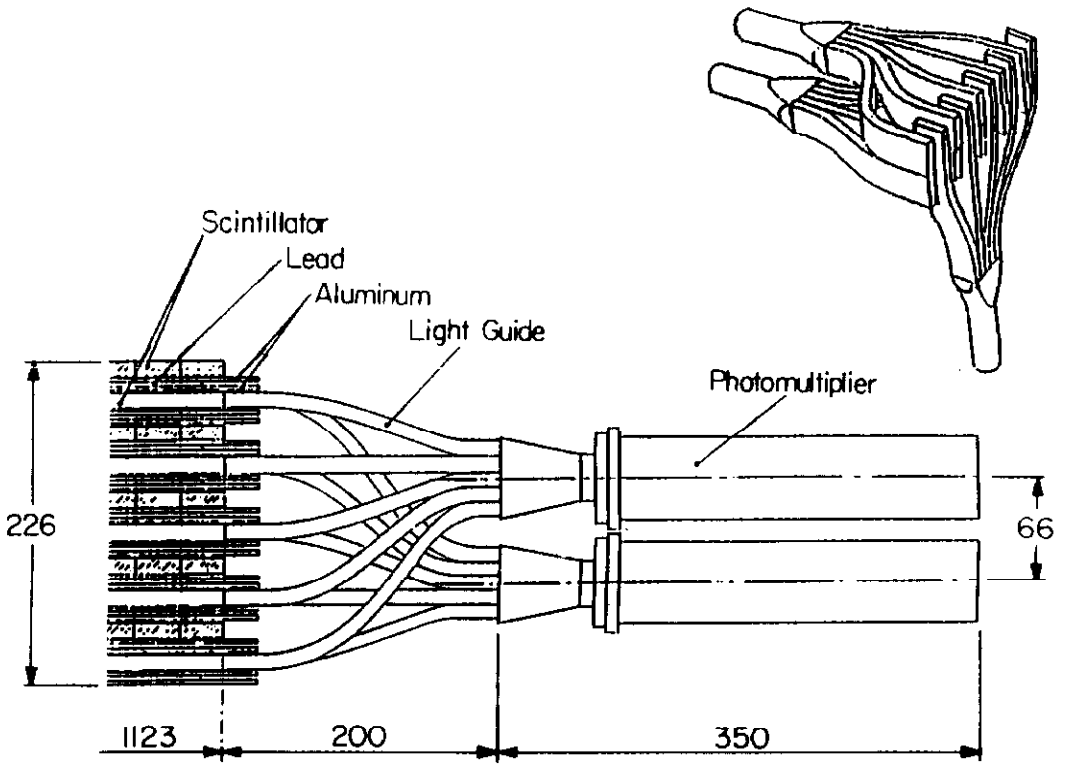

Figure 34: Arrangement of five-fold counters showing the interleaving of the Pb-Al absorbing layers and the scintillator layers. Dimensions are in mm.

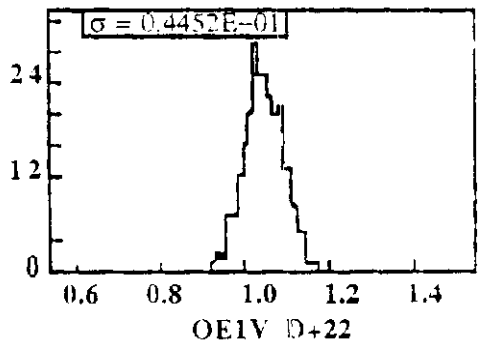

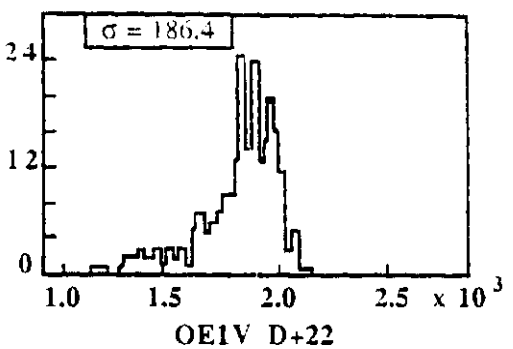

Figure 35: Typical laser pulse height distribution for one OE counter a) with reference PMT normalization and b) without reference PMT normalization, showing the reduction in variance produced by the normalization procedure

Table 8: Summary of the longitudinal and transverse segmentation of the active and passive layers of the OE and IE calorimeters

OUTER ELECTROMAGNETIC							
	OE0	OE9S	OE9Z	OE1V	OE1H	OE2V	OE2H
Rad. lengths sampled	0-1.3	1.3-1.9	1.9-2.5	2.5-7.3	3.0-7.8	7.8-12.6	8.3-13.2
Int. lengths sampled	0-0.09	0.09-0.15	0.15-0.21	0.21-0.56	0.25-0.60	0.60-0.95	0.64-1.0
Sandwich structure	AlPbAlSc			5×(AlPbAlSc)			
Pb thickness [cm]	0.650	0.254					
Al thickness [cm]	0.254						
Scint. type	NE102	POPOP					
Scint. thickness [cm]	3.0			1.0			
Counter width [cm]	3.3	7.0		3.3			
Counter horientation	hor	45^0	135^0	vert	hor	vert	hor
Counters integrated	1			5			

INNER ELECTROMAGNETIC							
	IE1V	IE1H	IE2V	IE2H	IEPADS	IE3V	IE3H
Rad. lengths sampled	0-6.21	1.18-6.35	6.35-11.1	6.38-12.1	12.1-13.4	13.4-23.7	14.6-24.9
Int. lengths sampled	0-0.43	0.14-0.46	0.46-0.72	0.47-0.73	0.73-0.82	0.82-1.35	0.87-1.39
Sandwich structure	Fe(5×ScAlScPb)	5×ScAlScPb	5×ScScPb		AlSc	Fe(5×ScPb)	5×ScPb
Fe thickness [cm]	1.9		-			1.9	
Pb thickness [cm]	0.68				-	0.68	
Al thickness [cm]	0.68		-		1.8	-	
Scint. type	POPOP						
Scint. thickness [cm]	1.0						
Counter width [cm]	3.3				25.0	3.3	
Counter horientation	vert	hor	vert	hor	square	vert	hor
Counters integrated	5				1	5	

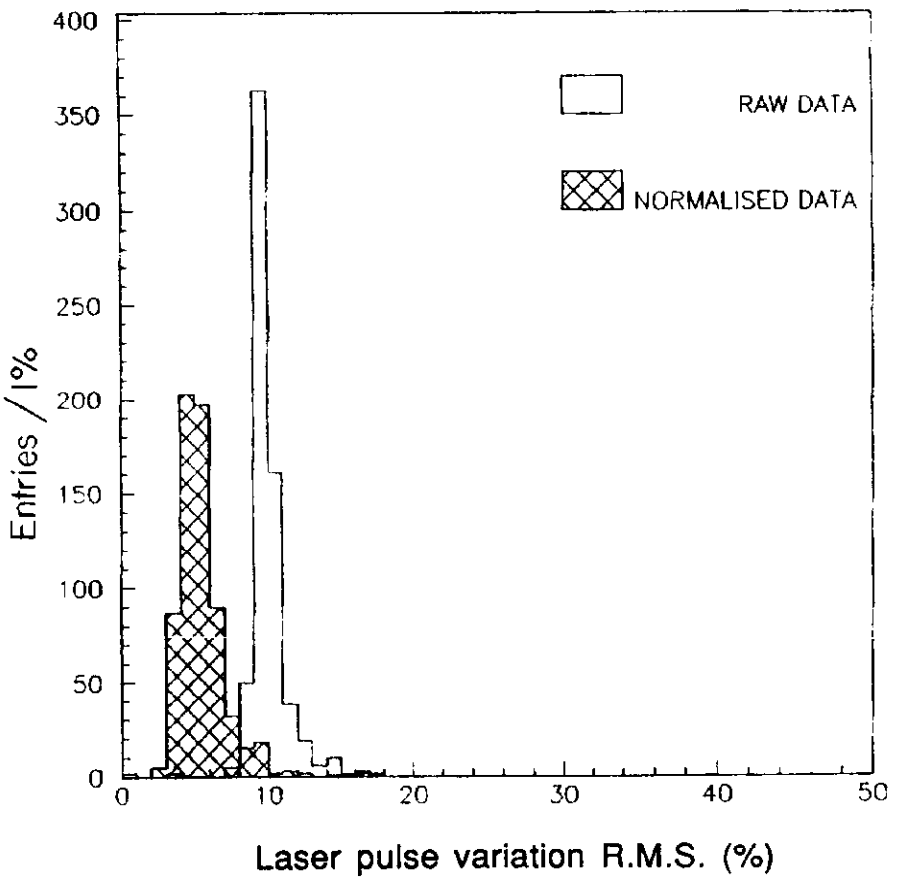

Figure 36: The distribution of the laser output pulse average variances over a 100-hour monitor period for a sample of 660 PMT's, before a) and after b) the normalisation with reference PMT's.

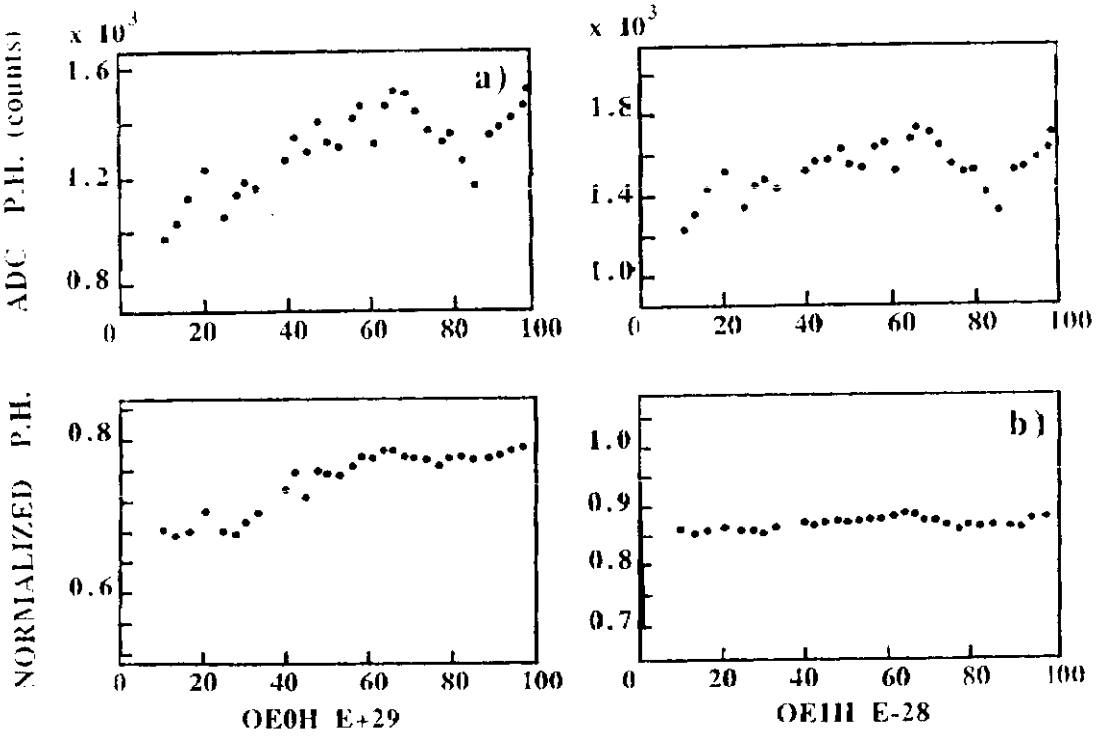

Figure 37: Time behavior of the laser output pulses: a) shows the raw data over a period of 100 hours for two OE PMT's ; b) shows the result when the output pulse has been corrected with the reference PMT normalization algorithm.

3.7.2 Hadronic Calorimetry

The main function of the hadron calorimeter for Experiment E687 is to provide a trigger which rejects purely electromagnetic events, mainly e^+e^- pairs, and enhances the selection of events with charm or beauty quarks. The hadron calorimetry covers only the inner detector. This region is covered by two separate devices: the main hadron calorimeter(HC), which covers the region from 5 mrad to approximately 30 mrad and the 'Central Hadron Calorimeter'(CHC) which covers the central 5 mrad centered directly on the beam.

The main calorimeter is an iron gas sampling calorimeter with tower readout geometry. The absorber consists of 28 iron plates with dimensions 120 in. × 82 in. × 1.75 in. These plates totaling 8 interaction lengths are separated by 1.125 in. wide gaps where the sense planes are inserted. The tower geometry of the sense planes allows formation of a trigger for the transverse energy E_t in addition to a trigger for the total energy E_{tot}. The calorimeter was made sensitive to minimum ionizing particles (mip) for monitoring and calibration. Electronic testing and monitoring was also included. Figure 38 gives an overview of this detector.

i. Construction of Sense Planes

Each sense plane consists of a multi-layered structure [28, 29] shown in Fig. 39. Particles enter the cross section from the bottom and encounter first a 0.031 in. copper coated plane of glasteel [30] which functions as a ground plane. The next layer is made up of 26 units of proportional tubes contained in PVC sleeves. These tubes, widely used in high energy physics experiments, are known as the Iarocci tubes [31]. In this construction, the inner structure of the Iarocci tubes which is normally made of PVC coated with carbon has been replaced by an aluminum extrusion channel [32] of the same dimension. The 8 anode wires of 0.002 in. diameter gold-plated tungsten are supported at the center of the 78 in. long extrusion and are terminated with a decoupling resistor of 270 Ω. The open side of the aluminum is covered with a sheet ("top") made of 500 μm polyester with a 2 μm resistive coating [33]. This resistive layer is necessary to prevent static charge from building up on the inside of the PVC sleeve. The resistivity of the "top" is between 1 and 20 MΩ/□. The layer of proportional tubes is covered with a 0.031 in. sheet of copper coated glasteel on which the pad's pattern (Fig. 40) has been engraved by a Fermilab facility. A 0.28 in. corrugated cardboard spacer reduces the capacitive coupling of the signal on the pads to ground. Six printed circuit board strips, each 12 in. wide, are placed on the top of the ground plane. Signal lines alternating with ground lines have been engraved on these strips. The signal lines are connected to the pads, through holes in the ground plane, by a short wire which is soldered to a signal line on the strip and wire-wrapped to a pin soldered to each pad. At the other end of the strip, the signal lines end in an edge card connector for coupling to the preamplifiers. Each sense plane reads out 184 pads. The entire stack is then

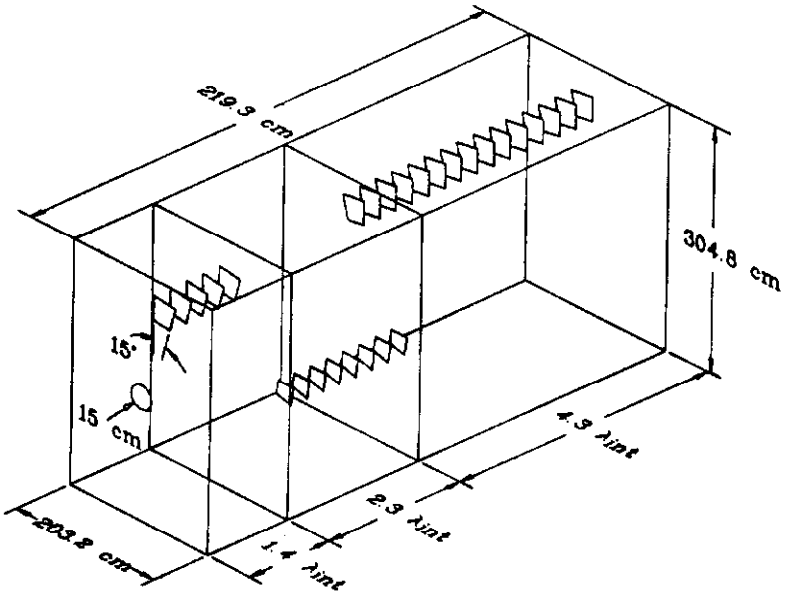

Figure 38: The hadron calorimeter, the pad geometry, and the longitudinal segmentation are shown.

covered with another ground plane. All these layers are finally glued together on a flat table under a uniform pressure [34]. Two steel bars along the long sides of the plane support each unit between the iron plates.

The sensitive area of the sense planes shown in Fig. 40 extends from an inner radius of 5.9 in. to a rectangle of 79 in. × 118 in. The subdivision into 8 concentric circles and 24 azimuthal sectors is based on the results of a Monte Carlo study of hadrons associated with charm particle decays. The design is a compromise between the size of hadronic showers, the average track separation at the calorimeter and the total number of readout channels. The pads aligned along the beam direction are electrically ganged together longitudinally in three sections to generate tower signals. This is shown schematically in Fig. 38. The choice of ganging 5, 8 and 15 sense planes is also based on a Monte Carlo study of longitudinal shower development. Most of the hadronic energy is deposited in the first 2 sections, and the downstream section measures the leakage energy of the hadronic showers. As a result, the total number of HC towers is 552.

The proportional tubes use a mixture of 50% argon and 50% ethane to which 1% ethyl alcohol was added. They are operated at 2.05 kV in the proportional mode.

A smaller calorimeter, the central hadron calorimeter (CHC), covers the solid angle left open by the hole at the center of HC. This device is considered as an additional tower to HC. The CHC is described below.

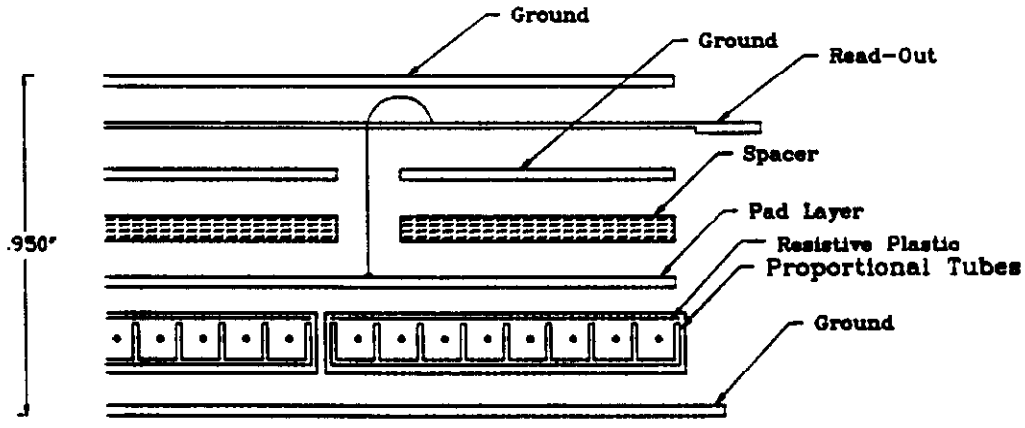

Figure 39: Cross section of proportional tube assembly.

ii. Monitoring of Gas Gain

The gas gain of the hadron calorimeter proportional wire chambers varies as a function of pressure, temperature, gas composition, and the high voltage on the sense wires. Although these conditions are monitored separately, direct methods of monitoring the gas gain with a Fe^{55} radioactive source in the same gas and with beam muons passing through the calorimeter are also employed. Radioactive source monitoring is particularly valuable for tracking short term variations in gas gain, while muons are useful for monitoring long term variations, since it is difficult to get adequate statistics over short periods.

Two cylindrical proportional counters are installed at the gas input and output manifolds to HC. These tubes measure the pulse height of the primary X-ray (5.9 keV) from the Fe^{55} sources. The pulse heights of the two are accumulated in a LeCroy qVt for one hour at a time, transferred to computer via a CAMAC interface, and analysed to find the primary peak. Figure 41 shows the variation of these peaks as a function of time. Typically the gain variations are of order $\pm 10\%$, but larger variations have also been observed. These peak values are stored in a data base and later used to correct for gain variations. As can be seen from this figure the HC response to muons and the gas gain measured from the sources track each other very well.

For the muon calibration, special runs are made with muon beams. The purpose of these runs is to establish the absolute gain of the entire calorimeter system. The gain varies from tower to tower (about $\pm 25\%$ spread) principally

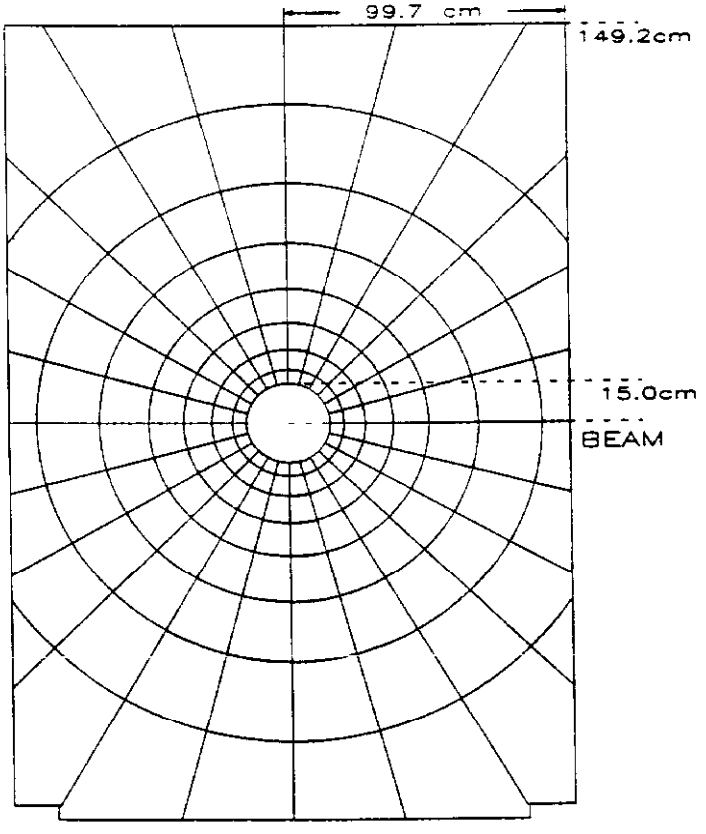

Figure 40: Diagram showing the outline of the pad geometry for the hadron calorimeter.

due to variations in the coupling of the capacitive pads and the electronic gain. The pulse height of the muon traversing one tower defines a minimum ionising particle (mip) pulse height, and all measurements in HC are calculated in terms of these mips. Typical pulse height distributions from muons are shown in Fig. 42. These distributions are fitted to find the peak value for the mip reference.

iii. Pion Calibration

The energy response and energy resolution of HC are measured with the pion beam directed at the calorimeter. Three pion momenta are used: 30, 45, and 60 GeV/c. Since the momentum spread of the pions was at least ± 15 GeV/c, this provides coverage of the momentum range from 25 GeV/c to 80 GeV/c in an almost continuous fashion. For this calibration, only pions which trigger a pair of scintillation counters centered on a designated calorimeter tower are selected. Particles which produced a large pulse height in the special downstream

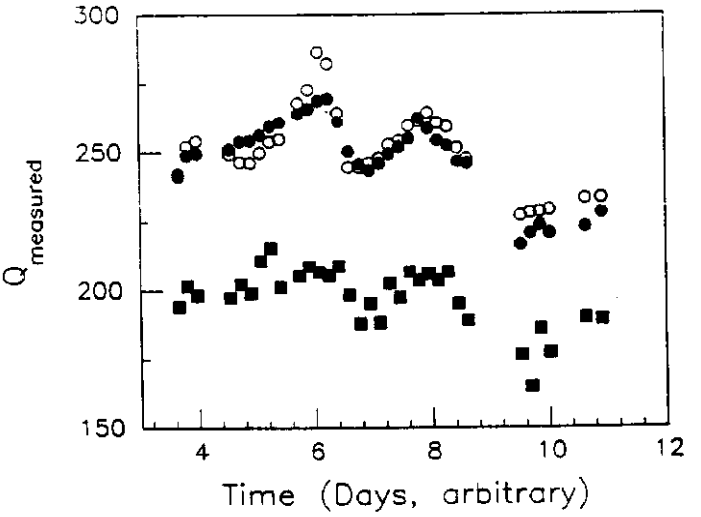

Figure 41: The variation of gas gain over an 11-day period for the hadron calorimeter measured as the collected charge ($Q_{measured}$). Black squares are for the response from muons of a specific HC tower; open circles for the gas inlet monitor, and black circles for the outlet.

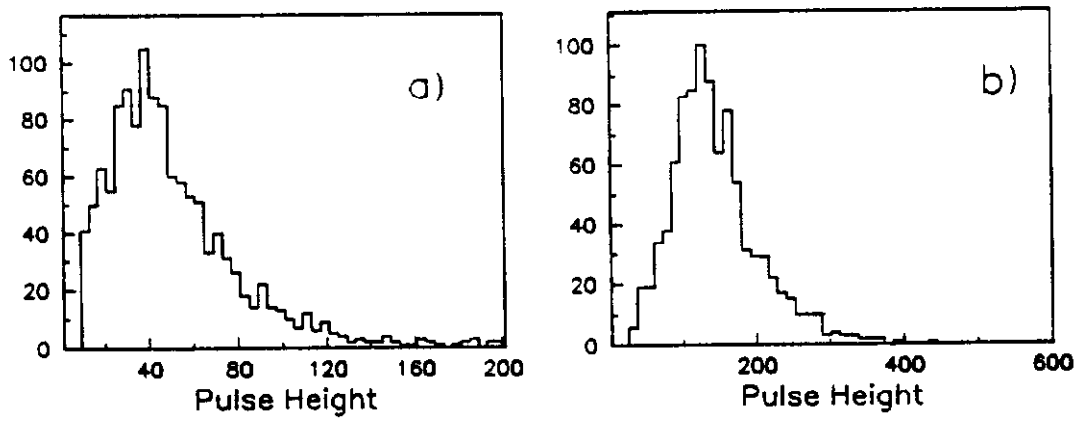

Figure 42: Typical muon pulse height spectra

scintillation counter are rejected because they could have interacted in IE upstream of HC. The sum of the pulse height in all towers of HC is computed. The data are binned into 20 bands based on the momentum measured by the spectrometer, and the range for the bands is $\pm 2\%$ of the mean momentum. The pulse height information is interpreted in terms of the mip definition given above. The pion momentum is measured in the magnetic spectrometer with an accuracy of 1.5%. Figure 43a shows the response of the calorimeter to four sample bands of energies.

This measurement is done with the pion beam pointing only at one spot of the calorimeter. (The IE calorimeter is moved aside for this calibration.) The normalization of the pulse height in each tower, as obtained with the muon beam, relates this measurement with the pion beam to the response at any point of the calorimeter. Consequently, the overall pion energy response of the hadron calorimeter is obtained by a linear fit to the energy response and is 0.601 mip/GeV (Figure 43b). To describe the energy resolution, the conventional parameterization $\frac{\sigma(E)}{E} = \frac{k}{\sqrt{E}}$, where k is a constant, is employed. The quantity k was measured to be 133% (Fig. 43c) almost independent of E. The resolution includes a 2% error due to the momentum spread within the energy bands.

iv. Preamplifier and Fan Out

The front end electronics includes a preamplifier, a pole zero filter, an amplifier, and a cable driver. The design is based on surface mount techniques with a unit of 16 channels mounted on the detector as close to the source as possible. Each tower of the two upstream sections has one preamplifier channel. Each tower of the downstream section of 15 sense planes has two preamplifiers. One serves 7 and the other 8 sense planes to decrease the capacitance seen at the preamplifier input. The preamplifier is a common base amplifier packaged

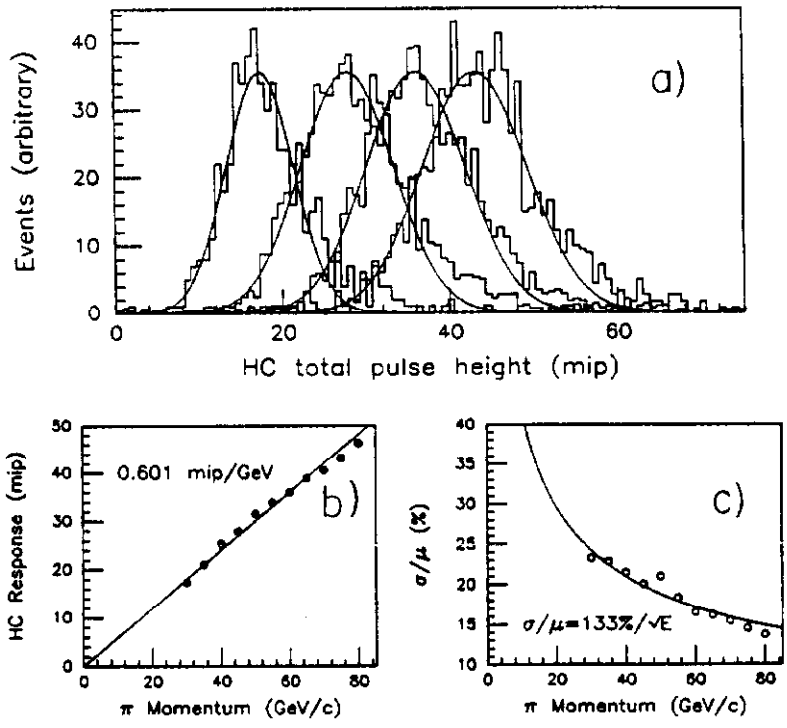

Figure 43: The hadron energy analysis of pions whose showers started in the HC: a) response of HC to pions in four different energy bands; b) average response as a function of momentum; c) energy resolution,σ, over mean energy,μ, plotted as a function of pion momentum.

with 4 channels in a single chip (Fujitsu MB43458) [35, 36]. This is followed by a pole zero filter where the values of R and C are varied to accommodate the different capacitances of the pads from about 0.01 nf to 1.0 nf. The shaped signal is then amplified by a video amplifier (NE592) followed by an emitter follower to drive 50 Ω coaxial cable 200 feet long. The signal of each tower is then split by a fanout circuit. One output goes to an ADC (LeCroy Fastbus 1880N) and is integrated for 800 ns. The other output is used for building the hadron energy trigger which includes $E_{\rm tot}$ and $E_{\rm t}$.

v. Central Hadron Calorimeter (CHC)

The Central Hadron Calorimeter is placed between the Beam Gamma Monitor (BGM) electromagnetic shower detector and the steel hadron filter just before the Inner Muon Detector (IM). It is sized to cover the forward ±5 mrad

beam hole through the Hadron Calorimeter (HC). In addition to simply measuring the hadronic energy in this beam region, its analog energy signal is included in the overall hadron calorimetry energy trigger sum. Due to a severe longitudinal space constraint between the HC and IM shielding, the CHC is a uranium-scintillator calorimeter.

The sixteen absorber layers consist of 16 in. × 16 in. × 1.5 in. depleted uranium slabs. There is an additional 1 in. transverse × 1.5 in. thick steel window frame surrounding the uranium, making a transverse profile of 18 in. × 18 in. The uranium and steel window frame is clad with $\frac{3}{32}$ in. thick steel sheets. These cladding sheets are riveted to a simple structural frame of welded 1.5 in. steel channel. An epoxy fillet completes the uranium seal. The total amount of absorber material, including scintillator in CHC, is 6.4 interaction lengths (as calculated for protons).

The sixteen 1/4 in. thick polystyrene scintillator layers are read out with conventional bent light guides and photomultiplier tubes. The first 12 layers, denoted CHC1, are read out by an Amperex 58AVP photomultiplier tube with a resistive divider base. The last 4 layers, denoted CHC2, are read out by an RCA 8575 photomultiplier tube with a transistorized base.

Typical performance for CHC1 and CHC2 for a 350 GeV, full momentum bite, incident hadron beam is shown in Fig. 44. These plots are for events chosen to have only minimum energy deposition in BGM. Correlation bands for CHC2 vs. CHC1 are observed in Fig. 45. A gain-balancing calculation minimizing the relative width of the weighted sum of CHC1 and CHC2 was performed and the resulting summed CHC distribution is given in Fig. 46. Using negative pion beams of 50, 100, 200, and 350 GeV, momentum tagged on a particle-by-particle basis, the CHC's resolution for pions not interacting in the BGM was measured to be

$$\frac{\sigma(E)}{E} = 6\% + \frac{134\%}{\sqrt{E}}. \tag{5}$$

Longitudinal shower leakage for the CHC alone decreased the CHC response by 19% for 350 GeV pions relative to the response for 50 GeV pions.

vi. Hadron Energy Trigger

The hadron energy trigger is a part of the main second level trigger for the experiment, and it selects events for which the deposited energy in HC and CHC was at least 40 GeV. The trigger electronics [29] uses the second output of the fanouts for the 552 analog outputs from the calorimeter. A set of fast analog summers adds the pulse height of all the towers at a fixed radius (Fig. 40) for each section of the calorimeter (12 modules with 24 inputs each, generating 24 outputs). Then the 24 signals are integrated for 400 ns by three integrator units (each has 8 inputs and 8 outputs) one for each of the longitudinal sections. Since the analog outputs from HC are shaped to be no longer than 800 ns, this integration time is a compromise between good energy resolution and a fast

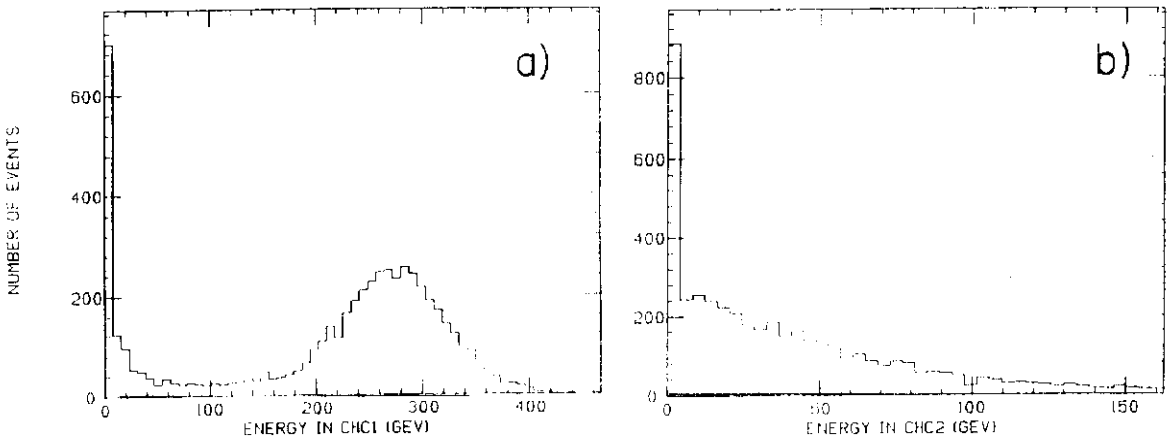

Figure 44: Energy observed in a) CHC1 and b) CHC2 for 350 pions that deposit very little energy in the BGM counter.

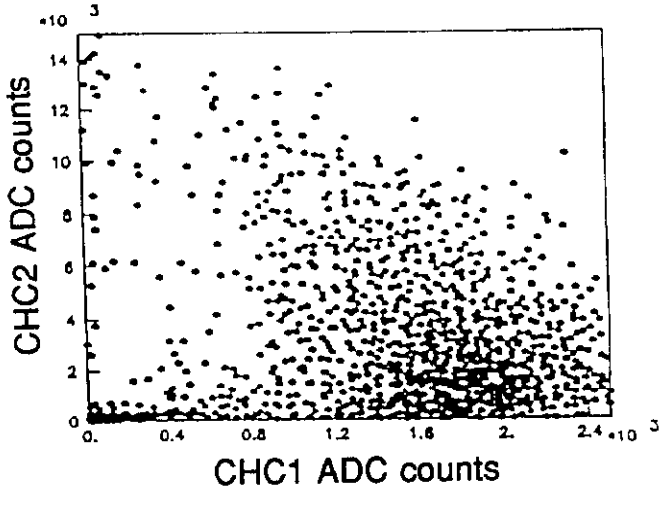

Figure 45: Plot of pulse height (ADC counts) in CHC2 versus CHC1 for 350 Gev pions, demonstrating the correlation between them.

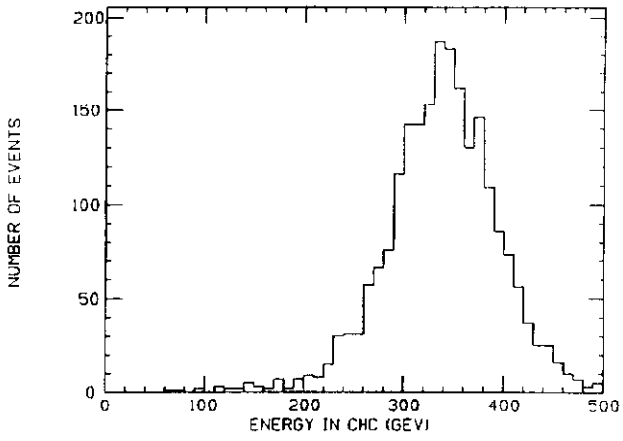

Figure 46: Plot of total energy in CHC for nominal 350 GeV/c pions not interacting in BGM.

summer modules again. The 8 outputs of the three calorimeter sections are then summed to form E_{tot}, and the outputs are weighted according to their relative radial position in the calorimeter to form the transverse energy E_{t}. The E_{t} information was not used as a trigger during the 1987–1988 running period. The final summed E_{tot} signal is digitised by a LeCroy 4504 4-bit Flash ADC. The digitised signals are added by a LeCroy 4508 Programmable Logic Unit (PLU) which sets the threshold level. The two digitised outputs of CHC from a Flash ADC are also added by the PLU to obtain the final total hadronic energy E_{tot}. This information is available for the second level trigger at 600 ns after the master gate. Figure 47 gives a schematic view of the hadronic energy trigger logic.

The choice of the E_{tot} threshold at 40 GeV for the E687 photoproduction experiment was made by considering the two curves in Fig. 48. One shows how frequently the E_{tot} trigger is set by noise from the calorimeter and electronics and the other indicates the number of hadronic events depositing an energy in HC and CHC larger than the selected threshold. The noise is measured by applying the integrating gate outside the beam spill. The data for the 1987–1988 photoproduction run were taken with a threshold of 40 GeV. This setting is a compromise between a high noise rejection and a low hadronic threshold. For this setting the hadronic energy trigger reduced the first level trigger by a factor of 100.

The trigger efficiency as a function of hadronic energy has been measured with hadronic events collected during a regular photon run without the requirement of any second level trigger. The number of recorded events is plotted as a function of the hadronic energy measured by the magnetic spectrometer for all the charged tracks in the event that intersect an area at the upstream end of HC within its boundaries. Tracks entering the central hole are not used since the

CHC signals were not included in the energy trigger for part of the data taking. Figure 49 shows this result when the trigger threshold was set to 40 GeV during one of the data taking periods. The edge is not sharp partially because the 400 ns integrating gate is not long enough to capture the entire analog signal, but principally because the hadrons lose energy in the upstream EM calorimeter (IE) which is not seen by the online trigger electronics. The efficiency shown in Fig. 49 can be fitted with a function of the form

$$\epsilon(E) = \begin{cases} 1 - \exp\left((a - E)/b\right), & \text{if } E \geq E_b; \\ c_1 + c_2 E + c_3 E^2, & \text{otherwise.} \end{cases}$$

The curve shown in Figure 49 has parameters $E_b = 17.0$, $a = 6.22$, $b = 34.2$, $c_1 = 0.059$, $c_2 = -0.0083$, and $c_3 = 0.00122$. The non-zero efficiency at low energy is due to neutral particles which deposit energy but are not seen as tracks, misidentification of electrons, electronic noise in the trigger circuit, and tracks passing through the central hole which still manage to shower partially in HC. The actual efficiency does not reach 100% even for high energy because of the loss of energy within IE which is not part of the trigger sum. The smearing of the threshold is due to HC resolution and the trigger electronics noise.

3.8 Triggering

The trigger is organized into two levels. The first level trigger– or MASTER GATE– is a simple interaction trigger. It requires a coincidence of the trigger counters TR1 and TR2, each set to respond efficiently to one minimum ionizing particle. It further requires evidence of at least two charged particles in the spectrometer. This can occur in either of two ways: two or more particles in the inner part of the spectrometer as signified by at least two sets of hits in the HxV hodoscope, a so-called 'inner-inner' trigger; or only one track in the inner detector, signified by only one set of hits in the HxV hodoscope and at least one hit in the OH array, as so-called 'inner-outer' trigger. As explained above, the geometric arrangement of these counters makes them highly efficient for hadronic events but only 5% to 10% efficient on electromagnetic events. In addition to the above requirements, veto conditions using the counters described above may be inserted into the first level trigger. The processing of a first level trigger candidate results in a negligibly small deadtime. When the conditions for a first level trigger are satisfied, gates are sent to the various readout systems. This causes all the signals that are employed in the second level trigger to be latched.

The second level trigger requires about 1.2 μs to process information latched by the Master Gate and to decide whether to read out the event or to execute a clear cycle.

The second level trigger operates on signals which are latched and pulse heights which are integrated and stored when a Master Gate occurs. These signals are processed by the level two trigger electronics– a system of specially

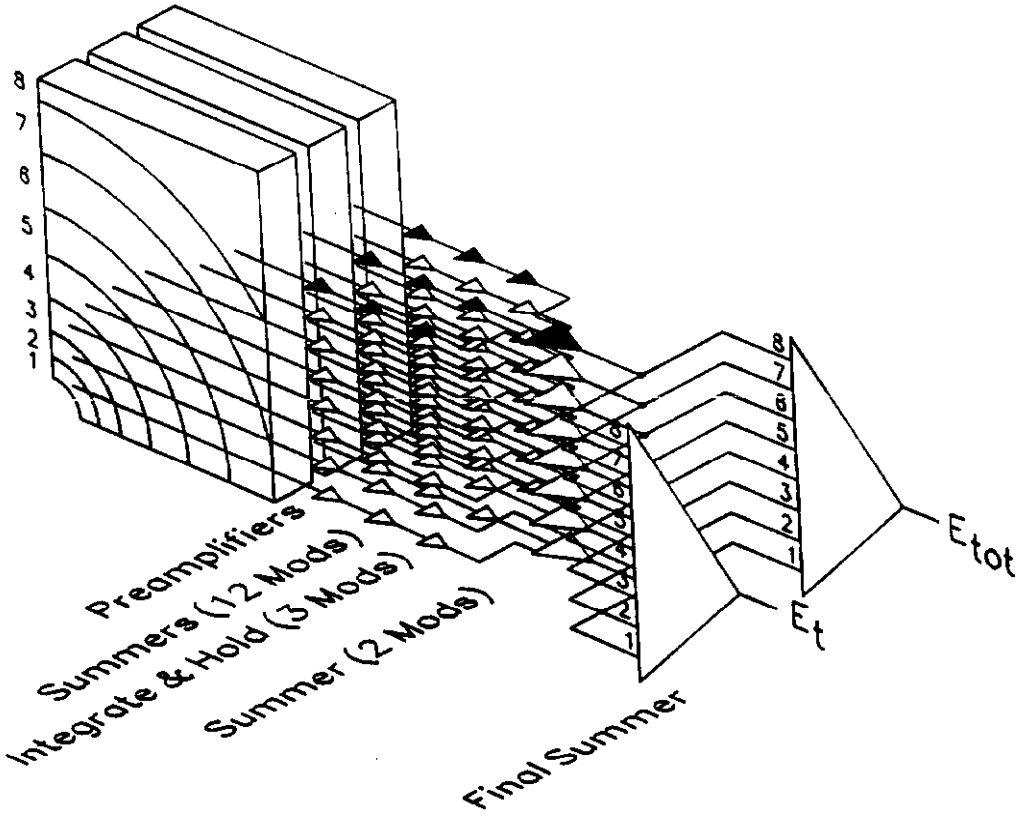

Figure 47: Schematic view of the energy trigger logic.

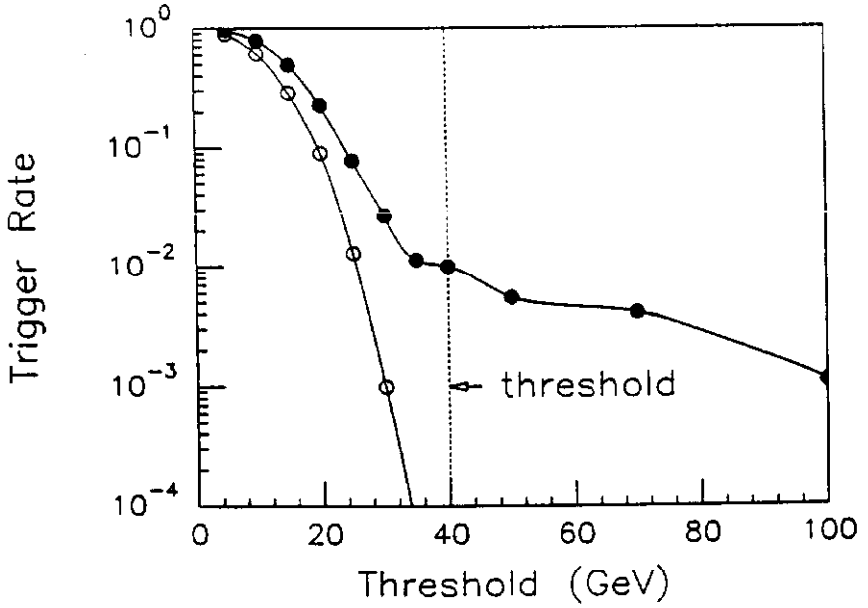

Figure 48: The hadron energy trigger rate relative to the first level trigger is shown as a function of the energy threshold. The curve associated with black circles is for photoproduction with a Be target; the curve with open circles is for noise only without an interacting photon beam.

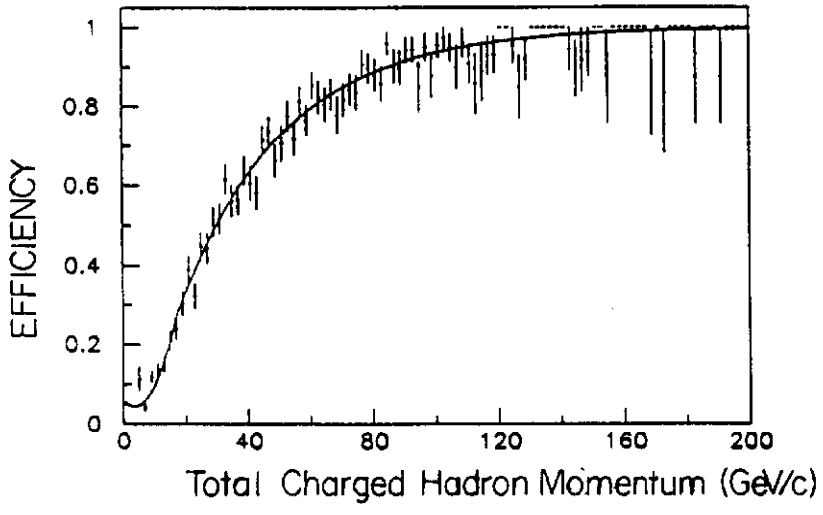

Figure 49: Online trigger efficiency versus the total momenta of the charged hadrons hitting the hadron calorimeter. The energy lost by the hadrons in the electromagnetic calorimeter is not included in the trigger electronics.

designed combinatoric logic [37] analog summation circuitry[38], and Lecroy 4415 and 44xy MLU/PLU's and Flash ADC's. This logic makes partial triggers which are called 'buslines'. The system has provision for up to 32 buslines.

The busline signals are presented to an auxiliary backplane of the trigger generator crate. This is a CAMAC crate which has special programmable trigger selection modules[39], called pin logic modules. Each module occupies one slot and is capable of producing one trigger. The module can be programmed with conventional CAMAC commands to require any of the 32 buslines to be true or false. The state of any busline may also be ignored. Finally, each module has a CAMAC settable adjustable pre-scale.

The OR of all the trigger modules constitutes the second level trigger. If within a fixed level 2 processing time of 1.2 μs, the trigger is not satisfied, a clear cycle is initiated. The clear cycle takes about 1 μs. The deadtime generated for each master gate which fails to produce a second level trigger is about 2.2 μs. If the second level trigger is satisfied, then a full readout (and automatic clear) cycle is initiated.

3.9 Data Acquisition

3.9.1 DAQ Readout, Logging and Event Distribution

The DAQ readout and logging software was written in a mixture of FORTRAN and MACRO assembly language on a PDP 11/45 running under the RT11 single user system. The RT-MULTI program[40] was used as the control interface to an interrupt driven set of routines which acquired data from the front end buffer memories, constructed complete event records, logged them to 9-track tape and distributed a subsample of events to VAX computers for monitoring tasks. These routines also acquired spill by spill data from CAMAC and logged this to the same 9-track tape.

Data comprising an event were stored during the spill in five Fastbus memory modules. Four of these were Lecroy 1892's with 4 Mbyte capacity and the fifth was a 2 Mbyte University of Illinois memory. Each memory was filled by a separate front end subsystem so that the data from each event were distributed over each of the five memories. These memories were read into the PDP extended memory via a UPI[41] interface module.

The PDP was connected to a BISON BOX[42] which was used to generate interrupts in response to the beginning and end of the accelerator spills and event triggers. It was also used to provide a means by which the PDP could add its own hold-off to the experiment busy generation: i.e. to stop and start the DAQ and to delay the start of a new spill if the readout of the previous spill was not completed.

Logging to 9-track tape was done through a STC 1921 controller connected to two AVIV tape drives. Two drives were used so that logging could continue on one while the second was being rewound and reloaded.

A Jorway 411 controller was used to provide access to CAMAC so that scaler and hardware status information could be acquired at the beginning and end of each accelerator spill.

The PDP was connected to a VAX 11/780 by both an RS232 link and a DR11W link. The former was used to pass user control and status information between the two machines and the latter was used to send a sample of events to the VAXONLINE package[43] which was used to supply events to various monitoring and display programs.

3.9.2 Program Structure

The PDP data storage memory was organized into a number of buffers, pointers to which were moved around among various queues depending on the status of the buffer: empty or partially empty; requiring processing; ready to be logged; or available for distribution to the VAX. The main event acquisition part of the program consisted of four almost independent loops each of which had an associated queue of input buffers. The first loop read events from the Fastbus memories into an empty or partially full buffer. The read was performed in

two steps. First the size and location of each subevent in the fastbus memories was determined; the second step started a DMA transfer of the data from each memory into a buffer. This buffer would then be passed to the input queue for the second loop. The first loop once started would continue until the memories were completely read out. In the second loop, bookkeeping information was added to the events just acquired from Fastbus. This uniquely identified each event and provided information needed to unpack the various subevents. The processed buffers would then be either passed back to the first loop if still partially empty or sent to the tape logging queue if full. The third loop was the tape logging loop. Buffers were asynchronously written to tape and then either put into the empty buffer queue or made available for distribution to the VAX. In the fourth loop a small fraction of the buffers were sent across the DR11W link to the VAX. On completion of the transfer the buffers were returned to the empty buffer queue or, rarely, made available to the top level RT-MULTI program for analysis.

Finally, three sections of code were required to handle spill interrupts and establish the "DAQ busy" hold off of the front end electronics. The first interrupt occurred at the beginning of the spill. After the arrival of this interrupt and after completing the readout for the previous spill, the Fastbus memories would be enabled for data taking, hold-offs would be cleared and some hardware status information would be read into an empty buffer via CAMAC. The second interrupt occurred at the end of the spill and caused the Fastbus memories to be disabled and a DAQ hold-off to be established. The last interrupt occurred a few seconds after the end of the spill and triggered the readout of both hardware status information and scaler information accrued during the spill. Again, these data were read through CAMAC into an empty buffer which was immediately made available for logging. These three interrupts were also used to synchronize certain user control commands such as "Begin Run" and "End Run" with the spill structure.

The speed of this program was the limiting factor in the total event rate available to the experiment: a little over 3,000 3 kbyte events in a one minute spill cycle. However, it was fairly closely matched to the logging capacity of a 9 track tape and the maximum throughput capacity of the UPI link.

4 Reconstruction of Data and Simulations

4.1 Tracking

There are four main categories of tracks found in the E687 analysis. Tracks which hit P0 and pass through the downstream magnet M2 are called '5-chamber' tracks. (A small subgroup of these with hits in P3 but not in the most downstream wire chamber, P4, are called '4-chamber' tracks.) The second major category, called 'stubs' or '3-chamber' tracks, includes tracks with hits only in P0, P1, and P2. Stubs are mainly low-momentum or wide-angle particles which strike the upstream face or pole tips of M2. A few stubs also result when the track-finding program fails to associate the P3 and P4 hits with the hits upstream of M2. The third major category, called 'unlinked SSD tracks', includes low-momentum and/or wide-angle tracks which did not even pass thru the upstream magnet M1. Finally, there are tracks from decays downstream of the first wire chamber which do not have hits in P0. These include tracks from 'reconstruction vees' (neutral vees decaying into two charged tracks between P0 and P2), 'P34 vees' (neutral vees decaying between P2 and P3), and 'kinks', track segments which join with other track segments but with a finite angle between the segments. The reconstruction of SSD tracks, 5-chamber tracks and stubs will be discussed in this section. The description of vees and kinks is discussed separately.

4.1.1 Microstrip Reconstruction

In order to speed up the reconstruction code, the microstrip tracking algorithm is based on projection finding on the three separate views. The efficiency of this approach depends critically on the degree of parallelism among the different planes of the same view. As previously indicated, the microstrip granite support ensures a maximum angular error of $\sim 3 \times 10^{-4}/5 = .6 \times 10^{-4}$ rad. This gives a negligible position error as compared to the intrinsic resolution of the microstrip detector.

A preliminary phase to the reconstruction, a very conservative analysis of the valid hits is performed on the basis of the released charge. This is to reduce the dimension of clusters of adjacent hits when they are consistent with a number of crossing particles lower than the dimension of the cluster itself and, in this case, to improve the measured coordinate by charge interpolation.

Projection finding is then performed with wide cuts and requires at least three hits per view. Sharing of hits among different tracks is permitted. Actually, in this process there is a soft arbitration. Hits of the last three stations, already assigned to a track having hits on all four stations, cannot be reused for a new track with only three hits.

In the next stage, projections are formed into tracks if they match in space and have a global χ^2 value per degree of freedom (DOF), lower than 8. Space

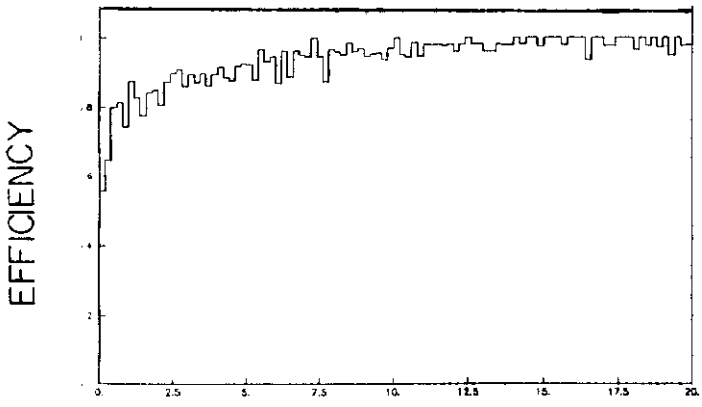

Figure 50: Microstrip reconstruction efficiency vs. track momentum

tracks sharing one or two projections are then arbitrated on the basis of their χ^2 values. This process is performed in a fully symmetric way with respect to the i and j views, selecting only the best j and k association for each i projection and, again, only the best i and k association for each j one. At this point, the class of hits not associated with any reconstructed space track is used to search for wide angle tracks and for single segments of highly multiple Coulomb scattered tracks. This search is performed by a direct match of hits in space and a track must have at least six hits.

The very conservative arbitrations employed in the algorithm often generate clusters of very closely spaced tracks, which are then eliminated and reduced to single equivalent tracks on the basis of the number of shared hits and their degrees of freedom. This reduction process, performed once at the end of the reconstruction, is cumbersome since all redundancies have to be taken into account, but it is practically unbiased by the particular track ordering.

The reconstruction efficiency of this tracking algorithm was evaluated by a full Monte Carlo simulation of the microstrip system, including hot strips and dead strips. It is found to depend on the number of DOF of the tracks, giving an overall track reconstruction efficiency of 96% for simulated photoproduced $D\overline{D}$ events, including MCS effects. The relative percentage of reconstructed spurious tracks is $\sim$ 2.7 %. Figure 50 shows the reconstruction efficiency as a function of track momentum. As shown, the efficiency approaches an asymptotic value larger than 99% at 10 GeV/c, retaining a value of about 90% at 2.5 GeV/c.

4.1.2 PWC

The multiwire proportional chamber(PWC) tracking algorithm is used to reconstruct tracks with hits in 3,4, or 5 chambers. In each case a track is required to have hits in the first chamber, P0. The algorithm proceeds as follows. Initially projections are formed from hits in all four views. In the U, V, and Y (bend)

views, projections are made using information from the PWC alone. In the X (non-bend)view, hits are first formed from a "seed" from the SSD by searching for PWC hits which match the SSD track extensions. Tracks are formed by matching all four projections. After all tracks containing an SSD-extended projection are found, then X-projections are constructed solely from the PWC hits which have not been used already. These X-projections are then matched with unused U, V, and Y projections to form additional tracks.

A least squares fit is performed on all candidate tracks. The fit parameters are the intercepts and slopes of the track in both the X and Y views at the M2 bend plane, and, in the case of 5-chamber tracks, the change in slope in the Y view (bend angle) between the track segments upstream and downstream of M2. A χ^2 per DOF cut is applied to each track to pass the fit. Tracks were not permitted to have more than 4 missing hits among all the chambers, nor more than 2 missing hits in any one chamber.

In practice, the reconstruction of tracks is somewhat more complicated than the above description suggests. First, arbitration between tracks with shared projections has to be performed. Also, there are various magnetic corrections. The finite length of M2 means that the sudden bend approximation implied by the above parameterization requires a correction. The existence of so-called off-field components B_y, B_z in addition to the main component B_x of the M2 field, the existence of a fringe field of M1 downstream of P0, and the fact that M2's field extends past P2 and P3, all lead to magnetic corrections. Finally, there is the fact that the components of B are not constants but functions of x, y, and z. All these effects are treated as higher-order corrections to the linear least squares fits described above. Each complete track fit thus has to include several iterations, so that momentum-dependent magnetic corrections can be made after the first-order track momentum is determined by the initial fit.

Ancillary to the main routine are several additional tracking routines designed to recover track topologies that are missed. These include linked and unlinked SSD tracks with hits in P0 and P1 only, and 3-chamber extensions into P3 and P4. The principal loss of tracks is due to low momentum tracks which pass through M1 and exit the PWC system before they pass through at least 3 chambers. A microstrip extension algorithm is used to recover these tracks. This routine uses SSD track parameters to predict the position of the track in P0 and P1. Hits are checked for a match and selected if the deviation from the predicted extension is less than 2 wires. The new track composed of SSD hits and PWC hits is then least squares fit and its PWC track parameters are determined.

The efficiency of the PWC algorithm was studied using Monte Carlo generated tracks(the individual chamber plane efficiencies are simulated). The efficiency was determined to be greater than 98% for tracks with a momentum exceeding 5 GeV/c. A limit of 30 charged tracks per event is imposed, not just to avoid poorer efficiency at high multiplicity, but to reduce the time for reconstructing a tape. Most of the events which appeared to have extremely

high multiplicity resulted from oscillating chambers and analyzing them fully significantly slowed the reconstruction speed. Finally, spurious reconstructed tracks occurred at the 0.5% level with this algorithm.

4.1.3 Tracing Particles Through the Magnetic Fields

Describing the trajectory of a particle in a magnetic field is conceptually very simple. If the momentum vector of a particle at some point in space is known and the magnetic field is known at all points, one can predict the motion of the particle. A method for doing these calculations very quickly without having to resort to severe approximations of the magnetic field has been developed.

The basic problem is to propagate a particle of momentum $\vec{p}$ from the point $\vec{r_0} = (x_0, y_0, z_0)$ to the point $\vec{r} = (x, y, z)$. The momentum vector is described as a total momentum p, and slopes $\vec{r'} = \frac{d\vec{r}}{dz}$.

A straightforward application of the Lorentz force equation gives:

$$\frac{\vec{r'}}{\sqrt{1+y'^2+x'^2}} = \frac{\vec{r_0'}}{\sqrt{1+y_0'^2+x_0'^2}} + \frac{.29997}{p}\int_{z_0}^{z} \vec{r'}(z_1) \times B(\vec{z_1})dz_1 \qquad (6)$$

One can algebraically solve this equation for the momentum as a function of the initial and final slopes or for the slope as a function of p and the initial conditions.

The only problem remaining is to do the integral involving the magnetic field. Since the field is a complicated function of (x,y,z) a simple parameterization of the trajectory is used. A reasonable approximation is to use only the main field component to obtain:

$$x = x_0 + x_0'(z - z_0) \qquad (7)$$

$$y = y_0 + y_0'(z - z_0) + \frac{(1+y_0'^2)}{p}\sqrt{1+y_0'^2+x_0'^2}\int_{z_0}^{z} dz_1 \int_{z_0}^{z_1} C_{00}^{s}(z_2)dz_2 \qquad (8)$$

This formula is a simple expression proportional to $\frac{1}{p}$ where the magnetic field information is present in the form of a precomputed integral between Z_0 and Z.

In the Appendix, a power series expansion of Eq. 6 which describes the full trajectory ($\vec{r}$) as a function of s is presented. This technique also expresses the trajectory as a $\frac{1}{p}$ expansion with precomputed coefficients. This trajectory trace provides magnetic corrections for track fitting and is necessary for locating vee candidates (K_s^0 and Λ^0) decaying within the volume of M1. By keeping terms up to order p^4, the resulting track description is as accurate as finite step algorithms and much faster.

4.1.4 Linking of SSD and PWC Tracks

Linking of the PWC tracks to the SSD tracks is one of the most important problems in the data analysis. It is done to provide the momentum for tracks

recorded in the microstrip detector which then pass through M1 into the spectrometer. The use of the microstrip segment in the momentum calculation improves the track momentum resolution dramatically for some track categories. A knowledge of the momentum of the tracks is essential for a correct calculation of the vertex resolution on an event-by-event basis and is essential to achieving high resolution for the impact parameters at the target and for the z coordinates of the interaction and secondary decay vertices. In addition, the fact that some PWC tracks fail to link to a microstrip track can also be significant. For example, unlinked PWC tracks are used as candidates for vee decay products and for kink decays. The rejection of unlinked SSD tracks serves as an important background reduction tool in searching for charm decays.

Linking is accomplished by comparing the extrapolated positions of SSD tracks and PWC tracks at the center of M1. Candidate links are subjected to a global least squares fit using all the hits, both from the SSD and from the PWC. For 5-chamber PWC tracks, the bend angles in each magnet are required to be consistent. Figures 51a) and b) present the linking efficiency as a function of momentum for 3 and 5-chamber tracks respectively. These efficiencies are determined by taking all PWC tracks, projecting them to the SSD vertex, and then checking to see if they are linked. The significant reduction in efficiency at low momentum is a result of multiple scattering within the microstrips which causes tracks not to be found in the SSD. The asymptotic efficiency at this stage is found to be 91.4% for 3-chamber tracks and 97.0% for 5-chamber tracks. Monte Carlo results show that the efficiency does not plateau at 100% due to the creation of a few spurious tracks in the SSD algorithm which have a better overall χ^2 than real tracks and hence are chosen.

In order to improve the linking efficiency further, a special recovery program was written to look for missing microstrip tracks. This routine traces unlinked PWC tracks back to the target and searches for possible matching SSD hits. A 2.5% increase in efficiency is observed for 3-chamber tracks and a 1.5% increase for 5-chamber tracks. The increase is essentially independent of momentum. After the implementation of this routine the asymptotic 3-chamber linking efficiency is about 94% while the 5-chamber linking efficiency is about 98%.

4.1.5 Neutral Vees

Neutral vees, K_s^0's and Λ^0's, decay into two charged tracks which may be detected in the microstrips and/or the PWC's. When these particles decay in the vertex region, they can look a lot like charm particle decays, but they have much longer mean lifetimes and typically decay downstream of the microvertex detector. Several vee-finding algorithms are employed in the experiment because of the large number of distinct decay topologies. There are four general decay regions and categories: 'SSD vees', which decay upstream of the microvertex detector; 'MIC vees' which decay inside the microvertex detector; 'M1 vees' which decay between the microvertex detector and the first chamber (P0); and

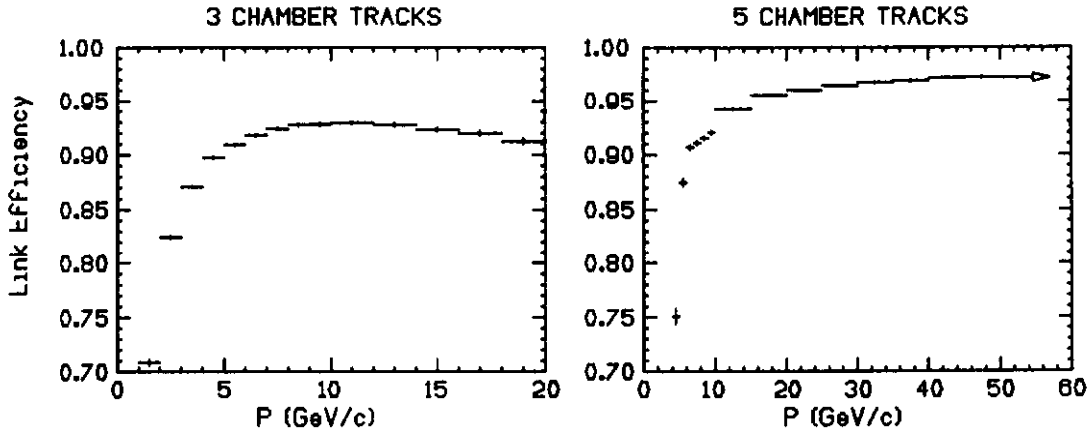

Figure 51: Linking efficiency vs momentum for a) 3-chamber tracks b) 5-chamber tracks before recovery of missing microstrip tracks.

'reconstruction vees' which decay between P0 and P2. M1 vees come in three 'flavors', depending on the number of 5 chamber tracks included in the vee. Reconstruction vees have two specific 'flavors' depending on whether the secondary vertex is upstream or downstream of P1. The overall region in which vees can be reconstructed is shown in Fig. 52. In all, vees were reconstructed over about 10 meters of decay space.

i. Target Region Vees: SSD and MIC vees

SSD vees are very straightforward to find, since they involve only looping over pairs of linked tracks with sero net charge and fitting for their vertex. To reduce the number of candidates to a reasonable level this vertex must be downstream of the primary vertex by $> 20\ \sigma_z$ and the vee track vector must point back to within 1 mm of the primary vertex in the transverse direction. The K^0_s and Λ^0 mass histograms of candidates satisfying these requirements are shown in Fig. 53. The primary benefit of the SSD information is that the track vector of the vee has resolution comparable to that of an SSD track. Figure 54 shows the x and y impact parameter distributions for vees extrapolated to the primary vertex. The impact parameters are normalised by dividing by the estimated error on an event by event basis. Typical transverse resolutions for SSD vees are about xxx times larger than those for the SSD tracks which compose the vees (10 μm).

MIC vees are neutral vees which decay within the microvertex detector in the region between the second and fourth stations. This region is 18 cm in length and contains about 10% of the observed K^0_s decays. The search for MIC vees is made possible by the very low number of spurious hits in the microvertex detector. The MIC vee algorithm takes unlinked PWC tracks and extrapolates them back into the microvertex detector. The last (fourth) microstrip station is

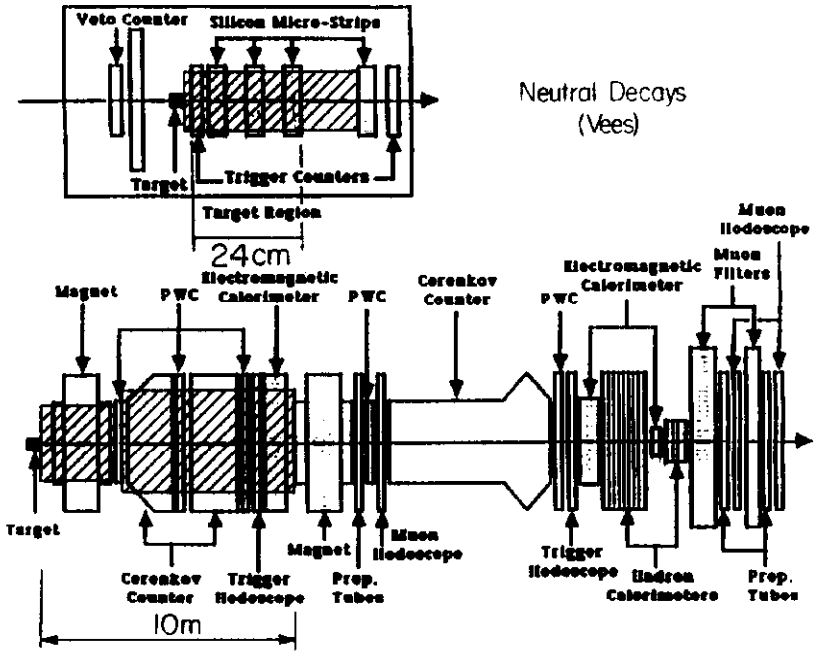

Figure 52: Regions of the spectrometer in which neutral vees can be reconstructed.

used as the "seed" station and all unused triplets in this station are tested with the candidate PWC track by comparing the residual between the extrapolated track and the triplet. If a triplet is found for a PWC track, the track parameters are recalculated and the track is projected upstream to the next station where the search for unused triplets is continued. If a new triplet is found the track is marked as a 2-station track. Since, for each candidate PWC track, more than one candidate triplet or pair of triplets may be found, arbitration among these triplets is based on the χ^2 from a global fit to all hits associated with the track. All combinations of pairs of candidate tracks with opposite charge are tested for "distance of closest approach", or DCA. The DCA cut removes almost all the spurious tracks. If a candidate track still makes more than one combination, only the one with the minimum DCA is retained. Finally the invariant mass for both the K_s^0 and Λ hypothesis is calculated and a loose mass cut applied. The K_s and Λ^0 mass plots for this category of vees is shown in Fig. 55.

ii. M1 Region Vees

The M1 region vees are formed from unlinked PWC tracks. There are three topologies: 'TT' vees, consisting of two 5-chamber tracks; 'SS' vees, consisting of two 3-chamber tracks; and 'TS' vees,consisting of one 5-chamber track and one 3-chamber track. The basic idea of the algorithm is the same for all three

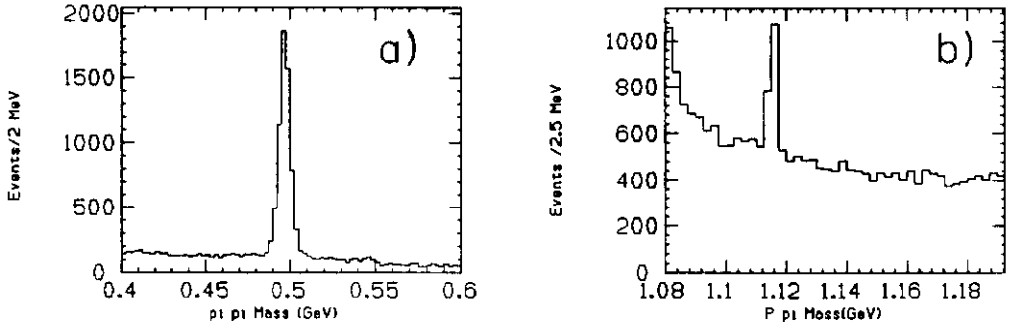

Figure 53: Invariant mass distribution for SSD vees with track mass assignments appropriate to a) K_s^0 and b) Λ^0 hypotheses. For b), the higher momentum track is assigned the proton mass.

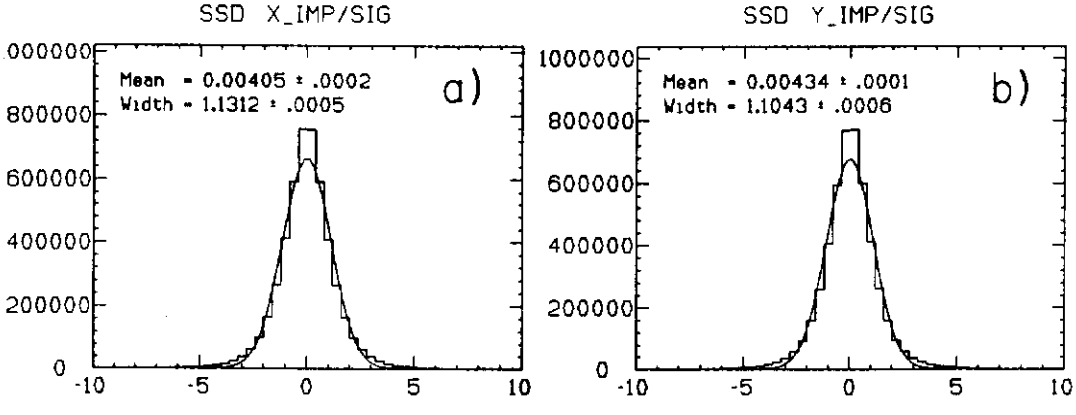

Figure 54: a) X and b) Y distributions of normalized impact parameters for SSD vees extrapolated to the primary vertex.

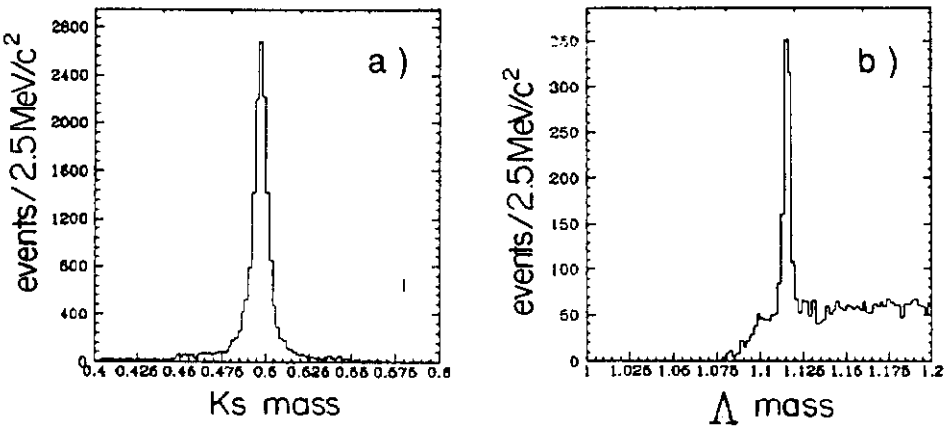

Figure 55: a) K^0_s and b) Λ^0 mass distributions for MIC vees with the appropriate mass assignments. For b) the higher momentum track is assigned the proton mass.

topologies: the X-view (non-bend) was used to obtain an estimate for the x - s location of the vee vertex and an iterative procedure based on the particle tracing formalism described previously was used to determine the y coordinate of the vertex and the momentum of all non-5-chamber tracks. The SS vees also required the additional constraint that the vee point back to the primary vertex. At this point a fit employing the full covariance matrices of the tracks, including MCS corrections, was applied to vee candidates from all three topologies. The requirement that the vee point back to the primary vertex was included in the fit via a contribution to the χ^2. The resulting χ^2 per degree of freedom was a good indicator of how well the candidate satisfied the vee hypothesis. Since the kinematics of the vee decay had an enormous effect on the mass resolution, the covariance matrix of the vee fit is used to calculate the resolution for each candidate. Mass distributions normalised to the expected resolution are used to select true K^0_s's and Λ^0's instead of the raw mass distributions. Figure 56 shows the raw and normalised K^0_s mass histograms for each of the three topologies. Fits to the normalised distributions give widths of 1.1 to 1.2, showing that the error estimates are reasonable. The Λ^0 mass histograms (with the higher momentum track assumed to be the proton) are shown for the three topologies in Fig. 57. It should be noted that all M1 vee candidates appear as entries in both Fig. 56 and 57.

iii. Reconstruction Vees

Reconstruction vees decay in the region of the spectrometer between P0 and P2. These vees are important to the analysis for two reasons. First, since higher momentum vees are more likely to decay downstream, the reconstruction vees substantially improve the acceptance at higher x_f. Second, the momentum

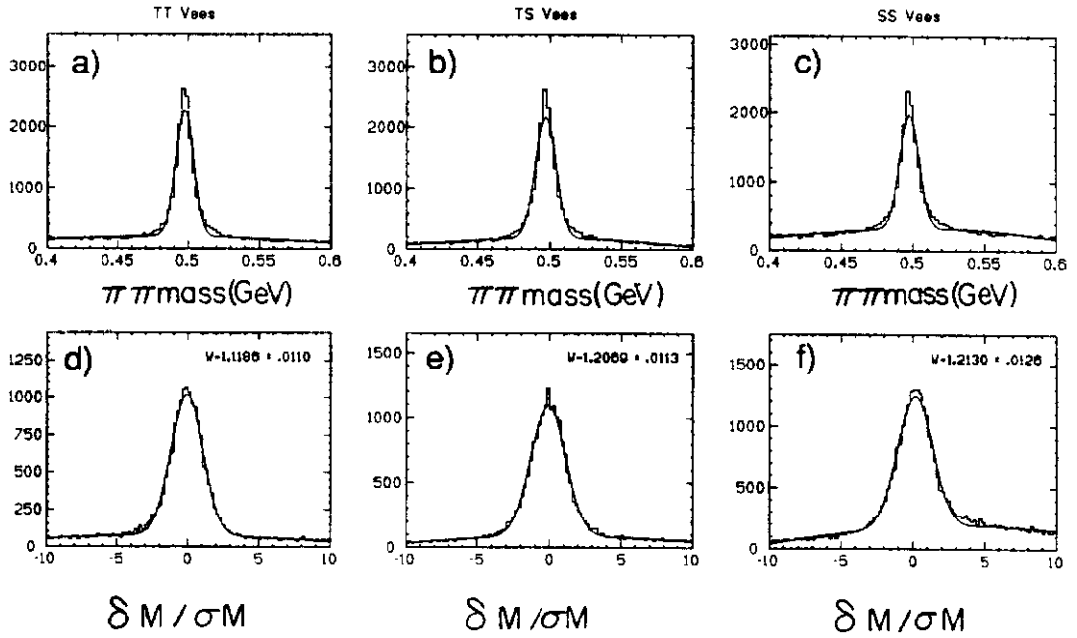

Figure 56: Unnormalized K_s^0 mass distributions for M1 region vees: a) TT vees; b) TS vees; and c) SS vees, and normalized K_s^0 mass distributions for M1 region vees: d) TT vees; e) TS vees; and f) SS vees.

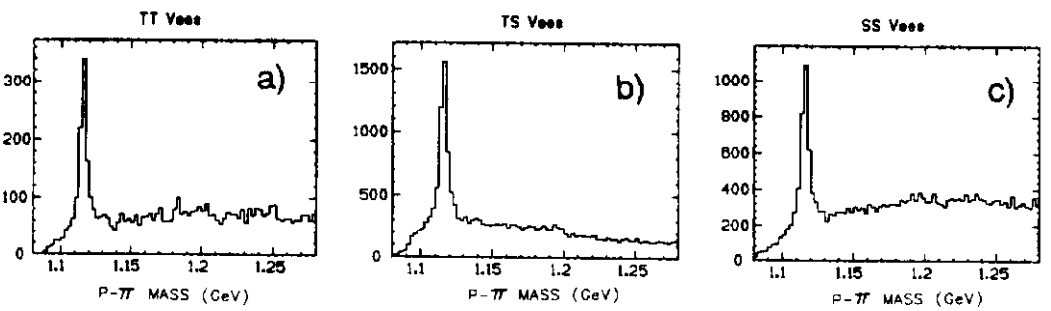

Figure 57: Λ^0 mass distributions for M1 region vees: a) TT vees; b) TS vees; and c) SS vees.

vectors of these vees are determined independent of the M1 magnetic field, so the p_t kick of M2 can be checked in a manner independent of M1 by requiring these K_s^0 decays to have the correct mass.

Since the reconstruction vee decay region is essentially field-free, no magnetic trace is required to find these vees. This fact makes the vee pattern recognition conceptually simple. However, the two tracks of the vee have less redundancy than 5-chamber tracks. For example, for a vee decaying downstream of P1, each track has at most 12 hits, as compared to 20 hits for a 5-chamber track. A more serious problem is that individual track momentum resolution for these downstream decays is poorer, because the upstream slopes are less constrained. To obtain better vee resolution and signal-to-background, the reconstruction vee fits are based on a fit to the vee as a whole, imposing the constraint that the two tracks of the vee must have a common vertex in three dimensions. Thus, the fitting procedure involves determining a total of 13 parameters: the five track parameters (x intercept x_0 and slope x', y intercept y_0 and slope y', and y bend angle $\delta y'$, just as for 5 chamber tracks) for each track, plus three parameters (x_d, y_d, z_d) for the vee decay point. The equations of constraint are:

$$y' = \frac{(y_d - y_0)}{z_d}, \quad and \tag{9}$$

$$x' = \frac{(x_d - x_0)}{z_d}. \tag{10}$$

These equations are true for each track individually, so the number of degrees of freedom in the fit is reduced by 4. An additional advantage of this method is that one obtains a χ^2 for the fit which is directly related to the probability that the neutral vee hypothesis is correct.

The reconstruction vee search proceeds as follows. The program first looks for vees decaying between P0 and P1, then for vees between P1 and P2. Each program has the same flow. Single track projections are found in the X (non-bend) view. The X hits are matched up with U, V, and Y hits to form track candidates and single track fits are performed. A loose χ^2 cut is made on the single track fits. Finally tracks of opposite charge are paired up to make vee candidates and the constrained fit described above is performed. Candidates with acceptable fits are sent to an arbitration algorithm which insures that no X-projection is used in more than one vee.

The vees which decay between P1 and P2 with decay tracks which exit before passing through P4 are handled separately. These tracks are subjected to an additional constraint that they originate at the primary interaction vertex and the transverse momenta of the tracks about this direction are required to balance.

Figure 58 presents plots of K_s^0 decays for the two reconstruction vee categories.

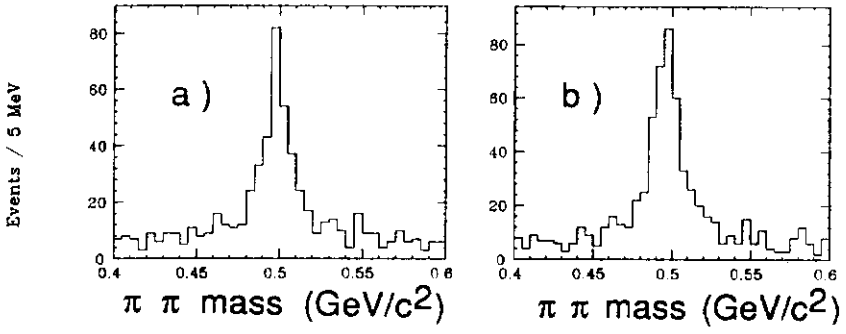

Figure 58: K_s^0 mass plots for two reconstruction vee topologies: a) decays occurring between P0 and P1 and b) decays between P1 and P2.

Table 9: Kink Decay Particles

Number	Particle and Decay Mode(s)
1	$K^- \rightarrow \mu^- \nu$, $K^- \rightarrow \pi^- \pi^0$
2	$\pi^- \rightarrow \mu^- \nu$
3	$\Sigma^+ \rightarrow p\pi^0$,$\Sigma^+ \rightarrow n\pi^+$
4	$\Sigma^- \rightarrow n\pi^-$
5	$\Xi^- \rightarrow \pi^- \Lambda^0$
6	$\Omega^- \rightarrow K^- \Lambda^0$

4.1.6 Kinks

The term "kink" refers to a decay where a charged particle passes through the microstrip detector and then decays to a single charged track and a missing neutral particle. The decay volume is from the end of the microstrip detector to the main spectrometer chamber P0. Although it is possible (and was performed in previous experiments) there has been no attempt to reconstruct charged particle decays in M2. Table 9 shows the decays that can be reconstructed from the "kink" topology. Anti-particles are included.

The reconstruction technique involves running the kink routines after all other PWC tracking, SSD tracking, and vee routines are called. Only microstrip tracks which do not link and which point into the M1 aperture are used. The requirement that the microstrip track point into the M1 aperture is employed to eliminate very low momentum target fragments. Next, all unlinked main spectrometer tracks are chosen as possible candidates for a kink. Vee candidate tracks are also not considered as potential kinks. A successful candidate has a decay point as determined by an intersection in the X view of the microstrip track and the main spectrometer track between the microstrip detector and P0.

Next, the momenta of both the parent and the daughter are calculated using each of the 6 possible decay hypotheses. The daughter track must always have the same sign charge as the parent; it must also have less momentum than the parent.

Two separate techniques are used depending on whether the main spectrometer track is a 5-chamber track or a 3-chamber track. The 5-chamber tracks have their momentum determined by M2 and hence by tracing them back through M1, their x and y position can be determined at any z position. Initially, the z position determined by the intersection of the microstrip track and the PWC track in the non-bend view is used to determine the parent momentum. If the intersection point is in the magnet, then the parent momentum can be uniquely determined. If the intersection point is upstream of M1, then there is a two-fold ambiguity in the momentum of the parent particle.

Intersections of 3-chamber tracks and microstrip tracks are only used when they occur upstream of M1. The non-bend view determines the z of the intersection point and the PWC 3-chamber track is traced upstream to the parent y position. Once, again there is a two-fold ambiguity in the parent momentum.

4.2 Čerenkov Counter Analysis and Charged Particle Identification

The following is a discussion of the procedure by which a track is identified using information from the 3 Čerenkov counters.

Charged tracks traversing the Čerenkov counters can be categorized as either electrons, pions, kaons, or protons. These 4 particles, which comprise the majority of all tracks emitting Čerenkov radiation in the experiment, have different threshold momenta at which they begin to radiate (see Table 7). Using the known momentum of a particular track in an event and the properties of the gas in each counter, a hypothesis is established concerning its light deposition in the counters for each of the 4 presumed identities. The actual presence or absence of light in a counter will contradict some of the hypotheses. Those particle types are then excluded as possible identities of the track. To the extent that the 3 counters agree on the allowed categories, the track may be definitely identified as one of the 4 particles or may remain ambiguous between several categories.

The approach involves first determining if a track radiated light in a counter. Each of the 100 or so cells in a counter yields PMT pulse height information which is read from ADCs for each event. The cell is called "on" if the pulse height exceeds a threshold, typically several pC above pedestal. For a given track, the relevant cells being examined are the one struck by the track and all adjacent cells. An anticipated light yield, based on photoelectron calibration of the counters, is calculated for each of these cells. The amount of light expected in a particular cell is a function of the particle hypothesis, the particle

momentum, and the geometric overlap of the particle's Čerenkov cone with the cell. Predicted light yields of tracks are calculated initially for pion and electron hypotheses, depending on the momentum, and the analysis is iterated to choose the better assumption. If the actual pulse height exceeds a low noise level in any cell predicted to have light from this track, the counter is said to be "on" for that track. If, however, more than one track could have contributed a significant amount of light in that cell or cells, the counter is said to be "confused" for that track. When the anticipated light yield from all "off" cells associated with the track exceeds a certain value, the counter is called "off" for that track provided the track was not previously called "on". The algorithm is therefore biased towards calling the counter on, which in turn means that tracks are more likely to be assigned to light particle categories and less likely to be falsely assigned to a heavy particle category.

Once the response to the track in each counter is found, a table of particle consistencies is set up. For example: counter C2 may be "on" for a track with a momentum just above its kaon threshold (see Table 7). In this case, the track is consistent with being an electron, pion, or kaon according to C2. If the same track has a momentum just above the pion threshold of C1 which is also "on" for that track, it is consistent with being an electron or a pion according to C1. When combined logically, information on the particle identification from all 3 counters places the track in a more precise identification category. The possible identification categories are listed in Table 14. In the example above, combined information from C1 and C2 identifies the track in question as e/π ambiguous. Information from C3 may serve to confirm or contradict this classification. In the case of a contradiction, no identification is given to the track. This will occur when one of the counters fails to detect Čerenkov light or if a signal in a cell is falsely attributed to a track. Some of these over-specified tracks can be recovered by ignoring information from counters which are "off" when the track has a momentum above the proton threshold. Otherwise these tracks remain unidentified to avoid any false classification.

Tracks can be under-specified by the Čerenkov system as well. These are cases where the identification remains ambiguous between light and heavy particles, most often in $e/\pi/K$, $\pi/K/P$, and $e/\pi/K/P$ categories. High momentum tracks are often under-specified because they exceed the highest threshold in one or more counters. The counter thresholds therefore determine a momentum range for each particle type beyond which the system is incapable of making specific identification. This is an important point when considering the overall performance of the Čerenkov system.

4.3 Muon System Performance, Muon Identification and the J/ψ

In order to establish a criterion for muon identification, one must have a good understanding of the efficiency of the muon system. The efficiency of the muon detector is measured with PWC tracks (in special muon runs) projected to the muon system. An allowance for multiple scattering is made by defining a circle of radius $3\sigma_t(p)$ around the straight line projection. A search is made for a corresponding hit within this circle. $\sigma_t(p)$, the deviation due to multiple scattering, was found from a fit to the equation:

$$\sigma_i^2(p) = \frac{\alpha_i^2}{p^2} + \frac{\beta_i^2}{p^3} + \sigma_i^2, \tag{11}$$

where α_i, β_i and σ_i are the fit parameters and p is the momentum of the particle. The data points for this fit are derived from distributions of the deviations between the projected hit position and the center of the nearest proportional tube which was hit. The fitted values of σ_i were in agreement with the physical width of the proportional tubes[17]. Thus, in measuring the efficiency, the border of the search circle was calculated as:

$$x = x_p + 3\sigma_t \cos\theta \tag{12}$$

$$y = y_p + 3\sigma_t \sin\theta \tag{13}$$

where x_p and y_p are the coordinates of the straight line projections and the angle θ varies from 0 to 2π. For the counter planes, the parameters used in calculating σ_t are the same as for the proportional tube plane immediately upstream.

The efficiency is defined as the number of muon tracks with hits within the projected cone of the PWC track divided by the total number of tracks pointing toward the detector. The average efficiencies of the arrays of counters are shown in Table 10.

For the photoproduction runs, the criterion for muon identification is based on counting the number of inner muon planes matched. In deciding which criterion to use, several $J/\psi \rightarrow \mu^+\mu^-$ samples taken from the dimuon trigger data were studied. Each sample contained only events with two oppositely charged tracks and differed from the others in the criterion that was used to identify the muons. The distribution of the dimuon invariant mass ($M_{\mu^+\mu^-}$) in the region of the J/ψ mass, shows a clear J/ψ signal. The ratio of background to signal was studied for various muon identification criteria and was used to determine the overall efficiency and rejection with each criterion.

Figure 59 shows that requiring 5 out of 7 muon planes to identify a muon gives a good signal/background ratio while not diminishing the signal significantly. It should be pointed out that this definition requires at least one fired channel in the back planes of the inner muon system. The probability that a muon is identified as a muon by this procedure, calculated from the efficiencies of the individual counters, is 98.36%.

Detector Name	efficiency [%]
IM1V	99.76
IM1H	99.86
IM2H	99.82
IM1X	85.76
IM1Y	84.08
IM2X	81.40
IM2Y	82.55

Table 10: Average efficiency of muon arrays

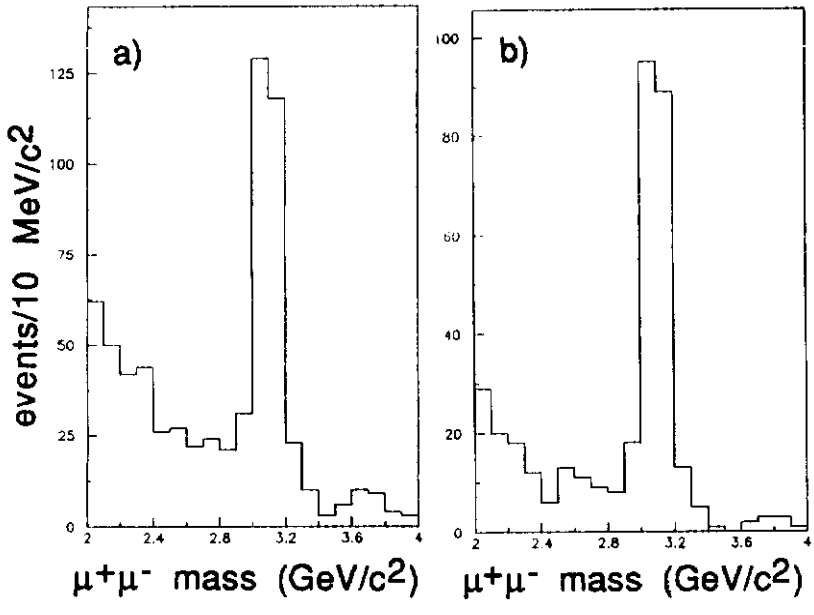

Figure 59: Efficiency of muon counters obtained from topologically identified J/ψ's. a) shows the invariant mass distribution for all two track events recorded with the muon trigger; b) has the additional requirement that each track must match at least 5 (out of 7) muon detector planes.

The muon runs were analyzed with the muon identification requirement and the muon identification efficiency was found to be 97.85%, in good agreement with the prediction from efficiency measurements for the individual counters.

During the 20 s beam spill, the singles rate of the 2.0 m by 3.0 m Inner Muon hodoscope plane was about 1 MHz. The Inner Muon trigger, which required at least 2 of the hodoscope planes to have at least 2 channels of counters on, had a rate of about 5 Hz, which made up about 5% of the data written to tape. The Inner Muon trigger efficiency, determined by Monte Carlo, for J/ψ's decaying to 2 muons was over 95% for events within the geometric acceptance of the muon detectors.

4.4 Performance of the Electromagnetic Calorimetry

4.4.1 The Response of the OE and IE to Minimum Ionizing Particles

Muons, pions and electrons have been used to determine the OE and IE counter geometry, to measure their light attenuation curves, to equalise their gains and to calibrate the energy scale of the electromagnetic (e.m.) calorimeters. The counters' response to m.i.p.'s was studied in the laboratory before the whole detector was assembled. High voltages were set to position the counter outputs for one m.i.p. at a suitable ADC channel, as shown in Table 11. This provides a dynamic range up to 25 GeV for the OE, and up to 90 GeV for the IE.

The TM counters described previously provide a trigger signal for muons in the forward region $\sim \pm 40$ mrad. The OE movement allows one to illuminate even the outermost counters with muons by moving them onto the beamline. The expected Landau distribution is smeared by inclined muon tracks, sharing energy between two counters. However, the peak position is used to verify and, if necessary, adjust the PMT gain, reaching an approximate ($\pm 20\%$) equalisation for all counters. After the equalisation, profiles for all counters are determined by plotting their efficiencies, at a typical threshold of 0.3 m.i.p., as a function of the track impact point measured by the MWPC. This is shown in Fig. 60. By excluding tracks depositing more than 0.1 m.i.p. in the nearby counters, an energy distribution, shown in Fig. 61, is obtained that can be fitted with the proper Landau curve.

A 30 GeV pion beam was also used for the same purpose. A very narrow beam of pions were defined by a system of three scintillation counters located upstream and downstream of the OE. The beam size was 1 cm $\times$ 1 cm and its divergence was $\pm$4mrad. Pions interacting in the calorimeter were rejected using anticoincidence counters. Simulations show that hadronic showers are suppressed in this setup by better than a factor 10^2.

Figure 62 shows typical attenuation curves for counters with different lengths and widths. By following the described procedure, peaks of Landau distributions are used to intercalibrate the counters, and to fit their attenuation curves.

Table 11: Settings for minimum ionizing particles in various sampling segments of the OE and IE

OUTER ELECTROMAGNETIC							
	OE0	OE9S	OE9Z	OE1V	OE1H	OE2V	OE2H
ADC counts	600	600	600	300	300	300	300
pC	30	30	30	15	15	15	15
INNER ELECTROMAGNETIC							
	IE1V	IE1H	IE2V	IE2H	IEPADS	IE3V	IE3H
ADC counts	100	100	100	100	100	100	100
pC	5	5	5	5	5	5	5

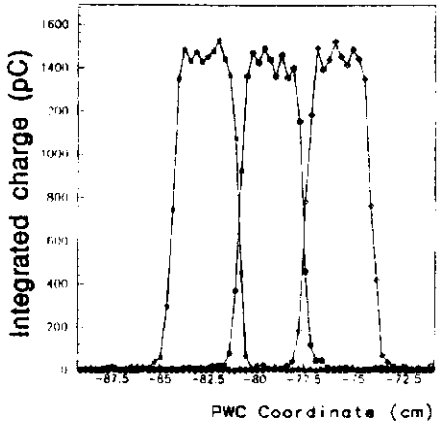

Figure 60: Efficiency curve for counters as a function of impact point extrapolated from PWC track parameters. This shows the precision of the determination of their location.

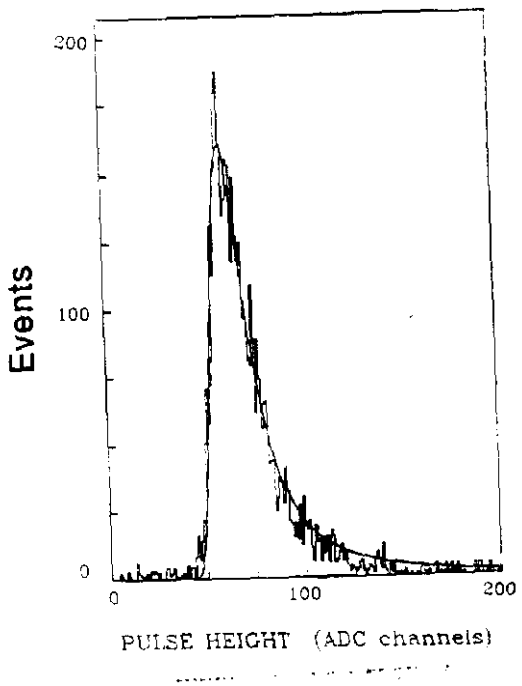

Figure 61: Typical response of a five-fold counter to muons.

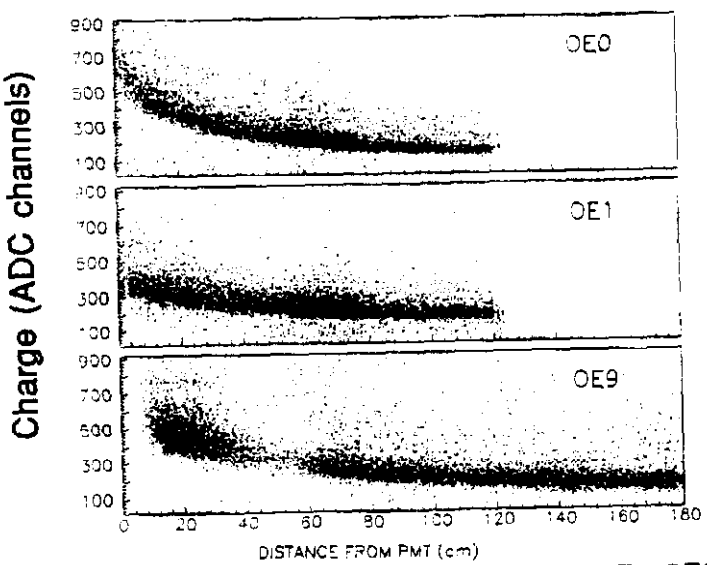

Figure 62: Examples of attenuation curves for a counter in OE9, OE0, and OE1, obtained summing data from several muon calibration runs.

4.4.2 Energy Calibration, Resolution and Performances

The energy range for photons and electrons in the calorimeter acceptances was studied using a Monte Carlo program[44] based on a photon-gluon fusion model and the Lund fragmentation model. The program predicts typical photon energies for the OE (IE) in the range 1-10GeV (10-100GeV), while electron energies in charm semileptonic decays go up to 30GeV (60GeV).

The response of the calorimeters to photon- and electron-initiated e.m. showers, their linearity, the scale factor between detected energy and incident energy, and their energy resolutions have been studied using a GEANT simulation.

The detected energy is parametrized as

$$E_{detect} = \frac{E}{\alpha} \pm \frac{\sigma_{FWHM}\sqrt{E}}{\alpha} \,[\mathrm{GeV}] \tag{14}$$

where E is the particle incident energy, E_{detect} is the particle energy deposit in the calorimeter's active layers, and $\sigma_{FWHM} \equiv FWHM/2.36$ is the relative energy resolution at $E = 1\,\mathrm{GeV}$.

For the OE, $\alpha_{MC} = 5.58 \pm 0.02$ when computed at $E = 10\,GeV$. The variation of α_{MC} is $\pm 5\%$ in the range $E = 1 - 6\,\mathrm{GeV}$ and only $\pm 2\%$ for $E \geq 6\,GeV$, while an energy resolution $\sigma_{FWHM} = 13\%$ is predicted.

The energy scale and resolution predicted from Monte Carlo studies have been verified using physics signals. The reconstruction algorithms for neutral showers begin with the identification of clustered energy deposits associated with the projections of charged tracks reconstructed in the magnetic spectrometer. Remaining clusters in the two orthogonal x-y views are coupled using diagonal counters and energy balance criteria. The shower centroids, once corrected for systematic effects, determine the impact point of photons. The typical resolution on the shower position, as measured by the sampling at shower maximum, is $\pm 0.9\,\mathrm{cm}$ at $3\,\mathrm{GeV}$ and $\pm 0.3\,\mathrm{cm}$ at $10\,\mathrm{GeV}$.

Energy deposits (in ADC counts) in each counter are multiplied by calibration constants, corrected for light attenuation in the counters, and then summed up to determine the detected energy associated with each cluster. Finally, the sum of energy clusters longitudinally forming a reconstructed photon track enters Eq. 14 as the detected energy term.

The position of invariant mass peak for the π^0(Fig. 63a)) was used to fine tune the energy scale. Optimization of the peak position provides $\alpha_{OE} = 5.87 \pm 0.13$, while the experimental width observed is compatible with $\sigma_{FWHM} = 15\%$, in agreement with the resolution predicted by the simulation.

Broad band electrons in the momentum range 10-20 GeV were also used for energy calibration, yielding results in overall agreement with the other methods. The OE response to a primary beam of nominally 18 GeV electrons, with a momentum spread $\sim 30\%$, is shown in Fig. 64. Electron energy deposits are clearly visible, along with those from contaminating m.i.p.'s and showering hadrons.

The OE and IE calorimeters significantly extend the $e - \pi$ rejection range beyond the Cerenkov momentum range, to include from 6 to 25 GeV and from 17 to 90 GeV.

To optimize the algorithms for electron identification, e^+e^- primary Bethe-Heitler pairs and e^+e^- Bethe-Heitler pairs from photon conversions in hadronic events, can be used. The E687 magnetic spectrometer is used to measure the $e^-(e^+)$ momentum (with $\sigma(p)/p \leq 0.5\%$ in the momentum range of interest). To reproduce standard experimental conditions, the analysis magnets are set to the currents used during normal data taking. The correlation between the energy deposit in the calorimeter and the electron momentum measured in the spectrometer is shown in Fig. 65.

The electron identification algorithms have been developed in the framework of Discriminant Analysis[45], which allows efficient differentiation between two or more groups of events, once a set of meaningful variables (called "Discriminant Variables") is found, which provides good discrimination for cases with known group membership. Muons, beam pions, pions from K^0_s decay, and e^+e^- pairs are used to form the "known" group. The patterns of energy deposits and the ratio E/p between the energy measured by the calorimeters and the track momentum, p, as measured by the magnetic spectrometer were used as discriminant variables. The overall hadron rejection obtained for a 90% electron identification efficiency is $\sim 10^2$, as shown in Table 12. Figure 66 shows the efficiency for electrons and the residual hadron contamination as a function of the track momentum.

Energy scale, energy resolution, and rejection algorithms were determined for the IE following the procedures described for the OE. However, in order to improve the IE pattern reconstruction capabilities for solving x-y ambiguities for both photons and electrons in crowded events, only one (x or y view) energy sampling is used. The energy scale experimentally tuned by the ω^0 mass peak (Fig. 63b) is $\alpha_{IE} = 5.89$, while the observed resolution, $\sigma_{FWHM} = 16\%$, is consistent with the Monte Carlo predictions.

Finally, the ability of the Čerenkov counters and e.m. calorimeters to identify electrons is compared in the common momentum range, i.e. 2-6 GeV (7-17 GeV) for the two-counter (three-counter) system. Once one specializes to the subset of non-overlapping e.m. showers fully contained laterally in the calorimeters, 90% of the tracks called electrons by the two Čerenkov counters C1 and C2 are called electrons by OE and 88% of the tracks called electrons by all three Čerenkov's are called electrons by the IE. To achieve 'clean' electron identification from the Čerenkov counters tight cuts were applied so that the efficiency of C1 and C2 for wide angle electrons is 70% and of C1, C2, and C3 for smaller angle electrons is 58%.

Although the energy resolution and pattern recognition capability of the E687 e.m. calorimeters were significantly degraded by the modifications to their sampling structure with respect to the original design, they still provide good $e-\pi$ separation which can be used to identify electrons from semi-leptonic charm

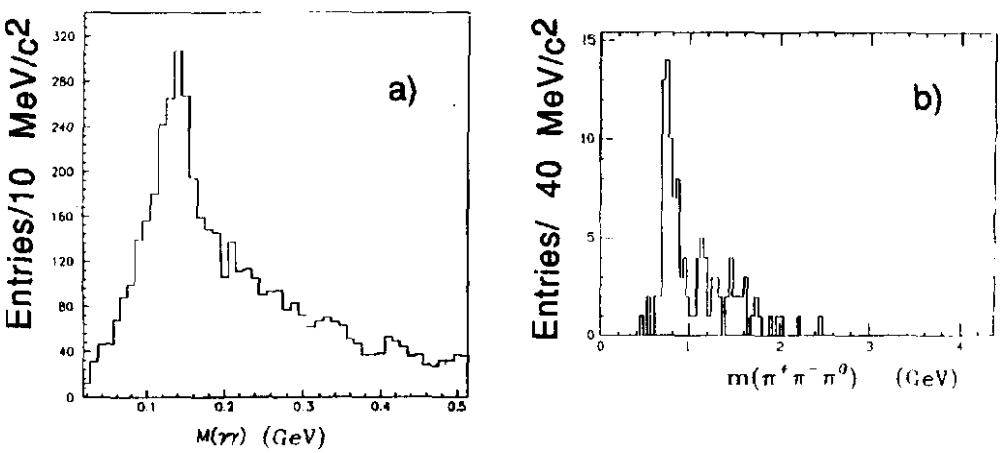

Figure 63: Invariant mass distributions for a)$\gamma\gamma$ in the OE and b)$\pi^+\pi^-\gamma\gamma$ in the IE, showing signals for π^0 and ω^0, respectively.

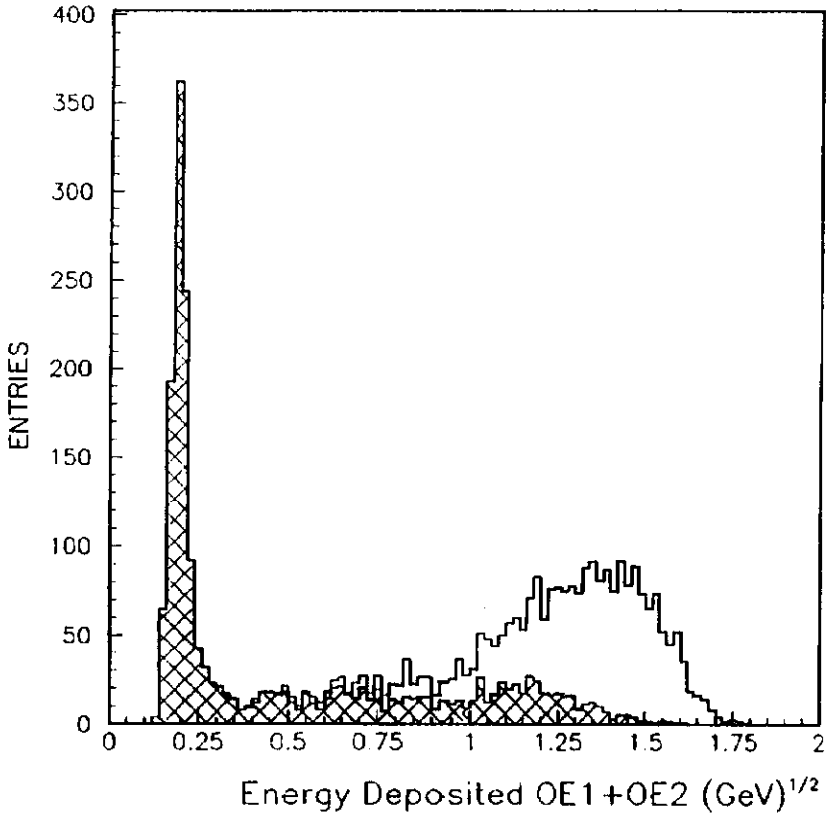

Figure 64: OE response to a nominal 18 GeV electron beam, contaminated with m.i.p.'s and showering hadrons. Shaded area is showers identified as hadrons by the algorithm.

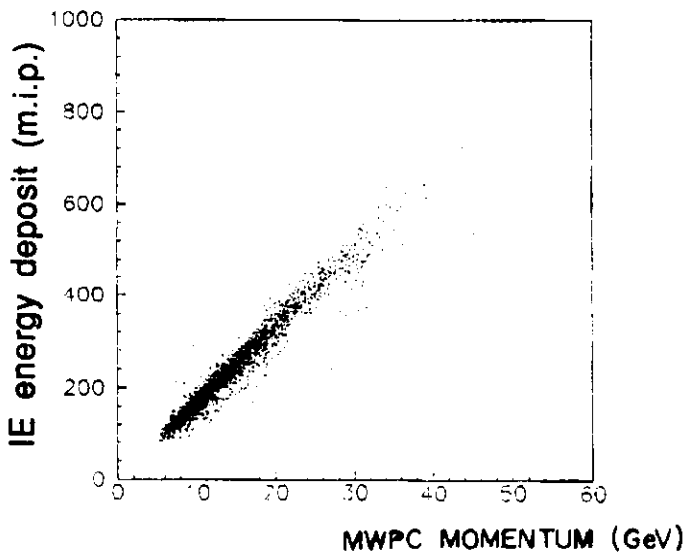

Figure 65: The scatter plot of energy detected in the calorimeters versus momentum measured by the magnetic spectrometer for electrons and positrons from an e^+e^- sample. The expected correlation around $E/p = 1$ is obtained.

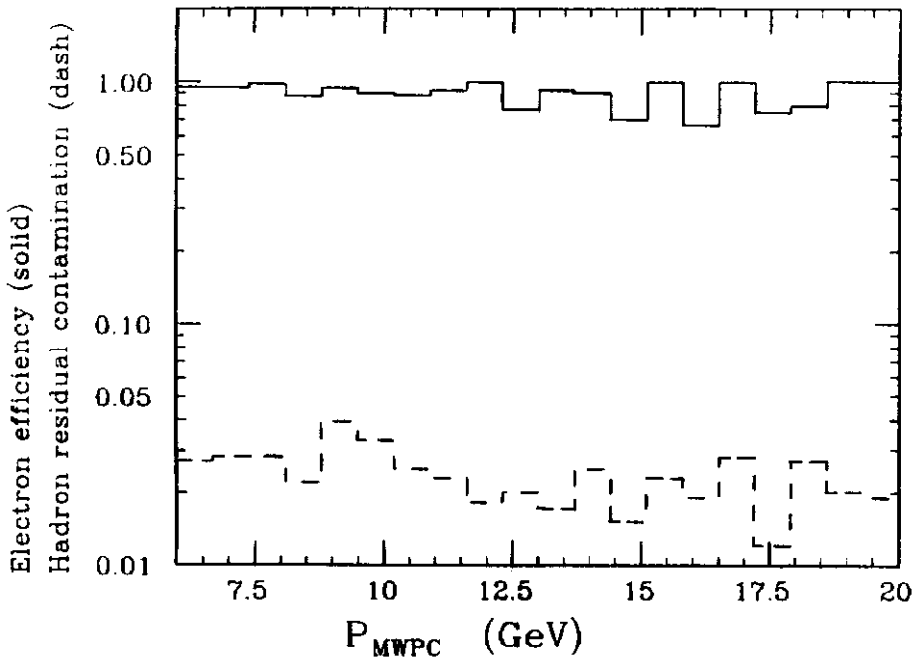

Figure 66: Electron efficiency and residual hadron contamination as a function of track momentum measured by the spectrometer

Table 12: Efficiency for identifying $e^{\pm}$ conversion pairs in hadronic events and residual contamination for pions from K_s^0 decays in the OE e.m. calorimeter. A momentum cut greater than 6 GeV is applied.

	Electron efficiency	Hadron residual contamination
Shower longitudinal development	0.90	0.090
as above, + shower lateral width	0.90	0.048
as above, + E/p	0.90	0.021

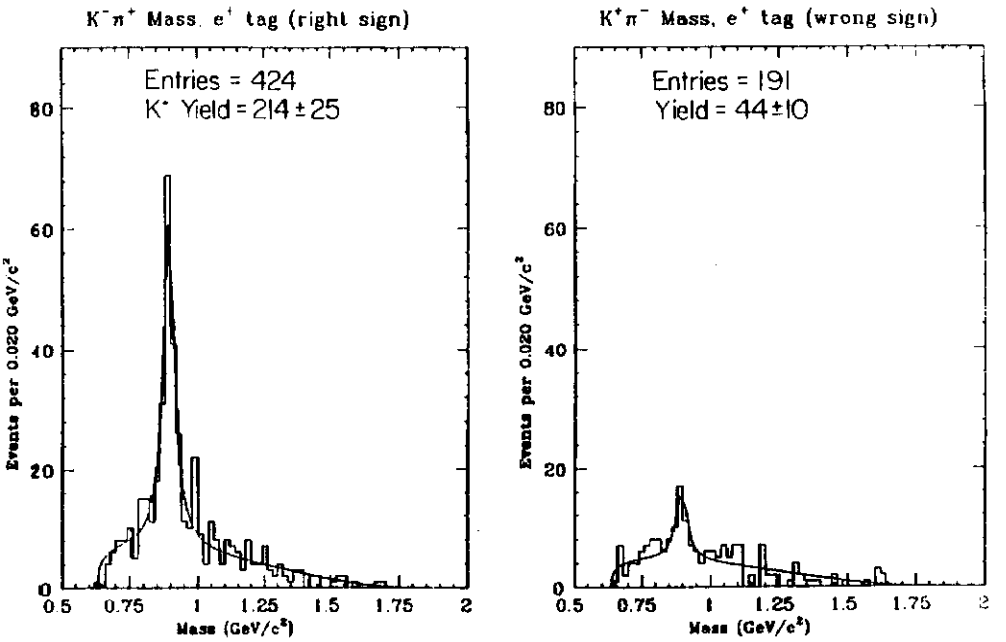

Figure 67: Distribution of $K\pi$ invariant mass, showing the $\bar{K}^{*0}$ signal from the semileptonic decay $D^{*+} \to \bar{K}^{*0}e^+\nu_e$. Electrons are identified by the calorimeters .

decays and a significant photon reconstruction capability for charm events with low neutral multiplicity. Figure 67 shows the $\bar{K}^{*0}$ invariant mass peak from the semileptonic decay $D^{*+} \to \bar{K}^{*0}e^+\nu_e$, where the electron is identified by the e.m. calorimeters.

4.5 Monte Carlo Simulation of the Detector

Two complementary software packages are used to simulate the detector response to minimum bias, J/ψ, open charm, and beauty events. One of them is based on the GEANT3[46] system written at CERN; the other one is a stand-alone program named ROGUE[47] written specifically for this detector. In addition, the performance of specific subdetector elements such as the beam tagging system, the microstrip detector and the Čerenkov counters were studied in great part with small, dedicated stand-alone Monte Carlo programs.

GEANT3 allows a complete and detailed simulation of particle tracking as well as calorimetry. Its graphic capability was useful at early stages of the design of the tracking reconstruction software to understand and locate pattern recognition issues (Fig. 68). All detector elements were included in this GEANT3 based package. Some of them used detailed simulation tools available in GEANT3 such as hits and digitisation data structures. Others were based on the stand-alone subpackages mentioned above. The GEANT3 infrastructure allows the construction of a coherent and manageable "global" Monte Carlo package capable of generating "fake" data tapes for a wide variety of

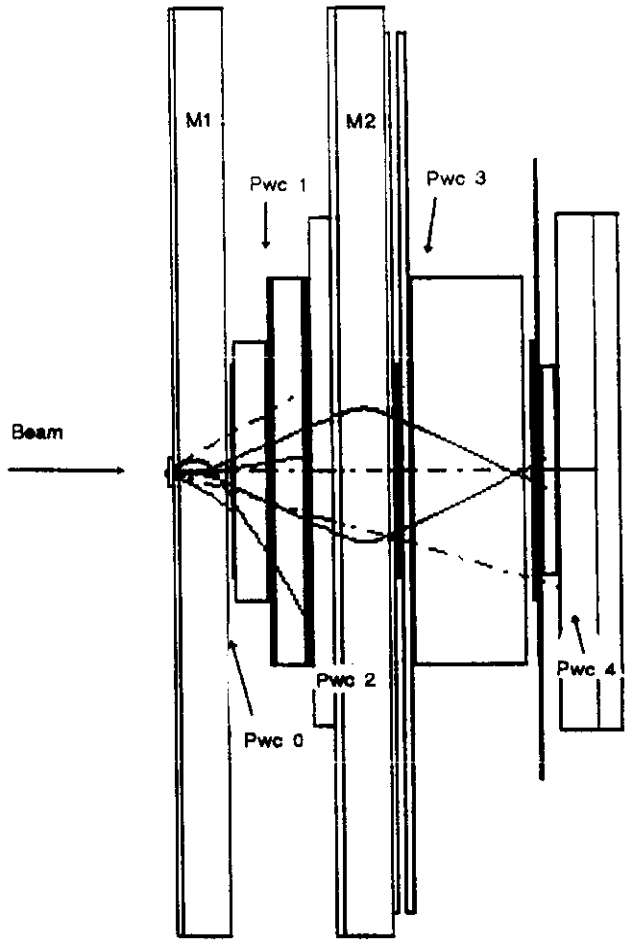

Figure 68: Picture of an event from the GEANT3 Monte Carlo

processes. Since the format of these "raw" Monte Carlo data tapes simulates exactly the back-end I/O layer of the data acquisition system, no modifications are required to the PASS1 reconstruction program to compute effective acceptances, resolutions, efficiencies, etc. A so-called "god's block", which contains detailed information about the generated event, is appended to the output record for each event. GEANT3 is interfaced to a recent version of the program Lucifer[48], which is part of the LUND family of event generation programs. Lucifer permits great flexibility in specification of the production dynamics and fragmentation schemes used to generate the events. GEANT3's complete shower simulation capability has been used extensively to check the position and energy resolution of the electromagnetic and hadronic calorimeters. An approximate showering model, based on real data as well GEANT3 studies, was used to simulate the hadron calorimeter response and the related second level-trigger bias for the production runs to keep the computing requirements within acceptable limits.

ROGUE avoided the major limitation of the GEANT3 system, namely it's

speed. The speedup is achieved by hard-wiring the geometry into the program to avoid the overheads paid by GEANT to search through more general (and flexible) structures and by using experiment specific information to reduce computing requirements wherever possible. In addition, the much simpler software infrastructure of ROGUE allowed great flexibility in speed optimization. The GEANT3 based Monte Carlo package simulates a complete open charm event in approximately 22 VAX 780 seconds, while ROGUE is able to simulate the same kind of events in 3 VAX 780 seconds.

The ROGUE package consists of the following major components: GENERIC, an event generator; CHAT, a user-friendly interactive front end for defining a physics problem to GENERIC; and ROGUE which handles the detector simulation and writes the "fake" tape.

GENERIC performs the simulation of the incident beam, the production of the primary charm or beauty mesons and baryons, and the decays of all unstable particles. The incident photon generation begins with the measured electron distribution at the radiator. Electrons generated according to this distribution are followed through the radiator and the resulting collection of photons is traced to the target. If a photon intersects the target (the beam is bigger than the target), it is allowed to interact. The number of electrons required to produce the charm sample is recorded to help in the normalisation of the data. The user has flexibility in the definition of the physics processes which occur when the photon interacts. For example, she may choose to generate a particular decay mode for either or both charmed particles or may force one type of charm particle to be produced and to decay into a specific mode while permitting the opposite side to have a variety of charmed states produced and to decay into a whole variety of different final states. The program offers various options with respect to the initial charm particle dynamics including one generator based on photon-gluon fusion and Feynman-Field fragmentation into hadrons and another one based on experimental measurements of inclusive charm photoproduction [49]. Target jets are formed by Feynman-Field fragmentation of the backward-going quarks to complete the event.

The program ROGUE simulates the response of the spectrometer to the particles as well as the responses of the particles (magnetic deflection,multiple Coulomb scattering,etc.) to the spectrometer. The basic philosophy of ROGUE is to trace each final state particle produced by GENERIC in turn, by stepping the particle to specified stopping locations, until the particle uses up its decay path, fails to clear an aperture, or leaves the spectrometer. Stopping locations are points where some action must be taken: at silicon planes or wire chambers to simulate hits, in Čerenkov radiators to generate photons (and trace them to PMT's), at specified points for multiple scattering, at the aperture of a device to determine if the particle is accepted by it. After all the particles are tracked, the event is digitized and written to tape. ROGUE has the ability to drop hits to simulate chamber inefficiency and to add hits to simulate noise. Multiple scattering is handled by applying a simple Gaussian model at specified stopping

locations. Electrons are allowed undergo bremsstrahlung in the spectrometer. Response of trigger counters is also simulated. The hadrometer portion of the trigger is simulated using the same approximate distribution employed by the GEANT3 program. ROGUE does not have the ability to generate showers for either hadrons or photons.

A detailed evaluation of the results on Monte Carlo data is required to certify the reconstruction program. Correct estimation of the tracking resolution - mostly dominated by multiple scattering for the inner spectrometer - is essential for lifetime measurements. Understanding the systematic effects in momentum measurements is required to achieve the best mass resolution. Large samples of events are required to compute efficiencies and acceptances. For this reason, the ROGUE program has been extensively employed as a production Monte Carlo. On the other hand, detailed understanding of the calorimetry and muon identification have taken advantage of the capabilities of the GEANT3 program.

5 Vertex Reconstruction

The ability to separate tracks coming from the primary interaction vertex from those coming from secondary decays occurring on the order of a few hundred microns downstream is the key to obtaining clean samples of states containing heavy quarks with lifetimes in the $10^{-12} - 10^{-13}$ second range. By using only those tracks coming from a downstream vertex in mass combinations, combinatoric backgrounds can be significantly reduced and mass peaks with good signal to background ratios can be obtained. Two different and complementary algorithms which are used for vertex reconstruction are described below. Each of these techniques has succeeded in producing striking charm signals in a variety of final states. A clear understanding of the relative strengths and weaknesses of these two approaches has been achieved and has contributed to the understanding of the optimal way to perform vertex reconstruction.

5.1 Candidate Driven Vertex Algorithm

The basic idea of this algorithm is to use a charm candidate as a seed to find the primary vertex. A combination of tracks consistent with a given charm (or beauty) decay mode is selected. This includes, for example, selection of particle combinations such as $K\pi\pi$ with the right charge and strangeness correlation. The candidate tracks which form the charm particle are then fitted to the hypothesis of a common vertex. If they conform to this hypothesis with a confidence level greater than a specified minimum, typically ≥ 0.02, then the cluster is accepted as a 'candidate'. The full covariance matrices of each track comprising the candidate are used to generate a charm "track", which then is fitted to a common vertex with all other SSD tracks one at a time. All tracks which form a vertex with the candidate with a confidence level $> .02$ are put into a list. The tracks in this list are combined pairwise with the candidate and the pair with the best confidence level is kept as a primary vertex. The algorithm then loops over the other microstrip tracks adding one track to the primary and refitting, always keeping the best track from each iteration. When the best remaining track has a confidence level $< .02$ for coming from this vertex, the search terminates. In addition to fits of the primary and secondary vertices, a global fit is applied to the decay tracks to find the decay length, L. The quantity $\frac{L}{\sigma_L}$, where σ_L is the calculated uncertainty in L, is then an unbiased measure of the significance of detachment of the secondary vertex. Cuts on $\frac{L}{\sigma_L}$ can be used to improve the signal to background by requiring more significant separations at the cost, of course, of some signal. The method works efficiently since the resolution is much smaller than the typical decay lengths so that the loss of signal required to reduce the background is not too severe.

Since it is possible to obtain charm signals in the decay chain $D^{*+} \rightarrow D\pi^+ \rightarrow (K^-\pi^+)\pi^+$ without using vertex constraints, the absolute efficiency for finding a successful primary vertex with this algorithm can be determined. It is just the

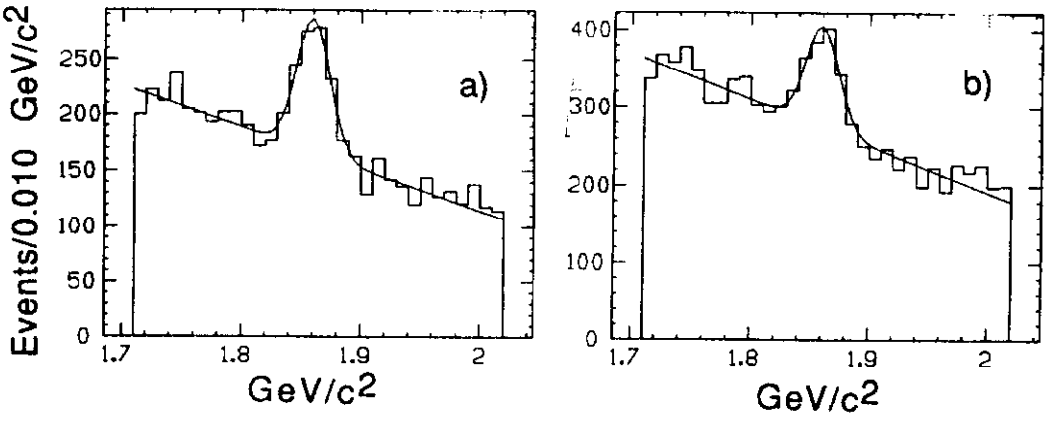

Figure 69: Primary vertex finding efficiency obtained from D^* signal. a) $K\pi$ combinations with a primary vertex b) All $K\pi$ combinations.

ratio of signal peak area for events from this decay chain with a primary vertex, Fig. 69a) to the peak area for all events, Fig. 69b). Fits to these histograms give an efficiency of 90% for this algorithm.

The validity of the Candidate Driven Vertex Algorithm can also be determined by examining the $\frac{L}{\sigma_L}$ distribution for noncharm candidates. Since these candidates should be random combinations of tracks coming from the primary vertex, the $\frac{L}{\sigma_L}$ distribution should be a Gaussian of unit width if the errors have been correctly calculated. Noncharm candidates are defined to be track combinations which fall more than 5σ away from the ΔM and D^0 mass values which define a D^* decay. Figure 70 shows the background $\frac{L}{\sigma_L}$ distribution for the noncharm $K\pi$ mass combinations. A fit gives a width of $1.01\pm.02$ showing that the resolution functions are correct.

Figure 71 shows the combined yield of $K\pi$ (x's) and $K3\pi$ ($\diamond$'s) from D^*'s surviving cuts on minimum $\frac{L}{\sigma_L}$ as a function of the cut value. The dashed curve gives the survival probability as a function of $\frac{L}{\sigma_L}$ from the Monte Carlo. The slope of this line implies a Monte Carlo lifetime resolution of .044 ps. This " effective" resolution combines uncertainty in both the primary and secondary vertices.

5.2 Stand-alone Vertex Algorithm

This algorithm uses only the microstrip information to determine vertex assignments and attempts to reconstruct the whole vertex topology of the event.

The method is based on an iterative procedure which, given a certain number of tracks, tries to build a vertex, disregarding, in each iteration, the track giving the largest χ^2 contribution. The procedure ends when the global χ^2 of the vertex becomes smaller than a specified value. As a first trial, the vertexing

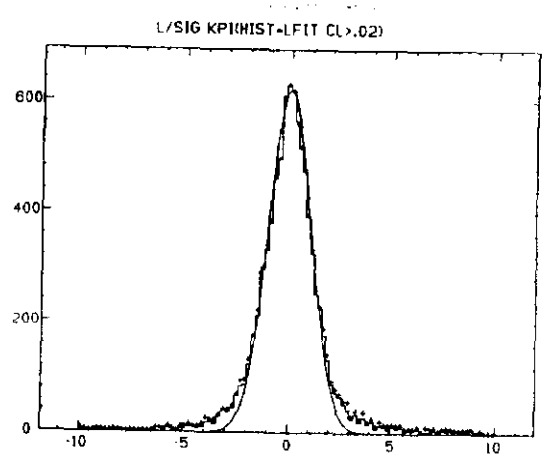

Figure 70: Background $\frac{L}{\sigma_L}$ distribution for noncharm $K\pi$ mass combinations

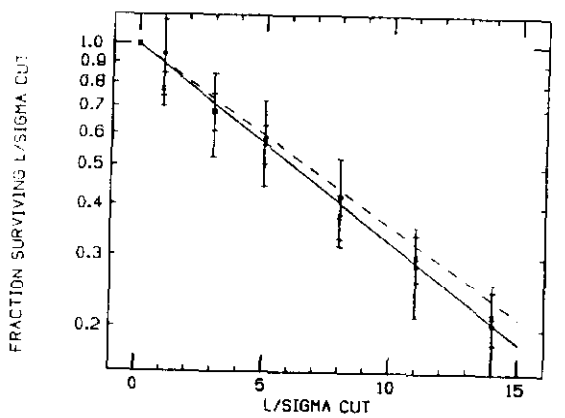

Figure 71: Yield of D candidates surviving various $\frac{L}{\sigma_L}$ cuts

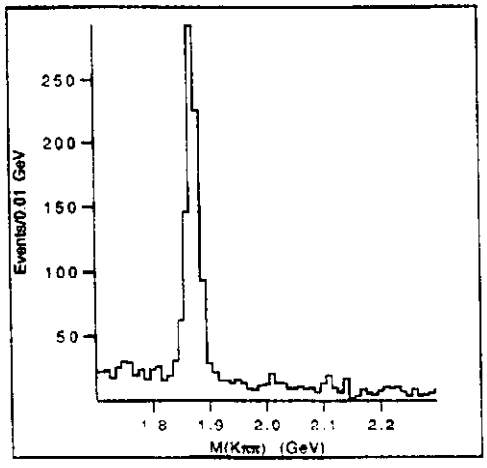

Figure 72: Invariant mass distribution for $K^-\pi^+\pi^+$ secondary vertices obtained with the Stand-alone Vertex Algorithm. The D^+ signal is clearly seen over a small background.

algorithm assigns all the tracks to a common vertex. In successive phases, only the tracks not previously included in a vertex are considered. Each time a vertex is found, the program then tries to add to the same vertex other tracks which could have been erroneously disregarded or simply not considered since they were already assigned to another vertex. The vertex fitting procedure does not make use of the reconstructed track parameters, but performs a new fit using the associated hits, with the constraint that all the included tracks come from a common vertex point. At the end of this procedure, tracks have definite assignments to a specific vertex. Some tracks may not be assigned to any vertex and they are not permitted to enter any mass combinations.

A clear example of the performance of this vertex algorithm is given by the $D^+ \rightarrow K^-\pi^+\pi^+$ signal as observed with the simple requirement of a secondary vertex of three tracks with a net charge of ± 1, with a resulting momentum vector pointing back to a primary vertex in the target region; the K mass is attributed to the opposite sign track (Fig. 72). In this selection no Cerenkov information was used at all.

5.3 Comparison of the two algorithms

The performances of the two algorithms have been compared in detail. The characteristics of the Stand-alone Vertex Algorithm are:

- No specific decay mode is assumed. This technique is therefore able to pick up decays with missing neutrals, e. g. ν or π^0. No biases are introduced into initial selection of candidates by assumptions about final states.

- This method achieves excellent signal-to-background ratios. The method has a built in bias towards including poorly separated tracks into the primary vertex. Poorly resolved secondary vertices are lost but background is significantly reduced in the process.

- This method becomes inefficient for short lifetimes for the same reason: tracks occurring close to the primary vertex will have a good chance of being assigned to it. If even one of the decay products suffers this fate, the whole decay is lost.

The characteristics of the Candidate Driven Vertex Algorithm are:

- Even primary vertices containing only one track can be found.

- There is no efficiency problem at short lifetime because the basic method of finding an acceptable secondary vertex without checking whether there is a better assignment to the primary vertex favors assignment to the charm candidate rather than the primary vertex. This insures the efficiency of the algorithm at short lifetimes while obviously accepting additional background.

- This method allows one a wide lattitude in signal versus signal-to-noise. If one uses a relatively low $\frac{L}{\sigma_L}$ cut, one achieves several times the yield obtained with the Stand-alone Vertex Algorithm but at the expense of a much poorer signal-to-noise ratio. As the $\frac{L}{\sigma_L}$ cut is increased, both the background levels and the signal yields become quite comparable.

It is clear that there is a continuum of solutions between these two algorithms. In the search for vertices, the Stand-alone Vertex Algorithm can be relaxed by allowing reassignment of a track from the primary to the secondary vertex in cases where the track's assignment is ambiguous between the two. This improves the yield while, of course, increasing the background. In the Candidate Driven Algorithm, there are also means available to improve the signal-to-noise besides merely making a cut at larger values of $\frac{L}{\sigma_L}$. These include requiring that no other track be consistent with passing through the secondary vertex and that no track which is assigned to the candidate vertex can be combined with the tracks assigned to the primary vertex and produce an acceptable χ^2. It has thus been demonstrated that the two methods, starting from rather different philosophies and initially appearing to produce rather different results, can be made to converge by adjusting some of the requirements that they impose on the vertices that they form.

6 Performance of Tracking and Charged Particle Identification systems

6.1 Incorporation of MCS Errors

It is important to obtain realistic track covariance matrices which incorporate both detector granularity and multiple scattering errors. Many of the fits used in E687 (such as secondary vertex fits, and K_s and Λ^0 fits) involve minimization of χ^2 which should properly reflect tracking errors. Often the confidence level distributions of these fits and the widths of resolution distributions normalised to uncertainties from the data serve as important checks of the proper calibrations and alignment of the E687 apparatus.

In the act of track fitting, a fitted track parameter, t_α can be written as a linear transformation of the wire coordinates X_i of the form:

$$t_\alpha = P_{\alpha i} X_i \qquad (\textit{implied summation}) \tag{15}$$

For the case of an over-constrained system, where there are more wire planes than track parameters, different $P_{\alpha i}$ matrices which provide unbiased estimates of t_α are possible; these may differ in the choice of space point weighting. The optimal variance choice weights space points according to the true coordinate covariance matrix $< \delta X_i \delta X_j >$ which reflects both MCS and granularity weighting.

In order to reduce the computer time per event, E687 employs a simple least squares fit where the MCS contributions to the true coordinate covariance matrix are ignored. The resulting track estimates are optimal at high momentum but nonoptimal at low momenta where MCS effects predominate.

Although MCS effects are not taken into account in the track fitting their contribution can be taken into account in computing the track error matrix. In terms of the $P_{\alpha i}$ matrix, the track covariance matrix is:

$$< \delta t_\alpha \delta t_\beta >= P_{\alpha i} < \delta X_i \delta X_j > P_{\beta j} \tag{16}$$

The coordinate covariance matrix contains a diagonal term due to detector granularity and an off-diagonal momentum dependent term due to MCS.

$$< \delta X_i \, \delta X_j >= \frac{\delta_{ij}}{12} + \frac{a_{ij}}{p^2} \tag{17}$$

The off-diagonal elements of a_{ij} reflect the fact that a multiple scatter will introduce a correlated stochastic deviation in the coordinates measured by all planes downstream of the scatter point.

Equations (16) and (17) imply a momentum dependence of the form:

$$< \delta t_\alpha \delta t_\beta >= \left(1 + \frac{P^{*2}_{\alpha\beta}}{p^2}\right) < \delta t_\alpha \delta t_\beta >_\infty \tag{18}$$

where $< \delta t_\alpha \delta t_\beta >_\infty$ is the track covariance matrix element at infinite momentum and $P^{*2}_{\alpha\beta}$ is an effective squared momentum at which MCS becomes the dominant error contribution.

6.2 Microvertex Track Resolutions

Although it is possible to compute anticipated resolutions (including MCS effects) for each possible combination of high resolution and low resolution space points which can constitute an SSD track, it was impractical to use this approach from the standpoint of CPU demands (large matrix operations on every track!) and storage demands ($\approx 2^{12}$ pre-stored covariance matrices!). The solution to this problem employs a granularity weighting approach. The errors are computed for a track-related quantity by assuming the track passed entirely through the high resolution region or entirely through the low resolution region and then these variances are averaged using the fraction of high resolution and low resolution hits actually used in the given SSD track as weights:

$$\sigma^2 = f_{hi}\ \sigma^2_{hi} + (1 - f_{hi})\ \sigma^2_{low} \tag{19}$$

The resolution of a track is expressed as the error in the x-y plane for the track when extrapolated to a particular z location. The resolution extrapolated to the center of the target for a track consisting entirely of hits on high resolution strips is:

$$\sigma_x = 11\mu m\ \sqrt{1 + \left(\frac{17.5\ GeV}{p}\right)^2} \tag{20}$$

$$\sigma_y = 7.7\mu m\ \sqrt{1 + \left(\frac{25\ GeV}{p}\right)^2} \tag{21}$$

This formula contains MCS effects as given by Eq. 18 as well as MCS contributions due to the target and the TR1 trigger counter added in quadrature. The target and trigger counter increase the error by only about 20%.

The anticipated SSD resolutions are compared to the data by measuring the transverse distance from a given SSD track to a primary vertex from which the candidate track has been removed. The anticipated x and y impact error should reflect both the uncertainty in the track and the uncertainty in the vertex. Events with only one vertex are looked at and each track is considered in turn. It is removed from the vertex, the vertex is refitted using the above resolution function for each of the tracks and then the following quantities are calculated:

$$\Delta x_v = \frac{x_i - X_v}{\sigma_{(x_i - X_v)}} \quad and \quad \Delta y_v = \frac{y_i - Y_v}{\sigma_{(y_i - Y_v)}} \tag{22}$$

These quantities are shown histogrammed in Figs. 73a) and 73b) respectively with Gaussian fits superimposed. The widths of these fits are 1.12 and 1.06 respectively and demonstrate an understanding of our track resolutions at about the 10% level.

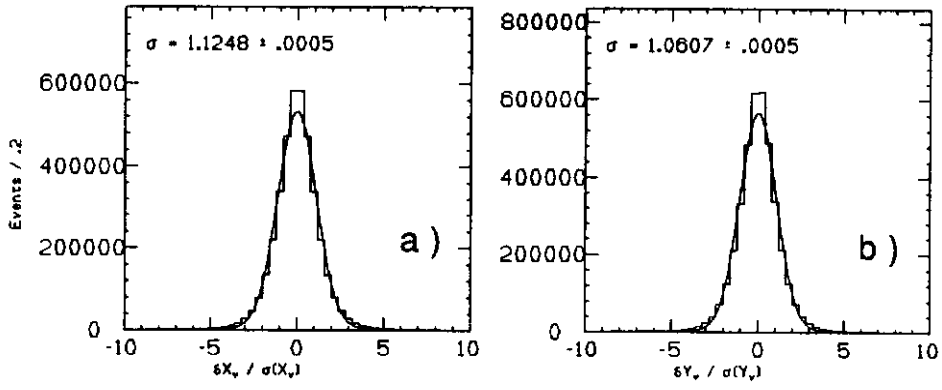

Figure 73: Distributions of normalized impact parameters in a) x and b) y for tracks at the primary vertex. The superimposed Gaussian fits demonstrate a good understanding of the resolution.

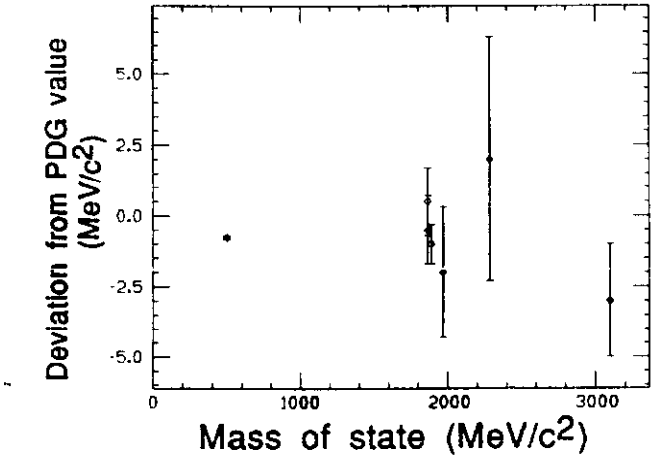

Figure 74: Comparison of the mean mass of several reconstructed mass peaks with Particle Data Group values. The difference between the value obtained in this experiment and the PDG value is plotted as a function of the PDG mass of the state.

6.3 Mass Scale and Momentum Resolution

The degree to which the magnetic aspects of the spectrometer are understood is demonstrated by comparing the reconstructed masses of well known objects with their accepted values. Figure 74 shows the reconstructed mass minus the Particle Data Group mass[50] for the K^0_s, ϕ, $D^{\pm}$, D^0, D_s, Λ_c and J/ψ. Over a mass range spanning almost 3 GeV and for wildly differing decay topologies, the systematic mass error is less then 1 MeV per GeV of mass.

The momentum resolution can be calculated for tracks whose momentum is determined by M1 or M2. The formulae which are given below contain a multiple scattering contribution similar to the one discussed earlier:

$$\frac{\sigma_p}{p} = 3.4\% \quad \left(\frac{p}{100\ GeV}\right) \quad \sqrt{1+\left(\frac{17\ GeV}{p}\right)^2} \quad for M1 \qquad (23)$$

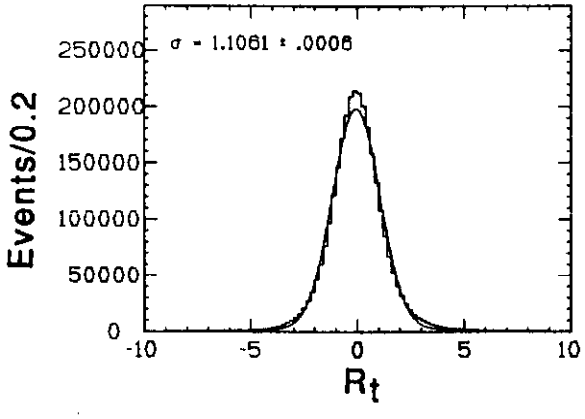

Figure 75: Comparison of momentum obtained from M1 with momentum obtained from M2. R_t is defined in the text.

$$\frac{\sigma_p}{p} = 1.4\% \quad \left(\frac{p}{100\ GeV}\right) \quad \sqrt{1 + \left(\frac{23\ GeV}{p}\right)^2} \quad for M2 \tag{24}$$

These formulae can be verified by histogramming the quantity

$$R_t = \frac{p_{M1}^{-1} - p_{M2}^{-1}}{\sigma_{pdif}}, \tag{25}$$

which is shown in Fig. 75 with a Gaussian fit superimposed. The width of the fitted Gaussian is 1.106 showing that the momentum resolution is well understood.

6.4 Performance of the Čerenkov System

The performance of the Čerenkov counter system has been studied using topologically identified states with known charged particle content. Decays such

as

$$\begin{aligned} \phi^0 &\rightarrow K^+ + K^- \\ K^{*0} &\rightarrow K^\pm + \pi^\mp \\ K_s^0 &\rightarrow \pi^+ + \pi^- \\ \Lambda^0 &\rightarrow p + \pi^- \end{aligned} \tag{26}$$

can be observed as clean peaks in the appropriate invariant mass distributions without relying on the Čerenkov counter identifications. The Čerenkov counter performance can then be evaluated by seeing how often the Čerenkov analysis obtains the correct identification for the charged hadrons in these states. The signals for these decays are copious, allowing for very high statistics studies. By use of strict cuts on the vertex separation, clean samples of D-mesons can also be obtained without using Čerenkov information. These can also be used to verify the performance of the Čerenkov system and the analysis algorithms but with lower statistics. Finally, detailed simulations of the Čerenkov performance have been performed and tuned carefully against the data. These provide additional insight into the capabilities and limitations of the detectors and analysis techniques.

The efficiency studies are accomplished by measuring the signal in some mass peak from a topological analysis and then from the same analysis but with additional requirements on the Čerenkov particle identification. Two different techniques are used to eliminate the background and get a measurement of the true amount of signal: fits to the invariant mass histograms; and sideband subtraction.

The first method is useful for cases where restrictions on the momentum and other quantities are applied and the statistics are poor. An example of this is the decay of D mesons, where the requirement of a large vertex separation must be imposed to reduce the non-charm background. Figure 76a) shows the combined invariant mass histograms for several D meson decay modes with no Čerenkov requirements. Figure 76b) has the additional requirement that the single kaon in these decays be identified in the K or K/P categories by the Čerenkov system. The ratio of the areas of the peaks in the two histograms demonstrates an average kaon identification efficiency of 0.60 ± 0.04.

The second method involves binning the events in the signal region according to the Čerenkov identification category of one of the decay particles. Events in the background region away from the signal are also binned but are subtracted from the the signal. An example of the signal region and the sideband background regions is shown in Fig. 76c) for the case of ϕ decay. Table 13 gives the fraction of topologically identified kaons falling into each Čerenkov category for both D and ϕ meson decays. The identification of the proton in topologically identified Λ^0's and the pions in the topologically identified K_s^0 is also tabulated. The bottom portion of the table gives the fraction of the particles which are 'well-identified'. In the case of kaons, this corresponds to the

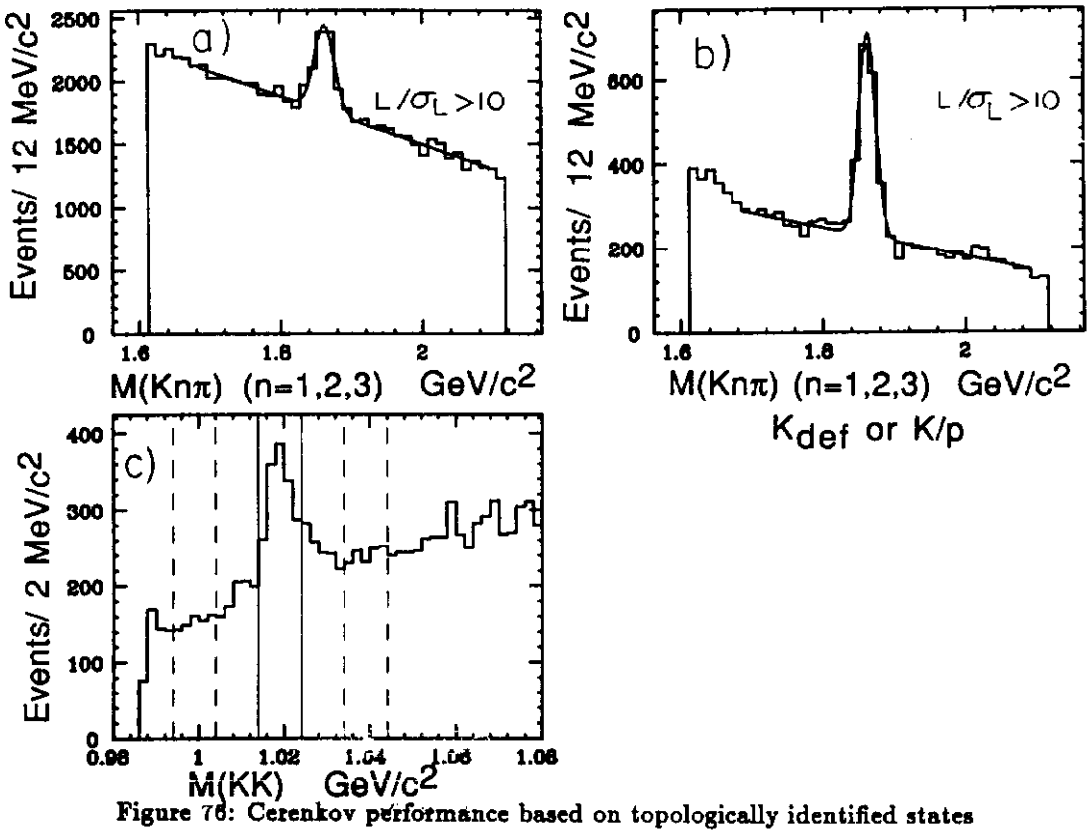

Figure 76: Cerenkov performance based on topologically identified states

K or K/p categories. Due to the restricted momentum range of the Čerenkov identification, there is no reason to expect kaons from D decay and ϕ decay to have the same efficiency. More of the kaons from D decay than from ϕ decay are under-specified in the Čerenkov system, which is consistent with their momentum spectra. Finally, the fraction of the particles in the signal region which fall into inconsistent categories (e.g. kaons identified in a category which is clearly other than a kaon) is listed at the bottom of the table.

A second study of Čerenkov efficiency has been carried out using only the $D^{\pm}$ decay to $K^{\pm}\pi^{\mp}\pi^{\mp}$. Figure 77a) shows the $K\pi\pi$ effective mass distribution for combinations in which three charged particles, reconstructed utilizing microstrip information only, formed a secondary vertex downstream of a production vertex. The production vertex was required to lie within the target. The particles were each required to be linked with a track reconstructed in the spectrometer and the combination of three tracks had to have a net charge of ± 1. The kaon mass was assigned to the particle with the unlike charge. The momentum vector of the three track combination was required to have an impact parameter relative to the primary vertex of less than $60\mu m$. A fit to the $D^{\pm}$ signal in this figure yields 1080 ± 49 events.

Figure 77b) shows the same distribution but with Čerenkov identification cuts. In order for a track to be called a pion, its Čerenkov identification was "not heavy" – that is, it was not identified as an unambiguous kaon, an unambiguous proton, or as K/proton ambiguous. In order for a track to be called a kaon,

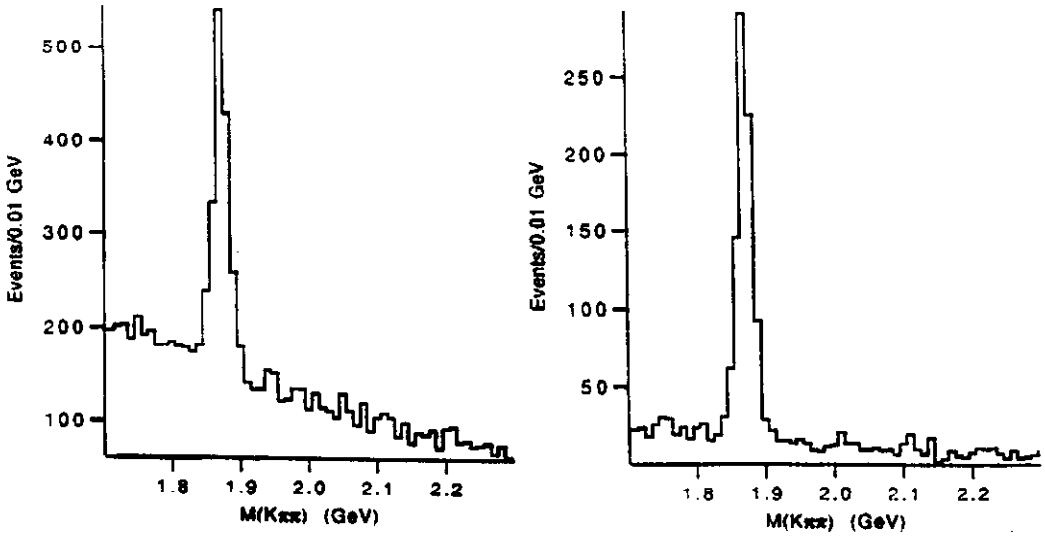

Figure 77: $K^{\pm}\pi^{\mp}\pi^{\mp}$ effective mass distribution for events selected as described in the text (a.) without Čerenkov cuts and (b.) with Čerenkov cuts.

its identification was either as a unique kaon, as ambiguous between kaon and proton, or, if its momentum was greater than 60 GeV/c, as pion/kaon/proton ambiguous. A fit to the signal in this plot yields 801 ± 41 events. From these fits,the Čerenkov efficiency for the $K\pi\pi$ system, averaged over the full momentum range present in this decay, is 74%.

In a final attempt to understand the performance of the Čerenkov system and the associated particle identification algorithms, a very detailed simulation of the Čerenkov counters was developed. The Monte Carlo simulation for each Čerenkov counter explicitly takes into account the threshold, the detailed geometry of the mirrors and light collection cone arrays, and the photon detection efficiency for each cell. The "photon detection efficiency",i. e. , the efficiency, averaged over wavelength, for detecting radiated photons as collected photoelectrons, depends on radiator transparency, mirror reflectivity, and photocathode quantum efficiency. The simulation of electronics noise, a significant source of misidentification below threshold, is currently being implemented. Simulation is carried out not only for tracks which pass all the way through the counter but also for tracks which decay or are produced inside the counter volume.

An indication of how well the Čerenkov simulation works is obtained by comparing the pion identification efficiencies measured using minimum bias hadronic data with the corresponding efficiencies determined from a charm Monte Carlo data sample. In each case, K^0_S decays have been used to tag the pions. Table 14 shows efficiencies for assigning the pions various ID's. A "perfect" ID is defined as the ID which would be assigned to the pion using perfect (high photostatistics and fine segmentation) Čerenkov counters. In this table, p_{Cn} is the pion threshold momentum for counter Cn. Tracks with a 2-counter topology are tracks which pass through C1 and C2 only while 3-counter tracks pass through C1, C2, and C3. "Heavy" means the ID is consistent only with a kaon and/or

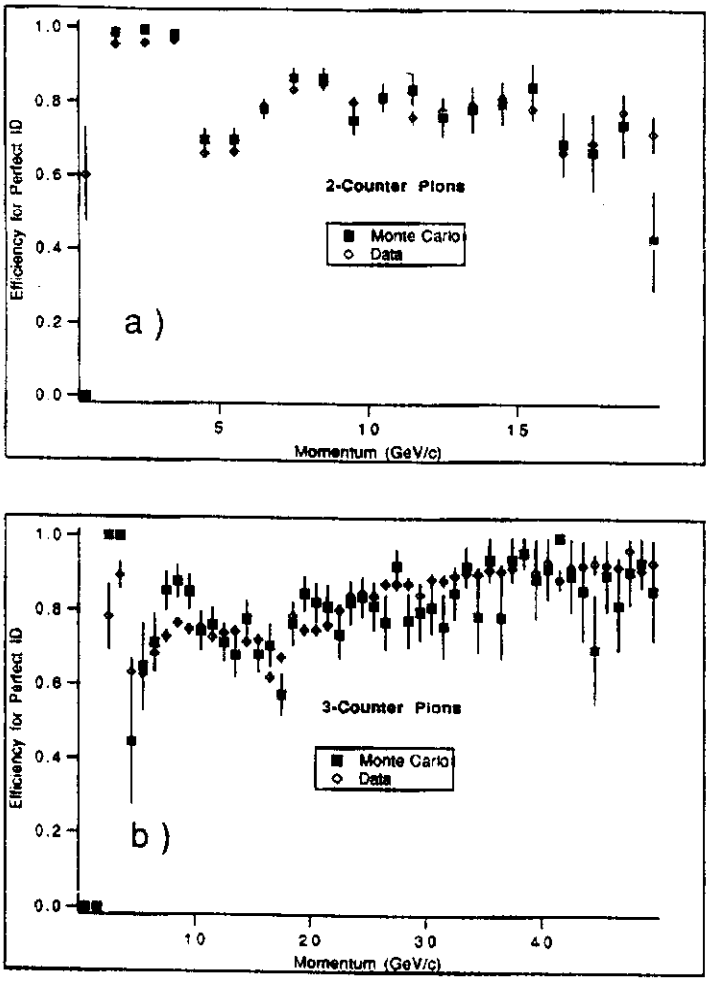

Figure 78: Plot of the efficiency for assigning pions the "perfect" ID as a function of momentum for the data and for the Monte Carlo events.

a proton.

Overall, the agreement between Monte Carlo simulation and data is satisfactory. The discrepancy in the efficiency for misidentifying 2-counter (3-counter) pions with momenta below the C1 (C3) pion threshold as electrons should be largely removed with the addition of electronics noise simulation.

The efficiency for assigning pions the "perfect" ID is plotted as a function of momentum is shown in Fig. 78 for both data and Monte Carlo events. The agreement between data and the simulation is very good when one considers that noise simulation is not yet included and that real differences between Monte Carlo event topologies and data event topologies do exist.

6.5 Measurement of Proper Time Distributions of Short Lived Particles

The ability of the tracking system to resolve a heavy quark decay vertex from the primary interaction vertex (and the accompanying heavy quark state) has been identified as a major tool for bringing out signals for short-lived particles and suppressing backgrounds. This capability, of course, implies the ability to

Table 13: Čerenkov Identification by Categories

ID category	Kaons (D)	Kaons (ϕ)	protons (Λ)	Pions (K_s
none	.009±.015	.040±.010	.068±.013	.026±.002
electron	-.009±.020	.003±.007	.003±.008	.030±.002
π	.035±.038	.014±.014	.037±.015	.306±.006
e/π	-.008±.055	.106±.030	.037±.028	.347±.006
K	.265±.019	.402±.020	.069±.013	.014±.001
K/π	.010±.004	.005±.003	.002±.001	.004±.001
K/πe	.140±.023	-.011±.009	.011±.010	.016±.001
p	.040±.012	.050±.009	.378±.026	.005±.001
K/p	.400±.030	.380±.020	.426±.028	.012±.001
π/K/p	.060±.050	.010±.007	.029±.010	.210±.005
e/π/K/p	.060±.020	.001±.013	.018±.009	.030±.002
K or K/p	.670±.036	.780±.028	–	–
p or K/p	–	–	.804±.038	–
π or e/π	–	–	–	.653±.008
inconsist	.071±.070	.210±.030	.153±.039	.087±.003

Table 14: Comparison of efficiencies for Čerenkov identification of pions from K^0_s decay in data and in Monte Carlo event samples.

Topology	ID	Data	Monte Carlo
3-counter	Pion consistent	0.90	0.90
	Perfect	0.78	0.79
	Electron ($p < p_{C3}$)	0.06	0.01
	Heavy ($p > p_{C2}$)	0.03	0.04
2-counter	Pion consistent	0.94	0.95
	Perfect	0.80	0.82
	Electron ($p < p_{C1}$)	0.03	0.002
	Heavy ($p > p_{C2}$)	0.04	0.04

measure the time evolution of weak decays. In this section, the measurement of the proper time distribution for weak decays is discussed briefly. The time evolution of $D^{\pm}$ decays, where the $D^{\pm}$ is detected through the $K\pi\pi$ final state, is presented as an example. The detailed methods used to extract lifetimes, to account for backgrounds, and to correct the observed time evolution are discussed elsewhere [51].

The measured proper time t_{meas} and its estimated uncertainty σ_t for the decay of a particle of mass M_X with momentum P_X are:

$$t_{meas} = \frac{L}{c}\frac{M_X}{P_X} \tag{27}$$

and

$$\sigma_t = \frac{\sigma_L}{c}\frac{M_X}{P_X}. \tag{28}$$

The uncertainty in the proper time has been discussed above and has the value 0.048 picoseconds; it depends only weakly on the event topology and momentum.

The raw time distribution will not look exactly like a pure exponential with the mean lifetime of a $D^{\pm}$ for several reasons:

1. Background events enter the time distribution along with signal events and are likely to distort it.

2. The signals are extracted by applying a significance of detachment cut, which means that the 'proper time' cut varies on an event-by-event basis.

3. There is a loss of signal at small values of the proper time. This comes from the fact that resolution effects may push 'signal' events to negative lifetimes but there is no compensation from the other direction since there are no true 'negative' lifetime events.

4. The spectrometer does not have a uniform geometric efficiency as a function of proper time. At large proper times, $D^{\pm}$'s may live long enough to decay in the microstrip detector itself which makes them more difficult to reconstruct. Particles which are produced and decay far from the microstrip detector have a lower acceptance than those that are produced and decay nearer to it.

5. The proper time distribution must be corrected for such effects as the absorption of the parent particle and the decay products in the target.

Corrections are applied to the raw distributions to remove each of these effects. The second effect can be handled by using the so-called 'reduced proper time' [52]:

$$t_r = t_{meas} - N\sigma_t. \tag{29}$$

The number N is chosen arbitrarily but must be greater than or equal to the cut used to select the signal. The t_r parent distribution for the signal is also

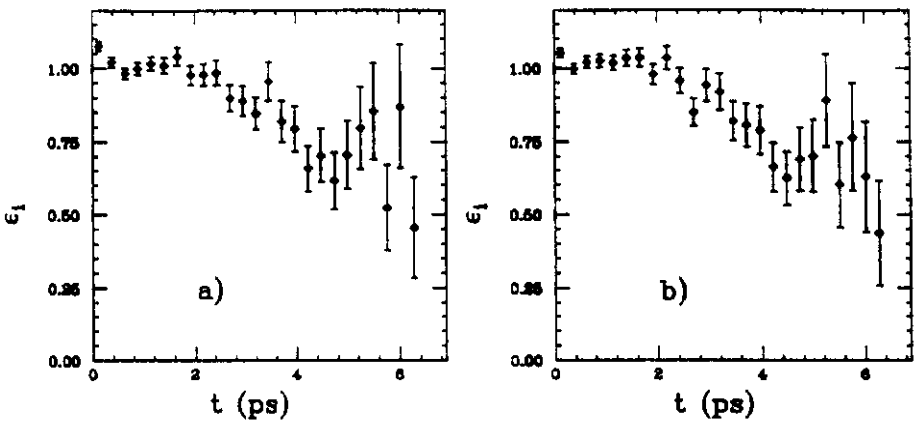

Figure 79: The modulator functions $\epsilon(t_\tau)$ for (a) $N = 3$ and (b) $N = 5$

an exponential with the same lifetime. This means that the clock is started for each event based on the topology (resolution) for that event. The lifetime should, in principle, be independent of the value chosen for N. Effects 3,4, and 5 are handled by means of a 'modulator' function $\epsilon(t_\tau)$ which is determined from Monte Carlo studies.

The correction for the background can be handled by applying sideband subtractions, by parameterising it, or by trying to understand in detail the sources of background and modelling them. All these approaches have been pursued and are discussed elsewhere[51].

Figures 79a) and b) show the 'modulator' functions determined from the Monte Carlo for $N = 3$ and $N = 5$, respectively. The distributions in the quantity t_τ are shown in Fig. 80a) and b) for a choice of $N = 3$ and $N = 5$, respectively. These particular distributions have been corrected by the appropriate function $\epsilon(t_\tau)$ and have had the background subtracted. The background has been determined using sidebands in the mass distribution above and below the signal and then employing a maximum likelihood fit to obtain the 'signal' in each bin of t_τ. The curves superimposed on the figures are exponentials with lifetimes between 1.05 and 1.10 picoseconds, in good agreement with the world average[50]. The final value and the associated statistical and systematic uncertainties are still being evaluated, but the ability of the detector to produce high quality time evolution distributions is clearly demonstrated.

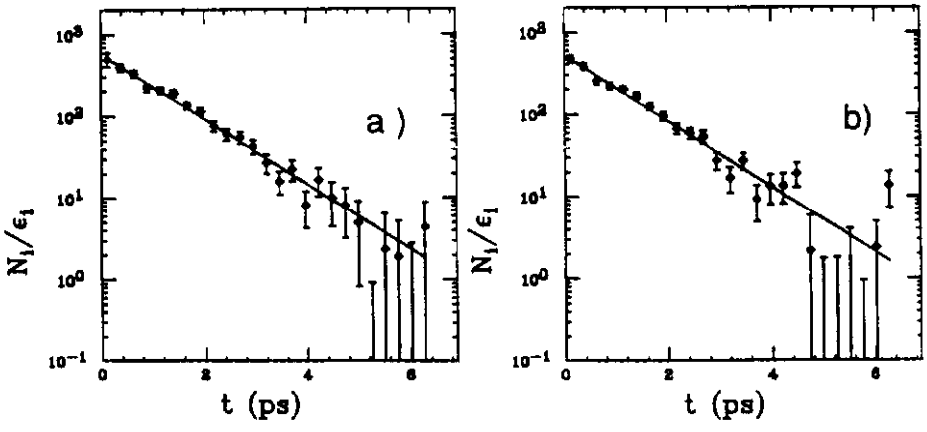

Figure 80: The corrected reduced time distribution for the $D^{\pm}$ for (a) $N = 3$ and (b) $N = 5$

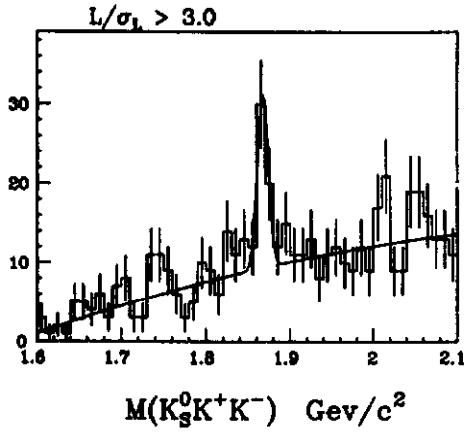

Figure 81: Mass plot of the final state $K^0_s K^+ K^-$

7 Conclusion

The E687 detector described above has been shown to have excellent tracking and particle identification capabilities. The detectors themselves are capable of sustaining high particle fluxes and they are backed up by a fast and reasonably sophisticated trigger and a data acquisition system capable of logging about 3000 events per Fermilab beam spill. These characteristics are required to do high precision studies of the complex final states into which particles containing heavy quarks decay. So far, the main successes of the spectrometer have been in studying states decaying to charged particles. Analysis of states containing photons is now underway and improvements to the detector promise to add this to the catalog of its strengths. Figure 81 shows a plot of the final state $K^0_s K^+ K^-$ whose analysis employs all the power of the vertexing, neutral vee reconstruction, and particle identification and is a final demonstration of the ability of the spectrometer to reconstruct complex decay modes. This spectrometer should provide spectacular samples of fully reconstructed charmed particles that will provide new insights into the weak decays of these fascinating and unusual objects.

Acknowledgements

It takes many people to construct a facility such as the Fermilab Wideband Beam/E687 spectrometer. We wish to acknowledge the assistance of the staffs of Fermilab, Laboratori Nazionali di Frascati, the physics departments of the University of Colorado, University of Illinois, Northwestern University, University of Notre Dame, and the I.N.F.N. Sections and the Physics departments of the Bologna University, Milano University, and Pavia University.

We would like to thank Ken Stanfield and John Peoples of Fermilab for encouraging and supporting the effort from its very beginning. We want to thank the Fermilab Research Division, Technical Support Section, and Physics Section, especially the design and installation team lead by Ron Currier, the electronics team lead by Sten Hansen, Angelo Cotta-Ramusino, and Tom Regan, the wire chamber team lead by Karen Kephart, the experiment operations team of Garvey Hale and Roy Justice, the data acquisition support team lead by Victoria White and Ruth Pordes, the ACP group lead by Tom Nash, the magnet design and construction teamlead by Ed Black, Al Ito, Jack Jagger and Jim Humbert. We would also like to thank the Accelerator Division for the excellent performance of the machine during the run and the Computer Operations staff for handling the thousands of tapes and many jobs associated with the data analysis.

We acknowledge the technical help of: G. Bacchiocchi, A. Igiuni, S. Grabar (Milano); L. Daniello, B. Dulach, G. Sensolini(Frascati); E. Imbres and P. Trespi(Pavia) and R. Schluter(Northwestern University).

In the case of E687, a disaster befell the experiment just as it began to collect data and many of these same people, and many additional people, were called upon to put things back in order. All the data shown in this paper were collected after these people performed their miracle. We would like to thank Leon Lederman for providing the resources and encouragement to accomplish the recovery. We want to thank the Fire Recovery Team, appointed by Ken Stanfield, consisting of Ron Currier, R. Scherr, N. Bosek, Peter Kapser, Age Visser, and Tom Prosapio. We want to praise the efforts of John Elias and Dan Green who lead the Fermilab group that investigated the fire. And we especially want to thank the DOE investigation team, led by Justin Zamiroski, who combined professionalism and compassion to, in a short period of time, determine the cause of the fire and help us get back on the road to recovery. We would like to thank Stephen Pordes, Don Carpenter's group at Lab 7, and Bill Burley and Gene Beck of the Physics Department Plastics Shop for their help. We would like to thank our many friends throughout the high energy community for their offers of assistance.

This research was supported in part by the Istituto Nazionale di Fisica Nucleare (I.N.F.N.) of Italy, Ministero della Universita' e della Ricerca Scientifica, the National Science Foundation, and the U.S.Department of Energy.

References

[1] The Montecarlo program and the pattern recognition for the microvertex detector of E687 experiment at FNAL; M.Giammarchi et al. NIM A251,40 (1986).

[2] P.L. Frabetti et al., Measurement of the Λ_c^+ and D_s^+ Lifetimes, submitted to Physics Letters.

[3] L.M. Jones and H.W. Wyld, Phys.Rev. D17:759 (1978)

[4] Tagged Photon Beam design report, C. Halliwell et al., Nucl. Instr. and Methods,102,51 (1972)
D. Aston et al.,NIM 197(1982)278.
M. Winter,Universite Louis Pastuer de Strasbourg, thesis, 1981, CRN/HE 81-03,
H.W. Atherton, et al., CERN/SPS 85-43 (EBS)

[5] Wide Band Beam Design Report,Fermilab TM, No. 963,1980 (updated 1989).

[6] D. Kruse and G. Koizumi, Fermilab TM-607 (1975) unpublished, and S. Snowdon and H. Stredde, Data Sheet 2220.10, Fermilab, unpublished.

[7] E. Kneip, Fermilab Technical Specification 2221-ES-27487 (1974) and S. Snowdon, Data Sheet 10-28-74, Fermilab, unpublished.

[8] Accumulator Dipoles: "Design Report, Tevatron I Project, Fermilab, Batavia, IL, September 1984".

[9] C.R. Kerns, "A high-rate phototube base", IEEE Trans. Nucl. Sci., Vol. NS-24, No. 1, pp 353-355, Feb. 1977.

[10] J. Knauer, et al., Proceedings of the Calorimeter Workshop, Fermilab, 1975, page 215, unpublished.

[11] A. Ito, W. Bosworth, W. Yang, Experiment #E687 Magnet 50-30-66, Engineering Note 08-08-83, Fermilab, unpublished.

[12] A. Ito et al., Ziptrack Manual, Fermilab TM no. 1200 (1983)

[13] An improved Silicon target for the lifetime measurements of short living particles in the 10^{-13} region, G.Bellini et al., IEEE V.NS30, 1 (1983) p.415

[14] The microstrip vertex detector for E687 experiment at Tevatron; G.Bellini et al.,NIM A252,366(1986).

[15] A fast ADC system for silicon microstrip readout; P.Inzani et al., IEEE Transactions on Nuclear Science, Vol. NS-33, N.1, Feb '86, pag. 911.

[16] Sten Hansen, Fermilab Physics Department, drawing number 3687-ED-240542

[17] H. Mendez,Ph.D. thesis, Cinvestav-IPN,Mexico, 1990 (unpublished)

[18] R. Yoshida, Ph.D. thesis, Northwestern University, 1990, (unpublished)

[19] Polivar S.P.A., Rome, Italy

[20] Physics Department,Fermilab

[21] Hammamatsu, Bridgewater, New Jersey

[22] R. Yoshida et. al.,"Tetrode Photomultiplier Base for Magnetic Field Environments", IEEE Transactions on Nuclear Science, Vol. 33,No. 1,February,(1986)

[23] We would like to express thanks to Professor Michael Marx of SUNY, Stonybrook, for the loan of R2107 photomultipliers.

[24] Plessey Semiconductors,Irvine, California.

[25] We would like to thank Professor Robert Ely of Lawrence Berkeley Laboratory for the loan of the amplifier cards and most of the readout cables for the muon proportional tubes.

[26] S. Bianco et al., INFN-Frascati note LNF-85/49(R)

[27] G. Bologna et al., Nucl. INstr. and Meth. 192(1982)315.

[28] S. Park, D. Buchholz, C. Castoldi, D. Claes, B. Gobbi, R. Schluter, and R. Yoshida, IEEE Trans. Nucl. Sci. NS-34 (1987) 516.

[29] S. Park, D. Buchholz, C. Castoldi, D. Claes, B. Gobbi, R. Yoshida, A. Sala, V. Arena, G. Boca, A. Cotta-Ramuniso, R. Diaferia, S. Ratti,and P. Vitulo, Nucl. Instr. and Meth. A289 (1990) 496.

[30] Trademark for a G10 type of plastic.

[31] E. Iarocci, Nucl. Instr. and Meth. 217 (1983) 30; G. Battistoni, et al., Nucl. Instr. and Meth. 202 (1982) 459.

[32] We wish to thank T. Lyons of Fermilab for loaning us the tooling die for the aluminum extrusions.

[33] G. Bertrand-Coremens, et al., "The Streamer Tube of the Charm II Neutrino Detector," Proceedings of the Gas Sampling Calorimetry Workshop II, Fermilab (1985) p. 313.

[34] We wish to thank E706 at Fermilab for the use of the press table.

[35] R.J. Yarema, et al., IEEE Trans. Nucl. Sci. NS-33 (1986) 933.

[36] This chip was designed in collaboration between Tsukuba University and Fujitsu Corp. of Japan. It is a common base amplifier.

[37] Sten Hansen, Fermilab Physics Department, drawing numbers 3687-EB-240546, 3687-EB-240549, 3687-EC-240547, and 3687-EC-240548

[38] analog summation circuitry

[39] Sten Hansen, Fermilab Physics Department, drawing numbers 3687-EC-240543,3687-EC-240544

[40] J.F. Bartlett et all "RT/RSX MULTI: Packages for data acquisition and analysis in high energy physics" IEEE transactions on Nuclear Science Vol NS 26 No 4 Aug 1979

[41] UPI: FASTBUS Demonstration Systems, E. Barsotti et all IEEE transactions on Nuclear Science Vol NS 29-No 1 Feb 1982

[42] Bison Box: Internal Fermilab note HN 3.2. Ron Martin et al

[43] V. White, et al "The VAXONLINE Software System at Fermilab" IEEE Transactions on Nuclear Science, Vol.NS-34, No.4, August 1987.
R. Pordes et al, "List Processing Software for the LeCroy 1821 Segment Manager Interface", IEEE Transactions on Nuclear Science, Vol.NS-34, No.4, August 1987.
T. Dorries et al, "VMS Software for the Jorway-411 Interface", IEEE Transactions on Nuclear Science, Vol.NS-34, No.4, August 1987.

[44] T. Sjostrand, M. Bengtsson, Computer Phys. Comm. 43 (1987) 367

[45] Statistical Package for the Social Scieinces (SPSS), McGraw Hill, New York (1975)

[46] R. Brun *et al., GEANT3 User GUIDE, CERN program library DD/EE/84/-1*

[47] Karen Lynette Lingel, Photoproduction of $D^{\pm}$ Mesons, University of Illinois Ph. D. thesis

[48] G. Ingelman, A. Weigend, Computer Phys. Comm. (1987) 241

[49] J.C. Anjos et al., Phys.Rev. Lett. 62,513(1989)

[50] B. P. Yost *et al.*, Phys.Lett. B204,1(1988)

[51] Glen Richard Jaross, Photoproduction of $D^{*\pm}$ and D^0 Mesons, University of Illinois Ph.D. thesis and
Karen Lynette Lingel, Photoproduction of $D^{\pm}$ Mesons, University of Illinois Ph. D. thesis

[52] J. R. Raab, UCSB-HEP-87-8, Lifetime Measurements of the Three Charmed Pseudoscalar D-Mesons,Ph.D. Thesis, University of California, Santa Barbara, 1987

A Derivation of Fast Trace

The starting point is the expression

$$\vec{r'} = \frac{\vec{g}}{\sqrt{1 - g_y^2 - g_z^2}}, \qquad (A-1)$$

with the identities:

$$\vec{g} \equiv (\vec{I} + \vec{\alpha}), \qquad (A-2)$$

and,

$$\vec{I} \equiv \frac{\vec{r_0'}}{\sqrt{1 + y_0'^2}}, \qquad (A-3)$$

$$\vec{\alpha} \equiv \frac{.29997}{p} \int_{z_0}^{z} \vec{r'}(z_1) \times \vec{B}(z_1) dz_1 \qquad (A-4)$$

Notice that $\vec{I}$ contains the initial conditions only and $\vec{\alpha}$ contains all the field information.

As an example, the case of the y view only is treated here. Equation A-1 is expanded in a Taylor series to give the result:

$$y' = \sum_{j=0}^{\infty} \frac{1}{j!} \left[\left(g_z \frac{\partial}{\partial u} + g_y \frac{\partial}{\partial v} \right)^j \frac{v}{\sqrt{1 - v^2 - u^2}} \right]_{u=v=0} \qquad (A-5)$$

Next, the binomial expansion is used to deal with the polynomial:

$$y' = \sum_{j=0}^{\infty} \sum_{m=0}^{j} \frac{\binom{j}{m}}{j!} g_z^{j-m} g_y^m \left[\frac{\partial^{j-m}}{\partial u^{j-m}} \frac{\partial^m}{\partial v^m} \frac{v}{\sqrt{1 - v^2 - u^2}} \right]_{u=v=0} \qquad (A-6)$$

The expressions A-2-A-4 are inserted into the equation (A-6) the binomial expansion is applied again, an identity from the calculus dealing with series forms of derivatives is employed and the final result emerges:

$$y' = \sum_{i=0}^{\infty} \sum_{k=0}^{\infty} \frac{\alpha_z^i \alpha_y^k}{i!k!} F_y^{(i,k)}, \qquad (A-7)$$

with this definition

$$F_y^{(i,k)} \equiv \frac{\partial^i}{\partial I_z^i} \frac{\partial^k}{\partial I_y^k} \frac{I_y}{\sqrt{1 - I_z^2 - I_y^2}} \qquad (A-8)$$

A similar expression can be found for x' by exchanging the x-y subscripts in equations (A-7) and (A-8).

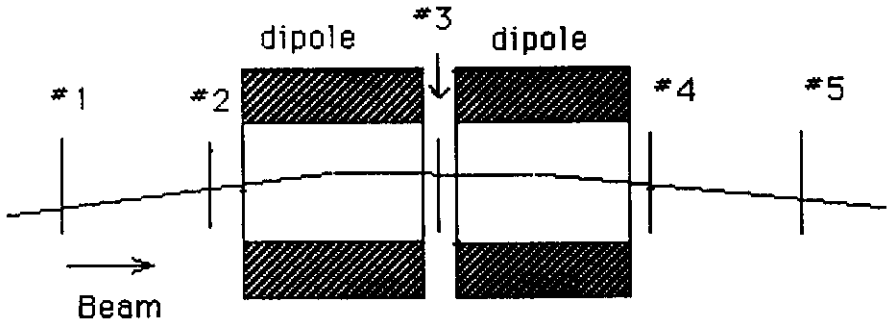

Figure B-1: Layout of the beam tagging spectrometer

B Beam Electron Momentum Tagging System

In the first run of E687, the incident photon energy was poorly measured because of the momentum spread of the beam electrons. In order to improve this measurement, it is necessary to measure the momentum of each electron before it reaches the radiator.

B.1 The Beam Tagging Spectrometer

Beam tagging for the second run of E687 has been accomplished by using the pair of dipoles which form the final piece of the double dogleg as a magnetic spectrometer. The deflection due to these magnets is measured by 5 large-area microstrip detectors. These detectors have a total active area of 7.7 cm × 5.7 cm. Each detector has 256 strips of 300 μ pitch. Two detectors upstream of the dipoles measure the incoming angle and two downstream measure the outgoing angle. A detector located in the small gap between the two dipoles improves the pattern recognition capability of this spectrometer when two tracks are found in the same radiofrequency(rf) bucket and helps avoid confusion due to spurious hits. Planes #4 and #5 (the most downstream ones) are set as far apart as as possible. The separation is limited by a beamline quadrupole. Monte Carlo simulation shows that the best performance, taking into account both resolution and acceptance, is obtained when the upstream microstrips are placed in a symmetric configuration. The distance between plane #1 and plane #5 is 13.7 meters. The location of the microstrip planes is shown in Fig. B-1. The predicted resolution is about 1.6% and the acceptance is about 81% of the electron beam whose bremsstrahlung photons reach the experimental target. This resolution is well matched to the resolution of the RESH, when it is used to provide an energy measurement of the electron after it radiates.

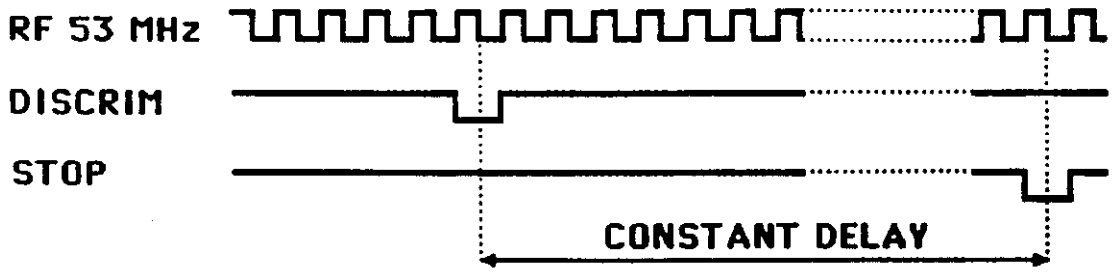

Figure B-2: Timing relationships in the beam tagging system.

B.2 Beam Tagging Electronics and Setup

The system has been operated with beam intensity in excess of 10^7 particles/sec. As a result, the jitter of the detector pulses with respect to any latching strobe must be kept as small as possible. For this reason it was decided to put the read out electronics close to the detector to avoid long trasmission lines for the 1280 channels.

The 2nd level trigger from the E687 spectrometer is available at the detector site about 2.5 μs after the beam particle crosses the detector. This means that the readout system must have enough memory to hold the addresses of hit strips until the arrival of the trigger.

The working principle of the detector is illustrated in Fig. B-2. The beam particles have a constant phase with respect to the accelerator rf signal. This phase relationship is degraded by a few ns by the jitter introduced by the detector,the preamplifier, and the discriminator. The signals from the discriminator are sent to a "shift register" continuously clocked by the accelerator rf signal. When an event trigger occurs, a signal is sent from the counting room to the system in the beam line to stop the shift register. Since the decision time is constant, the time interval between the pulse at the input of the shift register and the stop signal is also constant. One can then read the proper cell in the shift register at a fixed offset (in rf units) from the stop.

The accelerator rf is 53 Mhz and the localization of a particle inside a single rf bucket is about 1 ns. As stated in the previous paragraph, the rf/data timing is very important. To minimize the jitter of the data being written into the memories with respect to the rf, a fast current preamplifier with a rise time of about 10 ns is used. These have been realized on thick film circuits and have a bipolar input transistor. The noise FWHM is equivalent to 18 KeV in silicon with the detector connected, for a signal to noise ratio of 11.

Each strip has a discriminator with an independent CAMAC programmable

threshold. The output signal from these discriminators is as wide as the rf period. This is done to avoid latching the same signal in more than one memory location once the rf/data timing has been properly set.

Hit data for each channel is stored in fast ECL circular memories clocked by the 53 MHs accelerator rf, which synchronizes them with the beam structure. Since the objective is to extract the data for the triggered particle by subtracting a constant delay from the memories upon stop signal arrival, both the rf/data timing, and also the rf/stop timing are very important. These are set in the following way: the first level trigger, whose maximum jitter with respect to the rf is ± 1 ns, enables a counter clocked by the rf. This counter is set in such a way that the end-counting signal, whose timing is set by the rf, comes a few ns after the eventual second level trigger. The stop signal to the memories is the coincidence between these two signals. In this way the stop signal has no jitter with respect to the rf and the memories are stopped only when the second level trigger is present.

The readout is started approximately 50 ns after the stop arrival. It is done through a daisy chain with a 32 bit data bus, connecting the 8 memories in the same plane to the local (plane) termination unit and the 5 termination units in the system among them. The first termination unit is the master and it is connected to the E687 FASTBUS DAQ. While data are being read out, they are also stored inside the local termination and can be accessed via CAMAC for independent monitoring. The readout is 5×10^6 32 bit words/s for a total readout time of 8 μs. After the last memory has been read out the system is immediately restarted to take new data.

A test with a Sr^{90} source,fully confirmed with the beam, showed that it is possible to set the thresholds in such a way as to have an acceptably low number of spurious hits due to electronic noise and still have 100% efficiency on the signal. High statistics threshold curves of the noise spectra normalised to the number of samplings were made for each channel and then a program set the thresholds at a level of less then 1 spurious hit per strip over 1000 samplings. For 1280 channels, this gives 1.2 spurious hits per event; this does not present a problem to the pattern recognition program.

Each of the 40 memories used in the system has an independent constant delay (measured in terms of rf buckets) between the ionisation collection and the arrival of the stop signal. The expected offset is calculated and then the timing is "scanned" around that value in one rf bucket steps. There is a uniform background of counts for the wrong offsets and a sharp growth when the offset is correctly set to the rf bucket of the triggered particle.

Each of the 40 memories requires two separate delays to set the correct timing between the rf signal and the data and between the rf signal and the stop. The rf/stop timing was first set using the electronic calibration data. Then the rf/data timing was set in such a way to always latch the data in only one memory location.

B.3 Pion Calibration and Electron Data.

The system has been aligned by turning off the bending magnets and taking straight-through electrons.

The measurement of the resolution and the absolute momentum calibration is accomplished by passing a low intensity pion beam into the E687 spectrometer. The momentum measurement of the beam tagging system, p_{tag}, is then adjusted so that it agrees with the momentum measurement of the spectrometer,p_{spec}. The accuracy of the spectrometer momentum measurement was discussed previously. The studies required to achieve full resolution and absolute calibration of the spectrometer for the second running period are still in progress, so the results of this study must be viewed as preliminary.

Low intensity pion runs at 30, 60 and 350 Gev have been taken with the radiator and the target removed. Only events with one track in both the beam tagging system and the E687 spectrometer are used. The field in the "beam tagging magnets" has been scaled with the pion beam energy, so that the beam tagging resolution (apart from MCS effects that have been taken into account) is constant and predicted to be about 1.6%, while the expected resolution for the spectrometer is about 5% at 350 GeV. The overall resolution at 350 GeV was about 7% and was mainly due to the spectrometer because the final magnetic alignment had not been performed for the second run. At 30 and 60 GeV, where the spectrometer resolution is much better than the beam tagging resolution, the observed beam tagging resolution in both cases is about 2%, very close to the predicted value. The results are shown in Fig. B-3. Analysis of these data will be repeated when the final magnetic alignment of the spectrometer for the second running period is completed.

Efficiency studies have been performed for each strip using tracks within the acceptance and the average efficiency per plane is about 98%. This includes the effect of dead electronics channels and disconnected strips.

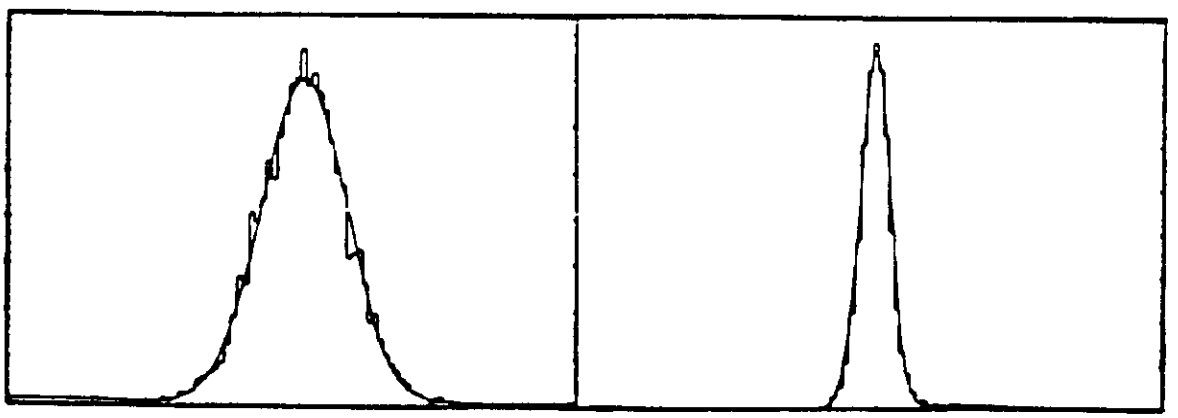

Figure B-3: The quantity $(p_{tag} - p_{spec})/p_{spec}$ for a) 350 GeV/c pions and b) 60 GeV/c pions. The resolution in the first plot, $\sigma = 7.4\%$ is dominated by the spectrometer resolution. The resolution in b), $\sigma = 2.6\%$ is dominated by the beam tagging resolution.